ETH
Eidgenössische Technische Hochschule Zürich
Swiss Federal Institute of Technology Zurich

Diplomarbeit

State Tomography of Multiple Qubits in Circuit QED

Presented by: Peter Maurer
Supervisor: Prof. Dr. Andreas Wallraff,
Laboratorium für Festkörperphysik, ETH Zürich
Duration of work March to July

Zürich, July 25, 2008

Abstract

In this thesis we realize a state tomography method to fully characterize the quantum state of one and two superconducting quantum bits (qubits) in the circuit QED architecture.

Superconducting qubits [1] coupled to a microwave resonator with high quality factor [2] are a promising system for quantum information technology and have an interesting analogy to cavity quantum electrodynamics (QED) known from atoms. Coherent control of these systems is theoretically well described for single qubit operations and two qubit operations [1]. Most resent it became possible to create entangled states [3] and Controled NOT (CNOT) gates [4] using superconducting qubits. The ability of control over the system enables us to perform quantum state tomography [5] as well as process tomography [6].

Tomography is a useful experimental tool to measure any quantum state and hence analyze the performance of creating a desired state. Tomography is a standard procedure in NMR quantum computing [7] and widely used in ion traps [8]. This makes it favorable to apply tomography on superconducting qubits to analyze the quantum state.

This thesis deals deals with two transmission line shunted plasma oscillation qubits (transmon) [9] placed in a coplanar microwave resonator.

On this system tomography on one and two qubits has implemented. To proof the possibility of the tomography we have applied state tomography on different superposition states for one qubit. Furthermore, demonstration experiments were performed by applying tomography on Rabi and Ramsey pulse sequences. For all this processes the deviation to the expected theoretical value can be determine by using the L_1 norm. Moreover a Hadamard gate was implemented and process tomography was performed.

In the second part we investigate the tomography for two qubits by creating several product states and performing tomography on them. Since noise in the measurement causes the tomography to yield results, which do not fulfill the physical requirements (positive definite) for being a density matrix, we have implemented a "most likelihood" process [5] which always gives physical solutions.

The techniques developed in this thesis should form the basis for future experiments on more complicated processes.

Contents

Acknowledgments

During my four month research project in the Quantum Device Lab at the ETH Zurich I have enjoyed help from different peoples.

First of all I would like to thank to the principle investigator Prof. Andreas Wallraff. I have become motivated for the field of quantum computing during his courses on "Quantum System for Information Technology". After that I conducted a semester research project in his group, where I got familiar with the experimental setup. In that time I became fascinated by the topic and I decided to take my Diplomarbeit in this field. I had many inspiring discussions with him especially about experimental approach and about analysis of the results. Moreover he has supported me in other matters regarding my scientific career, for which I will always be thankful.

Furthermore I am thankful to Dr. Stefan Filipp, with whom I had several discussion on tomography and on measurement processes. It was very helpful to discuss with somebody who has work experience on tomography. Moreover he is also the person who proofread this thesis.

Also I am grateful to Dr. Peter Leek. He was working on a different project, which was using the tomography process developed in this thesis. It was good to work with him to implement the tomography in another project. In addition he also supported me with the mixer calibration which turned out to be harder then expected. Regarding the mixer calibration I would also like to mention Johannes Fink who was also working on the mixer calibration.

On an experimental point of view I also appreciate the support from Matthias Baur. He has been working for quite some time on the setup and could always give helpful hints when I was struggling with the settings.

As it can be seen in Section 4.3 I have used the experimental determined qubit qubit coupling constant, which was measured by Martin Goeppl. I am thankful to him for providing me with this data and for the Fig. 4.4.

Truly it was a very good time and I enjoyed to work with every member of the QDEV Lab.

Chapter 1

Introduction

Since Feynman introduced in 1982 the concept of a quantum computer [10] to simulate quantum mechanical phenomenas a lot of effort has been made to develop the field theoretically. Already in 1992 Deutsch and Jozsa proposed an algorithm [11], which determines whether a function is balanced or constant with a single evaluation of the function. Even though that this algorithm is of little practical use it shows how much more powerful a quantum algorithm can be compared to a classical one. In 1994 Shore developed an algorithm that brings an exponential speed up for integer factorization [12]. shortly thereafter Grover published in 1996 a search algorithm for unstructured data base [13], which speeds up computation time $O(\sqrt{N})$ where as a classical algorithm requires $O(N)$ steps.

On the experimental side effort has been made to create a system, which allows implementation of quantum algorithms. The criteria which have to be satisfied for a successful realization are given by the DiVincenzo criteria [14]. Several systems have the potential to satisfy these requirements most mentionable are quantum bits (qubits) based on ions [15], quantum dots [16] and superconducting circuits [17].

NMR qubits, which have been the only systems where Shor's algorithm has been successfully implementation so far [18], are not any longer considered to be a serious candidate for quantum computing, since upscaling is almost impossible. Qubits based on ion are the most advanced system among the remaining. Using ions Bell states, which is a quantum mechanical entangled state, has been created [8] and a Controlled-Not (CNOT) gate has been realized [19]. Most recent a low fidelity CNOT gate has been implemented in superconducting flux qubits [4].

Superconducting qubits can basically be divided into three types charge, flux and phase qubits [17]. Furthermore, superconducting qubits give the possibility to be coupled to a microwave resonator [1] [20]. This yield a system analogously to cavity quantum electrodynamics (QED) known from atomic physics, but with the opportunity to be able to engineer the coupling constant g and to change more easily the detuning between cavity and qubit transition.

The first coherent control of a charge qubit has been reported by Nakamura in 1999 [21]. Since then charge qubits have been improved i.e. to enlarge coherence time. Charge noise insensitivity has recently been realized in the transmission line shunted plasma oscillation qubit (transmon) [9], which is a modified charge qubit. For the presented Diplomarbeit a sample with two transmon qubits coupled to a coplanar high fidelity microwave resonator

similar to the device in [3] has been used.

To verify the creation of a desired state, for example the Bell state mentioned above, it is required to be able to determine both qubits quantum state. Since the measurement operators for the different components of the qubit's density matrix do not commute, as in the measurement of a single spin, tomography has to be performed. In this thesis we demonstrate the implementation of one and two qubit quantum state tomography by using a tomography procedure proposed in [5]. The system under consideration has regardless of the amount of qubits only one measurement operator. This requires to apply more tomography pulses than in other systems. Since the tomography procedure does not necessary yield a positive definite matrix we have furthermore implemented a most likelihood procedure, which determines the density matrix that is most likely to produce the recorded response [5]. This is important to find a physical solution. Moreover, we have implemented process tomography which determines the outcome of a process applied on an arbitrary state [6].

Tomography is required if we want to verify the creation of a desired state or if we want to determine the operation of a gate. However, in NMR tomography is a standard tool [7] and in ion traps tomography is already a well established procedure [8]. Since superconducting qubits are now on the edge to become used for creation of more advanced states and for the implementation of gates several groups are currently implementing tomography for their system.

Chapter 2

Basic Introduction to Circuit QED

Here I explain the basic theory about the two qubit system utilized. The chapter is outlined as following: the Cooper pair box is briefly introduce and how it is coupled to a cavity. Once we understand the physical background of the qubits we will explain how coherent operations are realized. Understanding this is important because the chapter on tomography will make use of the formalism defined here. In the following section qubit-qubit interactions will be discussed. This is of particular importance for two qubit tomography. Then we will explain the transmon qubit as particular realization of the Cooper pair box. In the end a short discussion of the measurement process for the transmon qubit will be given. After that I will present a short discussion on decoherence processes, which are important for to the transmon.

2.1 The Cooper pair box

We will first talk about the Cooper pair box, since this is a natural and the historical approach to the transmon qubit.

A Cooper pair box is a superconducting island, which is connected by a Josephson junction to a Cooper pair reservoir [22]. A Josephson junction [23] is a superconductor-insulator-superconductor sandwich structure, which allows Cooper pairs to tunnel coherently from one superconductor into the other one. This hopping of Cooper pairs through the junction is related to the Josephson energy E_J and can be described by a sum of raising and lowering operators

$$H_J = -\frac{E_J}{2} \sum_N \left(|N+1\rangle \langle N| + \text{H.c.} \right),$$

where we have introduced the charge basis $|N\rangle$, which characterize the number N of Cooper pairs on the island. It would be nice to be able to tune the Josephson energy E_J. This can be achieved by adding an additional Josephson junction to the system and in this way building a SQUID loop Fig. 2.1. The Josephson energy becomes then flux dependent and is given by

$$E_J(\Phi_{ext}) = \frac{E_J(0)}{2} \cos\left(\frac{\pi \Phi_{ext}}{\Phi_0}\right)$$

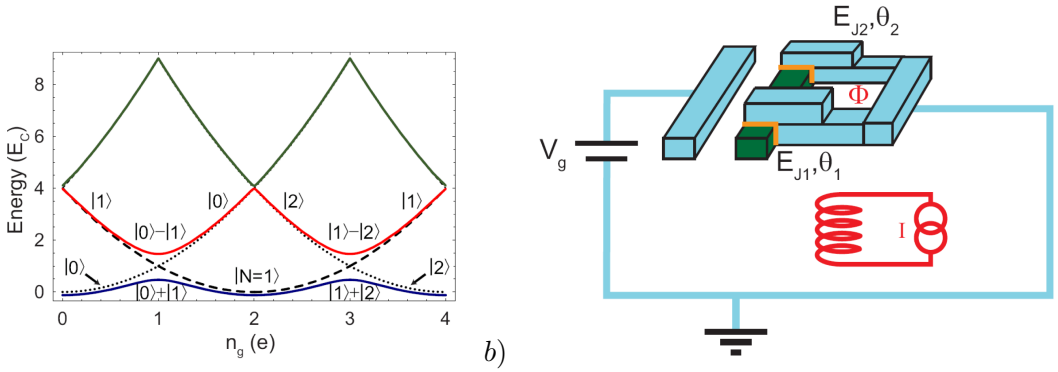

a) *b)*

Figure 2.1: The left graph shows systematically the energies for a Cooper pair box E_C as a function of the gate charge n_g. The Josephson energy of the SQUID can be controlled by the magnetic flux through the loop. On the left end of the picture the gate is shown. The pictures are taken from [24].

see [1]. On the other hand if we apply a gate voltage on the Cooper pair box, we will obtain the expression

$$H_C = 4E_c \sum_N (N - N_g)^2 \, |N\rangle \langle N| \,,$$

where the charging energy is given by $E_C = e^2/(2(C_\Sigma + C_g))\,(N - N_g)^2$ [1]. The total Hamiltonian for the Cooper pair box is given by

$$H = 4E_c \sum_N (N - N_g)^2 \, |N\rangle \langle N| - \frac{E_J}{2} \sum_N (|N+1\rangle \langle N| + \text{H.c.}) \,.$$

This Hamiltonian can be diagonalized numerically, if we use the charge basis $|N\rangle$ or analytically, if we use the flux basis $|\theta\rangle = \sum_N \exp(i\theta N) \, |N\rangle$, which results from a canonical conjugation of the charge operator $|N\rangle \langle N|$. A full diagonalization of the Hamiltonian can be found in [24].

Diagonalization of this Hamiltonian yield to Eigenenergies, which are periodic as a function of the gate charge n_g. Due to a finite Josephson energy E_J one can find that the degeneracies are avoided at points with n_g of integer. This is analogous to the tight binding model from solid state physics. The right graphic shows a Cooper pair box with a SQUID loop.

Since the eigenstates of the Hamiltonian are strongly anharmonic and the experiment is performed at sufficiently low temperature we can separate the Hilbert space for the Cooper pair box into a space for the first two levels H_{qubit} and for the remaining levels H_{rem}, $H_{\text{qubit}} \oplus H_{\text{rem}}$. The effective Hamiltonian becomes under this approximation [25]

$$H = -\frac{E_{el}}{2}\sigma_z' - \frac{E_J}{2}\sigma_x'. \tag{2.1}$$

Furthermore, we have restricted the charge to be in the interval $N_g \in [0, 1]$ and introduced the quantity $E_{el} = 4E_C\,(1 - 2N_g)$. This is the Hamiltonian for a spin $\frac{1}{2}$-particle in a magnetic field parallel to $(E_J, 0, E_{el})^T$ and we found the analogy to NMR qubits. We

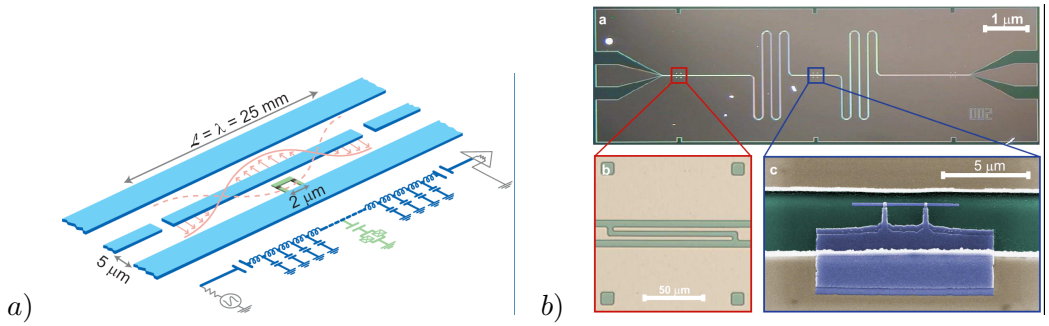

Figure 2.2: The left picture shows schematically a coplanar wave guide (blue), which is used as resonator. The equivalent network for the wave guide is also given [1]. The qubit Cooper pair box is show in the center of the resonator. The optical microscopy image to the right show the resonator (top), the finger capacitor (left bottom) and Cooper pair box (right bottom) [20].

can easily find a new basis $|0\rangle$, $|1\rangle$ in which the Hamiltonian is diagonal and the energy level splitting is given by $\hbar\omega_{01} = \sqrt{E_J^2 + (4E_C)^2(1-2N_g)^2}$. This already shows that the Cooper pair box is to first order charge noise δN_g insensitive at the sweet spot $N_g = \frac{1}{2}$ [26]. Therefore, it is favorable to run experiments at the sweet spot.

2.2 Cooper pair box coupled to a cavity

To protect the qubit from spontaneous emission, to realize readout and to implement coherent controll of the qubit the Cooper pair box is coupled to a resonator with high quality factor [1]. The resonator is a superconducting coplanar wave guide [2] with quality factor of several thousand. The Cooper pair box is placed in the resonators gap as shown in Fig. 2.2. The coplanar resonator-Cooper pair box system is analogous to a cavity atom system [1].

If we assume that only one resonator mode is of interest and if we apply the second quantization for the electromagnetic field, we can describe the circuit by the Jaynes Cummings Hamiltonian (see Fig. 2.3)

$$H'_{JC} = \hbar\omega_r \left(a^\dagger a + \frac{1}{2}\right) + H_{qubit} + \hbar g \left(a^\dagger \sigma_- + a\sigma_+\right), \tag{2.2}$$

where we have used the lowering/raising operator $a/a^\dagger$. If we use for the Cooper pair box the Hamiltonian $H_{qubit} = \frac{\hbar\omega_{01}}{2}\sigma_z$ as in Eq. 2.1, we can diagonalize the Jaynes Cummings Hamiltonian as shown in [1] and we find the dressed states

$$|+,n\rangle = \cos\theta_n\,|1,n\rangle + \sin\theta_n\,|0,n+1\rangle \quad \text{and} \quad |-,n\rangle = -\sin\theta_n\,|1,n\rangle + \cos\theta_n\,|0,n+1\rangle,$$

with the angle $\tan 2\theta_n = (2g\sqrt{n+1})/(\omega_{01} - \omega_r)$.

There are now two distinct regimes of interest: one is the resonant point $\omega_r = \omega_{01}$, where the qubit is maximally coupled (with g) to the resonator and vacuum Rabi mode

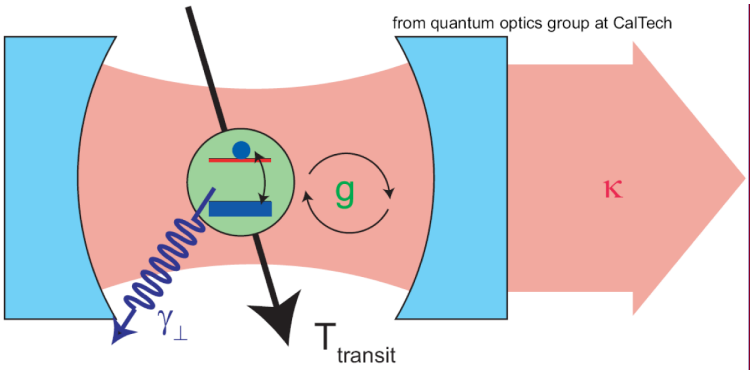

Figure 2.3: The sketch illustrates a cavity coupled to a qubit. The qubit couples to the field in the cavity with a rate g. Decoherence is caused by photons which escape the cavity through the mirror at a rate κ and by modes which are not confined by the resonator at a rate $\gamma_\perp$. The picture is from [1]

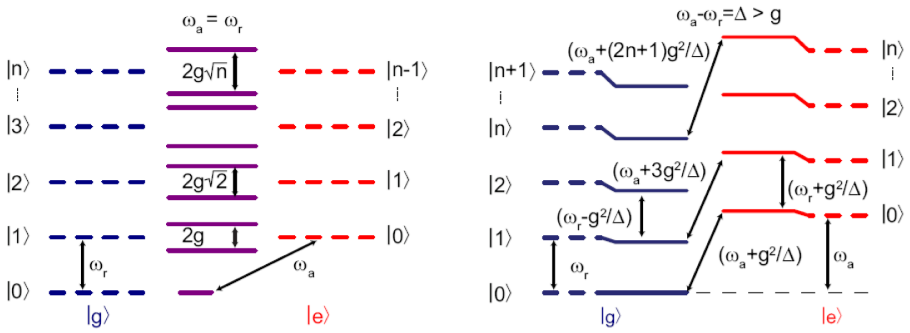

Figure 2.4: The graphic gives the energy level diagram for a qubit, which has same transition frequency as the resonator, and for a qubit, which is detuned form the resonator. The dashed lines show the energy levels for a not interacting qubit cavity system. The full lines indicates the energy levels for a system with a finite coupling rate g. The picture is from [1]

splitting equal to $2\sqrt{n}$ is observed [27]. The other is at large detunings $\omega_{01} - \omega_r >> g$ see Fig. 2.4. In the following we will discuss the second case.

For further calculations it would be nice if the Fock space for the photons and the Hilbert space for qubits are decoupled. For this we would have to eliminate the terms $a^{(\dagger)}\sigma_{(-)+}$. Indeed this can be achieved for large detuning $g\sqrt{n+1} << |\omega_{01} - \omega_r|$, if we apply the transformation $UH'U^\dagger$ with $U = \exp\left(g(a\sigma_+ - a^\dagger\sigma_-)/(\omega_{01} - \omega_r)\right)$ and neglect terms with higher then second order in $g/(\omega_{01} - \omega_r)$, see [1]. For the dispersive limit this yields the very useful expression for the dispersive Jaynes-Cummings Hamiltonian given by

$$H_{JC} = \hbar\omega_r a^\dagger a + \hbar\left(\frac{\omega_{01}}{2} + \frac{g^2}{\omega_{01} - \omega_r}\left(a^\dagger a + \frac{1}{2}\right)\right)\sigma_z. \tag{2.3}$$

The first term of the Jaynes Cummings Hamiltonian represents the energy of the field in the cavity, the second the energy of the qubit, the third the AC stark shift and the fourth the Lamb shift. The Lamb shift describes the interaction of the qubit with the resonators vacuum mode. One can clearly see that the Lamb and AC stark shift shifts the dressed energy level compared to the case where the qubit is decoupled form the cavity.

2.3 Coherent control

Here we explain how coherent control of the qubit is realized. If the cavity is irradiated by a microwave sigmal with a frequency ω_{drive} and an envelope $\epsilon(t)$, we will have to add the term

$$H'_{\text{drive}} = \hbar\epsilon(t)\left(a^\dagger \exp\left(-i\omega_{\text{drive}}t\right) + a\exp\left(i\omega_{\text{drive}}t\right)\right),$$

to the Jaynes Cummings Hamiltonian H'_{JC} from Eq. (2.2). Applying the transformation from above $U\left(H'_{JC} + H'_{\text{drive}}\right)U^\dagger$ and assuming that the driving frequency ω_{drive} is close to the transition frequency yields the driven Jaynes Cummings Hamiltonian

$$H_{JC} = \hbar\left(\omega_r + \omega_{\text{drive}}\right)a^\dagger a + \frac{\hbar}{2}\left(\omega_{01} + \frac{2g^2}{\omega_{01} - \omega_r}\left(a^\dagger a + \frac{1}{2}\right)\right)\sigma_z +$$
$$+\frac{\hbar}{2}\frac{2g\epsilon(t)}{\omega_{01} - \omega_r}\left(\sigma_x\cos\varphi + \sigma_y\sin\varphi\right),$$

where the phase of the driving field is given by φ. Obviously the driving induces Rabi rotations of the qubit. The rotation axis for the Rabi process is given by the phase φ and the rotation rate by the amplitude of the driving pulse. Moreoverit can be seen that a detuning from the transition frequency $\left(\omega_{01} + 2g^2\left(a^\dagger a + \frac{1}{2}\right)/(\omega_{01} - \omega_r)\right)$ induces σ_z rotations. This enables us to perform arbitrary unitary operations on the qubit. Since the qubits transition frequency is far detuned from the resonator the driving field will only virtually populate the resonator with a small average photon number and therefore not cause any dephasing [28]. This is important to be able to perform high fidelity operations.

2.4 Qubit-qubit coupling

If two qubits are placed in the resonator they can interact with each other. If they are in resonance with the cavity's mode, they will exchange with each other photons, mediated

by the cavity due to vacuum Rabi processes. This yields a qubit interaction rate of the order of $2g$. Possibilities to realize this coupling are tunable resonators or flux lines among others [28].

On the other hand for our experiment more important is the interaction of the qubits by the exchange of a virtual photon. If two qubits are in resonance with each other and strong detuned form the cavity frequency, they can exchange virtual photons with the resonator, and therefore interact with each other even though they are located on a microscopical distance in the resonator.

To find the Jaynes Cummings Hamiltonian for such a detuned two qubit system we can apply the transformation $U = \exp\left(g^A(a^\dagger\sigma_-^A - a\sigma_+^A)/(\omega_r - \omega_{01}^A) + g^B(a^\dagger\sigma_-^B - a\sigma_+^B)/(\omega_r - \omega_{01}^B)\right)$ on the two qubit Hamiltonian, as described in [28]. This yields under the assumption that we can neglect therms with higher than second order in $\frac{g^i g^j}{(\omega_r - \omega_{01}^i)(\omega_r - \omega_{01}^j)}$ the new Hamiltonian without $a^{(\dagger)}\sigma_{+(-)}$ terms

$$H = \hbar\omega_r a^\dagger a + \hbar\omega_{01}^A \sigma_z \otimes id + \hbar\omega_{01}^B id \otimes \sigma_z + \hbar J(\sigma_+ \otimes \sigma_- + \sigma_- \otimes \sigma_+).$$

For simplicity we have introduced the coupling therm $J = g^A g^B(1/(\omega_{01}^A - \omega_r) + 1/(\omega_{01}^B - \omega_r))$. For this Hamiltonian the states $|01\rangle$ and $|10\rangle$ are not eigenstates any longer. However, we can easily find the new eigenvalues and eigenstates to the Hamiltonian

$$H = \frac{\hbar}{2}\begin{pmatrix} \omega_{01}^A + \omega_{01}^B & 0 & 0 & 0 \\ 0 & -\omega_{01}^A + \omega_{01}^B & J & 0 \\ 0 & J & \omega_{01}^A - \omega_{01}^B & 0 \\ 0 & 0 & 0 & -\omega_{01}^A - \omega_{01}^B \end{pmatrix},$$

$$\text{as } E_\pm = \pm\sqrt{J^2 + \frac{\Delta_{A,B}^2}{2}} \text{ and}$$

$$|\psi_\pm\rangle = \frac{1}{N}\left(\frac{\Delta_{A,B} \pm \sqrt{(2J)^2 + \Delta_{A,B}^2}}{2J}|0\rangle + |1\rangle\right),$$

where the detuning between the two qubits is given by $\Delta_{A,B} = \omega_{01}^A - \omega_{01}^B$ and N is the normalization constant. This is analogous to the double well potential where a similar splitting occurs.

It can easily be seen that the qubit-qubit interaction can be suppressed by a strong detuning between the two qubits. In this case energy conservation does not permit a flip-flop interaction. A very intuitive way to understand how a detuning of the two qubits prevent flip-flop interactions is by changing to the rotating frame of the first qubit ω_A. In this frame a coupling to the second qubit is suppressed by fast rotating oscillations $\omega_B - \omega_A$.

2.5 Transmon

We have seen in Section 2.1 that the Cooper pair box is charge sensitive. Since usually charge noise is low frequent and therefore adiabatic this fluctuations will not induce transitions from the excited to the ground state but they will cause a random phase shift,

a) 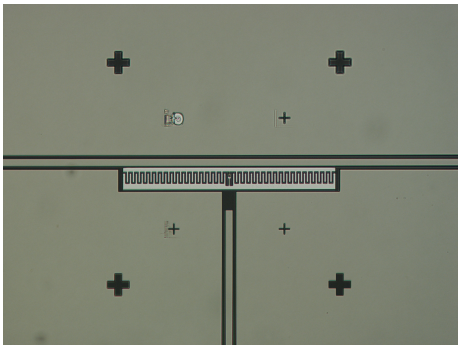 b) 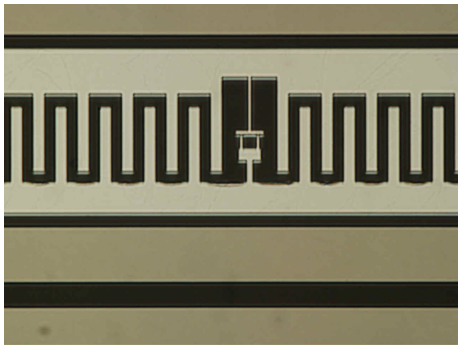

Figure 2.5: The microscopic images show a transmon qubit. On the left hand side we can clearly see how the reservoir is coupled to ground by a capacitor. The transmission line coming from the bottom is a charge gate line. On the right hand side we can recognize the SQUID loop. The pictures have been taken by Martin Goeppel.

which yields to decoherence. In fact this is the limiting factor for dephasing and hence T_2. Therefore it has been of general interest to modify the Cooper pair box in such a way that it becomes insensitive to charge noise. This has been achieved with the proposal of a transmission line shunted plasma oscillation qubit (transmon) [9]. However, the price for the charge insensitivity is paid by reducing the anharmonicity. Nevertheless, the anharmonicity remains sufficient for selective addressing of the 01 transition. We will now explain how this is done.

Charge insensitivity is realized by adding a large additional capacity C_B between the Cooper pair reservoir and ground see Fig. 2.5. It can be shown [9] that the Hamiltonian becomes the same as for the Cooper pair box but with a much larger capacitance

$$H = \frac{2e^2}{C_J + C_g + C_B} \sum_N (N - N_g)^2 \left|N\right\rangle \left\langle N\right| - \frac{E_J}{2} \sum_N \left(\left|N+1\right\rangle \left\langle N\right| + \text{H.c.}\right), \tag{2.4}$$

if we add the capacity C_B. Charge insensitivity is observed in the regime $E_C << E_J$. If we use Mathieu functions $\tilde{m}_\mu[x]$ the Hamiltonian can be diagonalized in the phase basis [9] and the eigenvalues are given by

$$E_m(N_g) = E_C \tilde{m}_{2(N_g + k(m,N_g))}[-E_J/(2E_C)].$$

The eigenvalues become less sensitive to charge noise $\frac{\partial E_m}{\partial N_g}\delta N_g$ with increasing $\frac{E_J}{E_C}$. On the other hand the energy spacing between energy levels becomes more harmonic, which causes problems for selective addressing of the 01 transition. One can show that the first three energy levels are equally spaced for a ratio of $\frac{E_J}{E_C} \approx 9$ and becomes again anharmanic for larger $\frac{E_J}{E_C}$. For very large $\frac{E_J}{E_C}$ ratio the anharmonicity decreases and approximates 0 again. It is possible to engineer a $\frac{E_J}{E_C}$ ratio which satisfy both a sufficient anharmonicity as well as charge insensitivity as shown in Fig. 2.6. Since the Josephson energy E_J depends on the flux Φ through the SQUID loop the separation of the energy level is depending on Φ, this is shown in Fig. 2.7.

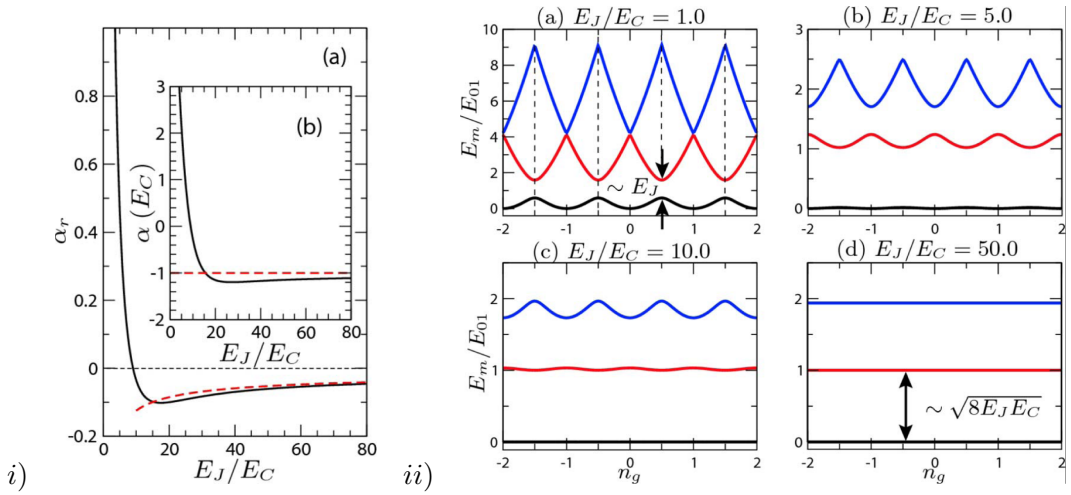

Figure 2.6: The left graph show the relative $\alpha_r = \frac{E_{12}-E_{01}}{E_{01}}$ (a) and absolute $\alpha_r = E_{12} - E_{01}$ (b) anharmonicity for a transmon qubit as a function of $\frac{E_J}{E_C}$. The middle graph show the energy diagram for the first three energy levels. On can recognize that the charge insensitivity increases with smaller α_r. The pictures are taken from [9].

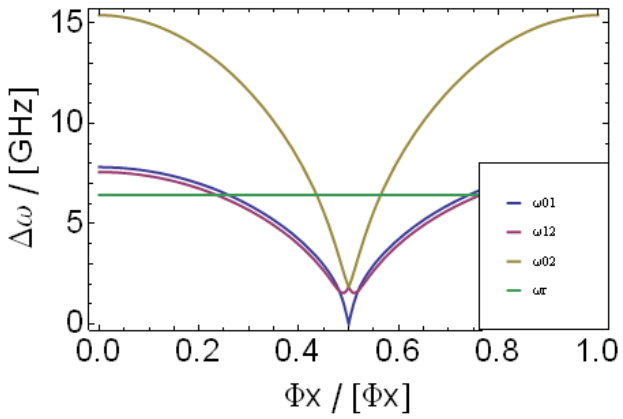

Figure 2.7: The graph shows the frequency for different transitions as a function of the flux through the SQUID loop.

2.6 Transmon coupled to a cavity

Even though, that the transmon's anharmonicity is large enough to prevent population of higher energy levels we can not neglect the presence of these levels since they can be populated virtually.

The Jaynes Cummings Hamiltonian can easily be expanded for an arbitrary number of energy levels by writting

$$\tilde{H}_{JC} = \hbar \sum_j \omega_j |n\rangle \langle j| + \hbar\omega_r a^\dagger a + (\hbar g_{j,j+1} |j\rangle \langle j+1| + \text{H.c.}),$$

where we have taken into account only transition between neighboring energy levels and $|n\rangle$ are eigenfunctions for the transmon Hamiltonian Eq. 2.4.

It would be very nice to reduce the Hilbert space again to a two level system so that we can use the results obtained previously in the Cooper pair box. A elegant way to separate the Hamiltonian in an effective Hamiltonian H_{eff} and an remaining Hamiltonian H_{rem} is by applying a canonical transformation

$$H = e^{\sum_j \frac{g_{j,j+1}}{\omega_j - \omega_{j+1}} |j+1\rangle\langle j| - \text{H.c.}} \tilde{H} e^{(\sum_j \frac{g_{j,j+1}}{\omega_j - \omega_{j+1}} |j+1\rangle\langle j| - \text{H.c.})^\dagger}$$

as demonstrated in [9]. Similarly to the Cooper pair box the effective Hamiltonian takes the simple form

$$H_{eff} = \hbar \left(\chi(a^\dagger a + \frac{1}{2}) + \frac{\omega_{01}}{2} \right) \sigma_z + \hbar\omega_r' a^\dagger a.$$

In the effective Hamiltonian we have used the renormalized frequency

$$\omega_r' = \omega_r - \chi_{12}/2.$$

The effective dispersive shift is

$$\chi = \chi_{01} - \chi_{12}/2$$

with the dispersive shift for the jm transition given by $\chi_{j,m} = g_{j,m}^2/(\omega_{j,m} - \omega_r)$. These renormalized frequencies and the effective shift take the higher energy levels into account. For more details we refer to [9].

2.7 Measurement process

In this section we will describe how the readout of the qubit state is realized.

As mentioned above the resonator is a superconducting coplanar wave guide, which is capacitively coupled to a wave guide, for driving the resonator, and to an other wave guide, for readout. Dividing the resonator into infinitesimal elements allows us to rewrite the resonator as a LCR circuit [24] (Fig. 2.8). The transmission as a function of frequency has has the well known Lorentzian shaped resonance

$$|t(\omega)|^2 = \frac{(\omega_r)^2}{4Q^2(\omega - \omega_r)^2 + (\omega_r)^2}$$

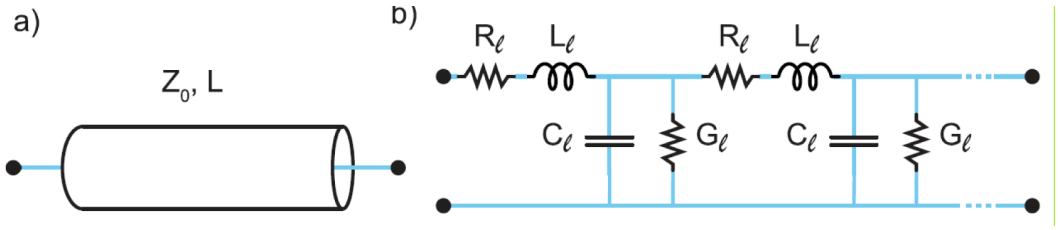

Figure 2.8: The left picture shows a transmission line. The right picture gives an equivalent network for the transmission line. The pictures are taken from [24].

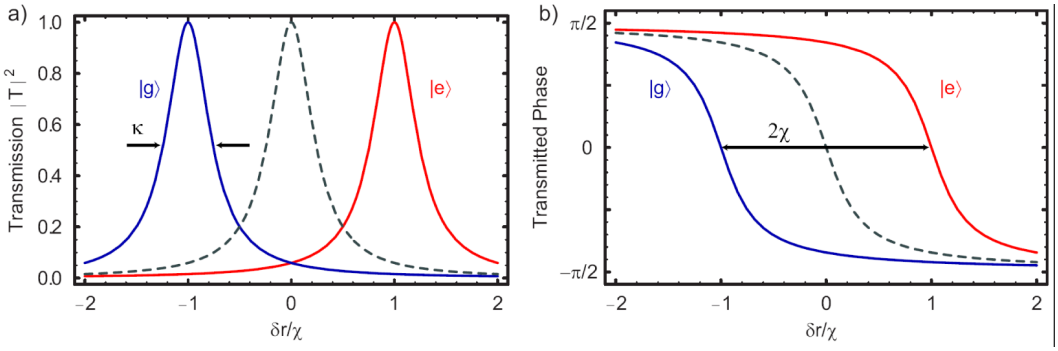

Figure 2.9: The left plot shows the transmission of a microwave passing through the resonator as a function of the frequency. The resonance for the ground state (blue) is shifted by χ toward lower frequencies and the resonance for the exited state is shifted by the same amount toward higher frequencies. The other graph gives the corresponding phase. The pictures are taken from [1].

with half width at half maximum equal to $\omega_r/(2Q)$, where the resonator quality factor is Q. The phase of the transmitted microwave on the other hand has an arctan dependancy

$$\varphi(\omega, \omega_r) = \arctan\left(\frac{2Q(\omega - \omega_r)}{\omega_r}\right)$$

and picks up a phase shift of π when the frequency passes through the resonance. This is total analogous to optical cavities.

As we have seen by deriving the dispersive limit of the Jaynes-Cummings Hamiltonian the presence of the qubit induces a AC Stark shifts $\left(\frac{g^2}{\Delta} a^\dagger a \sigma_z\right)$ of the resonator's bare frequency by $\pm\chi$ depending on the qubit's state. This yield the response as given in (Fig. 2.9).

If we measure the amplitude of the transmitted field at the resonator frequency $\omega_{|0\rangle}$, we can find maximal transmission coefficient for the qubit in the ground state and minimal transmission coefficient for the qubit in the excited state (Fig. 2.9). On the other hand if we measure at bare resonator frequency we can find a maximal phase shift 2ϕ, with phase $-\phi$ for the ground state and ϕ for the excited state. For an arbitrary measurement frequency ω we can find the measurement operator

$$M = (\varphi(\omega, \omega_r + \chi) - \varphi(\omega, \omega_r - \chi)) \frac{1 - \sigma_z}{2},$$

where we have set the phase for the ground state equal zero. It is pointed out that this measurement operator M commutes with the Jaynes Cummings Hamiltonian H_{JC}. Therefore the measurement is invariant under the time evolution and we call it quantum non demolition measurement.

2.8 Decoherence

So far we have assumed that the qubit cavity system does not interact with the environment. In this section we will discuss time evolution of the qubit in an open system.

As explained in the appendix 5.5, if our system is open, the time evolution of the density matrix is not given any more by the von Neumann equation but by the Master equation. Since we have a two level system the Lindblad operator will consist of maximally 4 super operators. One of the super operator ($[H, .]$) comes from the Hamiltonian H for the closed system, one ($L[a]$) satisfies the fact that our cavity looses photons over the capacities C_{in}/C_{out}, one ($L[\sigma_-]$) takes into account energy relaxation of the qubit and the last one ($L[\sigma_z]$) describes acquisition of a random phase. The Master equation is then given by [29]

$$\frac{d\rho}{dt} = -\frac{i}{\hbar}[H, \rho] + \kappa L[a]\rho + \gamma_1 L[\sigma_-]\rho + \frac{\gamma_\phi}{2} L[\sigma_z]\rho,$$

The super operators $L[A]$ are defined by

$$L[A] = A\rho A^\dagger - \frac{1}{2}A^\dagger A\rho - \frac{1}{2}\rho A^\dagger A.$$

This differential equation can be solved by changing into the Liouville space.

For the energy relaxation the ultimate limit would be given by the Purcell effect. The energy relaxation rate is then determined by $\gamma_\kappa = \kappa \frac{g_{01}^2}{\Delta_o^2}$ [9]. Most recently the limit of T_1 due to the Purcell effect has been achieved experimentally [30]. In [9] it is estimated that high frequent charge noise yields to relaxation times T_1 as long as 1 s this is basing on the charge noise insensitivity of the transmon and the fact that the noise has a $1/f$ behavior. Previously we have seen that the Josephson energy and hence the qubit transition frequency is depending on the flux through the SQUID loop. High frequency fluctuations in the magnetic field may cause a decay as well. In [9] an estimation for T_1 can be found of the order of micro seconds (depending on the flux).

The dephasing T_2 can be caused by several effects we will now discuss two on them. According to [9] the most important noise factor is given by current noise through the Josephson junctions and T_2 is supposed to be on the order of few μs. Current noise comes from trapping and releasing of charge in the Josephson junctions, which changes the Josephson energy and hence dephase the qubit. Another noise source is low frequency noise in the magnetic field. In this regime the qubit is adiabaticly detuned from resonance and no energy relaxation is induced. Since the qubit is randomly detuned it will pick up an additional phase. However current samples have T_1 and T_2 well below the estimated values.

Chapter 3

Tomography of single qubit states

I will here discuss the tomography of one qubit. This is important because it proves that tomography in principle works in our system. Furthermore, there are many interesting phenomena which can be observed on one qubit that require tomography. In addition it is important to determine the fidelity of one qubit gates i.e. the phase and Hadamard gate, if we want to use the system for quantum information technology. Moreover, single qubit operations like Rabi oscillations and Ramsey fringes are nice experimental demonstrations of the ability to manipulate quantum mechanical systems. Besides that, conclusions made in this chapter will be useful to implement tomography on several qubit systems.

3.1 Theory

This section gives a theoretical introduction on tomography for one qubit. State tomography can be explained in a very intuitive picture using the Bloch sphere. In the Bloch sphere picture operations are isomorphic to affine mappings of the Bloch sphere onto itself. A mathematically more convenient picture, which uses density matrices, will be discussed in some details. In addition we will discuss the L_1 norm and the fidelity, which both measure the distances between quantum states, which is important if we want to discuss deviation between theory and experiment. Furthermore, we will also derive a measurement process, which can be performed even if the tomography pulses are unknown operations. Once we understand state tomography we are enable to do process tomography.

3.1.1 Bloch sphere picture for quantum state tomography

The Bloch sphere picture is a very illustrative way to describe the state of a qubit. The Bloch sphere is a picture which identifies an arbitrary density matrix ρ with an point on/in the unit sphere (Bloch sphere). However, as we will see the mapping is not strictly unique. Nevertheless, this picture is sufficient for almost all applications. Furthermore, the Bloch picture allows us to visualize the outcome of operations on an arbitrary state. This is especially useful for an intuitive understanding.

The Bloch picture can be introduced by some simple thoughts. The wave function of a two level system is given by $|\Psi\rangle = a\,|0\rangle + b\,|1\rangle$. The normalization condition and the fact that the eigenstates are orthogonal yield the property $1 = |a|^2 + |b|^2$. It is convenient to

parametrize a and b in spherical coordinates $a = e^{i\delta}\cos\left(\frac{\theta}{2}\right)$ and $b = e^{i\delta}e^{i\varphi}\sin\left(\frac{\theta}{2}\right)$. In this notation θ is the azimuthal angle, φ is the polar angle and δ is a global phase, which is of no interest since δ is annihilated by forming the expectation value. It can immediately be seen that all these points lie on the surface of a three dimensional unity sphere, the Bloch sphere.

Now we will show that simple operations on an state can be described in the Bloch picture by rotations. If operations, with exception those describing interactions with the environment, are applied on an arbitrary pure state, the resulting state will be again a pure state. In the Bloch picture, an operation on a point on the Bloch sphere gives again a point which lies on the sphere. As it can be looked up in any book on linear algebra the set of operations which maps linearly the unit sphere on it selfs and conserves the orientation is given by the rotation group $SO(3)$.

As mentioned above this simple picture is not totally true. Operations on a state in a two level system are described by $SU(2)$. On the other hand $SU(2)$ is not isomorphic to $SO(3)$ but $SU(2)/Id \cong SO(3)$. Therefore, rotations of 2π pick up the phase -1, hence rotations have to be at least 4π to reproduce the identity. However, in most cases this additional phase is not of interest, an example where it is obtained is given in [31].

Now we will illustrate the tomography process, in the Bloch sphere picture, using the tomography pulses id, $\left(\frac{\pi}{2}\right)_x$ and $\left(\frac{\pi}{2}\right)_y$. The id pulse is just a identity operation on the Bloch sphere. The $\left(\frac{\pi}{2}\right)_x$ and $\left(\frac{\pi}{2}\right)_y$ pulses on the other hand transform the qubit's state in to the equally super position state $|0\rangle + |1\rangle$ and $|0\rangle + i\,|1\rangle$. This pulses will also be used for our experiment.

We want to determine the state $|\psi\rangle$ which is equivalent to the Bloch vector $r = (r_x, r_y, r_z)$. It is important to mention that this state can be reproduced as many times as we like. Therefore we can perform measurements several times, average the outcome and estimate hereby the expectation value. The measurement defines our quantization axis, which is chosen to be the z axis.

Applying the first tomography pulse, which is the identity, and measuring the expectation value is equivalent to projecting the the vector r on the z axis.

$$p_z = |\langle 1|\psi\rangle|^2 = |\langle 1|\,(a\,|0\rangle + b\,|1\rangle)|^2 = |b|^2 = \sin\left(\frac{\theta}{2}\right) = \frac{1-\cos\left(\frac{\theta}{2}\right)}{2} = \frac{1-r_z}{2}$$

This yields perfect knowledge (up to statistical uncertainty) of the p_z component of the Bloch vector. On the other hand a maximal uncertainty in the r_x and r_y component remains due to the Heissenberg principle see Fig. 3.1.

Additional rotations on the Bloch vector give the opportunity to determine the other components of the Bloch vector (r_x, r_y). To determine the r_x component we apply first a $R_y\left(\frac{\pi}{2}\right)$ rotation around the y axis. This rotation maps the Bloch vector (r_x, r_y, r_z) on $(r_z, r_y, -r_x)$. The measurement of this new state yields $p_x = \frac{1+r_x}{2}$. Analogously a $R_x\left(\frac{\pi}{2}\right)$ rotation gives $(r_x, -r_z, r_y)$ the response $p_y = \frac{1-r_y}{2}$. These three rotations and coresponding measurements determine the initial state of the qubit up to a statistical uncertainty coming form the measurement process.

Following the discussion given in [6] we will now describe processes which take interactions with the environment into account. This can be done in a elegant way using the Bloch picture. During a decoherence process points from the surface of the Bloch sphere

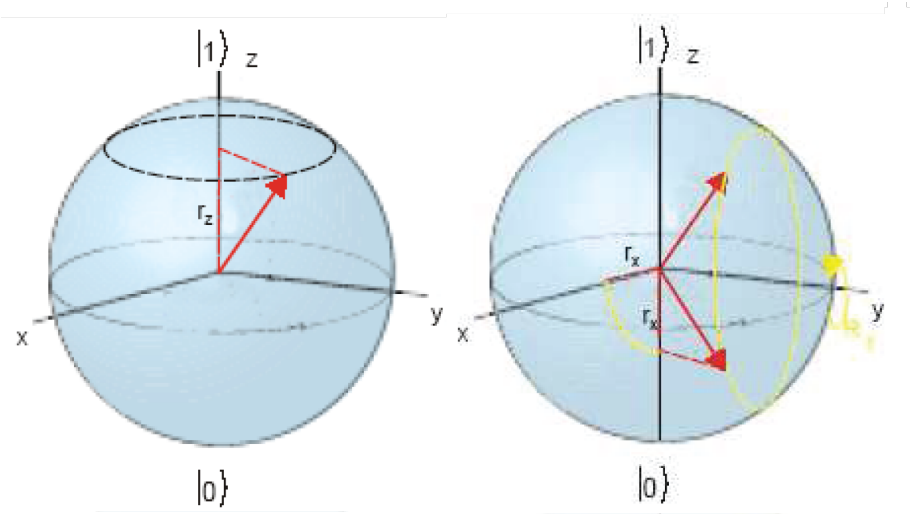

Figure 3.1: The pictures show the tomography on a qubit. On the left hand side the qubit state, which is indicated by the red vector (Bloch vector), is illustrates. The average of the measurement is then given by the projection on the quantization axis (z axis), which determines the r_z component. However, due to Heisenberg's uncertainty principle a maximal indeterminacy in the r_x and r_y components remains (black circle). On the right hand side the Bloch vector is rotated around the y axis by $\frac{\pi}{2}$ before performing the measurement (yellow circle). This gives the opportunity to determine the r_y component.

will be mapped into the inside of the Bloch sphere. This processes can be described by an affine function which maps the unit ball into itself.

$$\vec{r} \mapsto A\vec{r} + \vec{c}$$

here A is a real 3x3 matrix and $\vec{c}$ is a translation. The exact form of this mapping can easily be found by using the operator sum representation and changing into the Bloch vector picture or can be looked up in [6]. Using polar decomposition the matrix A can be written as $A = OP$ with $O \in SO(3)$ an orthogonal matrix and P a positive definite matrix. The transformation as written above has now a very intuitive meaning: first the positive definite matrix P deformes the Bloch sphere according to T_1 and T_2 and the additional orthogonal matrix O rotates the Bloch sphere in respect of dephasing and finally the translation $\vec{c}$ shifts the whole sphere which satisfies the relaxation T_1.

3.1.2 Alternative picture for quantum state tomography

Doing QST in R^3 maybe intuitive and geometrically simple but calculations become mathematically difficult. Furthermore the Bloch sphere picture breaks down if entanglement is taken into consideration. However, if operations are done in $SU(2)$ the mathematical tools stays rather simple and an upscaling can be done easily.

If we want to fully describe the state of a qubit the density matrix has to be determined. The density matrix ρ is a hermitian 2x2 matrix, which is positive definite and has trace 1. In the basis $|0\rangle \cong (1,0)^T$ and $|1\rangle \cong (0,1)^T$ the density matrix has the form

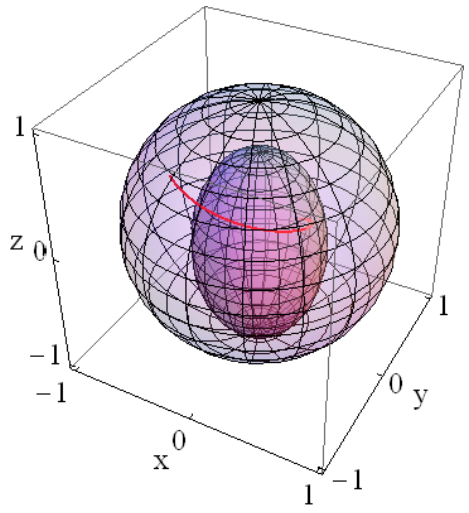

Figure 3.2: The picture shows systematically how the set of Bloch vectors evolves if interactions with the environment are taken into account. Here the starting set is indicated as the set of pure states (semi transparent ball). After applying an affine transformation a codomain, which is represented by the cigar shaped surface, can be obtained. It can be seen that this transformation contracts and rotates (Red lines) the initial set. The resulting codomain will not be a set of pure states any more ($|\vec{r}| < 1$).

$$\begin{pmatrix} \rho_{00} & \rho_{01} \\ \rho_{10} & \rho_{11} \end{pmatrix}$$

Since the trace is always $Tr(\rho) = 1$, the density matrix's entries have to satisfy the condition $\rho_{00} + \rho_{11} = 1$. A more elegant way to write the density matrix is given by $\rho = \frac{1}{2}\left(1 + \sum_{k=x,y,z} r_k \sigma_k\right)$, where $Tr(\rho) = 1$ is already taken into account and σ_k denotes the Pauli matrices. The vector $\vec{r}$ is equivalent to the Bloch vector.

The task is now to determine $\vec{r}$. The measurement operator σ_z yields the equation $p_0 = Tr(\rho|1\rangle\langle 1|)$, which measures r_z. Where p is the expectation value for the measurement. Two more equations can be found by applying known operations U_k on ρ. Examples and a good choice of U_k will be discusses later one in this section. In total this yields a system of linear equations

$$| \; p_k = Tr(U_k \rho U_k^\dagger |1\rangle\langle 1|) \; |_{k=0,1,2} \; .$$

If the rotations have been chosen in a proper way this system of equations will have kernel zero. It can easily be seen that a rotation of the density matrix is equivalent to a rotation of the measurement operator since the trace is commutative

$$p_k = Tr(U_k \rho U_k^\dagger |1\rangle\langle 1|) = Tr(\rho U_k^\dagger |1\rangle\langle 1| U_k).$$

Again it is pointed out that the operation U_k has to be known. For simplicity we assume that T_1 and T_2 are negligible on the time scale rotations are applied.

The Hamiltonian, which describes operation on the qubit, is given by the Jaynes Cummings Hamiltonian, written in the rotating frame, for the dispersive limit

$$H_{\text{rot}} = \hbar\left(\chi(a^\dagger a + \frac{1}{2}) + \frac{\omega_{01}}{2} - \frac{\omega_{\text{drive}}}{2}\right)\sigma_z + \hbar\frac{g_{01}(t)}{\Delta}\left(\epsilon_x(t)\sigma_x + \epsilon_y(t)\sigma_y\right) +$$

$$+\hbar\left(\epsilon_x(t) + \epsilon_y(t)\right)\left(a^\dagger + a\right) + \hbar\left(\omega_r - \omega_{\text{drive}}\right)a^\dagger a.$$

The low anharmonicity of the transmon is taken into account by introducing the renormalized frequencies $\omega_r' = \omega_r - \chi_{12}/2$, with the effective dispersive shift $\chi = \chi_{01} - \chi_{12}/2$, see [9]. The first term represents σ_z rotations and can be chosen to be zero if the frequency of the driving pulses ω_{drive} matches the qubit transition frequency plus the AC stark shift and the Lamb shift, the second therm represents σ_x and σ_y rotations and can be controled by the envelope ϵ_x and ϵ_y of the driving pulse, the third term represents a population of the cavity and the last one stands for the energy of the field inside the cavity. However, for the tomography pulses just the first two terms are of interest. Therefore, we rewrite the Hamiltonian for operation on the qubit as

$$H = \frac{\hbar\Delta}{2}\sigma_z + \frac{\hbar\Omega_x}{2}\sigma_x + \frac{\hbar\Omega_y}{2}\sigma_y,$$

where $\Delta = \chi(a^\dagger a + \frac{1}{2}) + \frac{\omega_{01}}{2} - \frac{\omega_{\text{drive}}}{2}$ is the detuning from resonance, $\Omega_i = \frac{2g_{01}\epsilon(t)}{\Delta}$ and $\sqrt{\Omega_x^2 + \Omega_y^2}$ is the Rabi frequency.

The Von-Neumann equation determines the density matrix's evolution $\frac{\partial\rho}{\partial t} = [H, \rho]$. For piecewise time independent Hamiltonian the evolution is given by

$$\rho(t) = \mathrm{T}\exp\left[-\frac{i}{\hbar}\int dt' H(t')\right]\rho\mathrm{T}^\dagger\exp\left[\frac{i}{\hbar}\int dt' H(t')\right]$$

$$= \left(\prod_{n=1,2,\ldots,N}\exp\left[-i\frac{H_n}{\hbar}\Delta t_n\right]\right)\rho\left(\prod_{n=N,N-1,\ldots,1}\exp\left[i\frac{H_n}{\hbar}\Delta t_n\right]\right),$$

where T is the time order operator and the system evolves under the Hamiltonian H_n for the duration Δt_n.

Now that we know the qubit evolution under a driving pulse we can write down the system of equations $\mid p_k = Tr(U_k\rho U_k^\dagger|1\rangle\langle 1|)\mid_{k=0,1,2}$. In absence of decoherence we can write a sequence of operations on the qubit by one unitary operator

$$U_k(\Omega_{x,k}, \Omega_{y,k}, \Delta_k) = \exp\left[-i\frac{\Omega_{x,k}\sigma_x + \Omega_{y,k}\sigma_y + \Delta_k\sigma_z}{2\hbar}\tau\right]$$

Using the properties for the Pauli matrices we can write the operator in the intuitive way

$$U_k = \mathrm{id}\cos(\Omega) - i\vec{\sigma}\cdot\vec{n}\sin(\Omega),$$

where Ω_k is the Rabi frequency $\sqrt{\Delta_k^2 + \Omega_{x,k}^2 + \Omega_{y,k}^2}$ and $\vec{n}$ is the rotation axis. The system of equations greatly simplifies if we parametrize the density matrix by

$\rho = \frac{1}{2}\left(1 + \sum_{k=x,y,z} r_k \sigma_k\right)$. The quantities r_k are equal to the Bloch vector components. The system of linear equations can easily be solved by using the identity $p_k \mapsto p_k \vec{e}_k$ and $r_k \mapsto r_k \vec{e}_k$ (the vector $\vec{e}_k$ is the unity vector with 1 at the k^{th} position but zero elsewhere) and we obtain

$$\vec{p} = \frac{1}{2} \underbrace{\begin{pmatrix} \frac{\Omega_{y,1}\sin\sqrt{\Omega_{x,1}^2+\Omega_{y,1}^2}}{\sqrt{\Omega_{x,1}^2+\Omega_{y,1}^2}} & \frac{-\Omega_{x,1}\sin\sqrt{\Omega_{x,1}^2+\Omega_{y,1}^2}}{\sqrt{\Omega_{x,1}^2+\Omega_{y,1}^2}} & -\cos\sqrt{\Omega_{x,1}^2+\Omega_{y,1}^2} \\ \frac{\Omega_{y,2}\sin\sqrt{\Omega_{x,2}^2+\Omega_{y,2}^2}}{\sqrt{\Omega_{x,2}^2+\Omega_{y,2}^2}} & \frac{-\Omega_{x,2}\sin\sqrt{\Omega_{x,2}^2+\Omega_{y,2}^2}}{\sqrt{\Omega_{x,2}^2+\Omega_{y,2}^2}} & -\cos\sqrt{\Omega_{x,2}^2+\Omega_{y,2}^2} \\ \frac{\Omega_{y,3}\sin\sqrt{\Omega_{x,3}^2+\Omega_{y,3}^2}}{\sqrt{\Omega_{x,3}^2+\Omega_{y,3}^2}} & \frac{-\Omega_{x,3}\sin\sqrt{\Omega_{x,3}^2+\Omega_{y,3}^2}}{\sqrt{\Omega_{x,3}^2+\Omega_{y,3}^2}} & -\cos\sqrt{\Omega_{x,3}^2+\Omega_{y,3}^2} \end{pmatrix}}_{A} \vec{r} + \frac{\vec{e}_1+\vec{e}_2+\vec{e}_3}{2}.$$

The solution is then simply given by

$$\vec{r} = A^{-1}(\vec{p} - \frac{\vec{e}_1+\vec{e}_2+\vec{e}_3}{2}).$$

The condition for a complete set of tomography pulses is then equivalent to the condition $\det(A) \neq 0$.

For illustrative purposes and because the experiment will use Id, $\left(\frac{\pi}{2}{}_x\right)$ and $\left(\frac{\pi}{2}{}_y\right)$ pulse the tomography procedure will now be explained in more details for this kind of pulses.

The unknown density matrix $\rho = \frac{1}{2}\left(1 + \sum_{k=x,y,z} r_k \sigma_k\right)$ has to be determined. Applying no pulse yield the equation

$$p_0 = Tr(\rho \frac{1-\sigma_z}{2}) = Tr\left(\frac{1}{2}\left(1 + \sum_{k=x,y,z} r_k\sigma_k\right)\frac{1-\sigma_z}{2}\right) = \frac{1-r_z}{2},$$

where the property $\sigma_m\sigma_n = i\epsilon_{mnk}\sigma_k$ and the relation $|1\rangle\langle 1| = \frac{1-\sigma_z}{2}$ has been used.

For the $\frac{\pi}{2}{}_x$ pulse the expectation value is given by

$$p_x = Tr(\exp\left[-i\frac{\pi\sigma_x/2}{2\hbar}t\right]\rho\exp\left[i\frac{\pi\sigma_x/2}{2\hbar}t\right]\frac{1-\sigma_z}{2})$$

$$p_x = Tr\left(\exp\left[-i\frac{\pi\sigma_x/2}{2\hbar}t\right]\frac{1}{2}\left(1 + \sum_{k=x,y,z} r_k\sigma_k\right)\exp\left[i\frac{\pi\sigma_x/2}{2\hbar}t\right]\frac{1-\sigma_z}{2}\right)$$

$$p_x = Tr\left((1+i\sigma_x)\frac{1-\sigma_z}{2}(1-i\sigma_x)\frac{1}{2}\left(1 + \sum_{k=x,y,z} r_k\sigma_k\right)\right)$$

$$p_x = \frac{1+r_x}{2},$$

Where in addition the property $[\sigma_n, \sigma_m] = \delta_{nm}$ and the useful feature $\exp\left[-i\frac{\alpha}{2}\vec{\sigma}\cdot\vec{n}\right] = \cos\left[\frac{\alpha}{2}\right]\mathbf{1} - i\sin\left[\frac{\alpha}{2}\right]\vec{\sigma}\cdot\vec{n}$ has been used.

Analogously it can be found for the $\left(\frac{\pi}{2}\right)_y$ pulses that

$$p_y = \frac{1 - r_y}{2},$$

This measurement process fully determines any arbitrary state. For this case the A^{-1} matrix takes the simple form $A^{-1} = \begin{pmatrix} \frac{1}{2} & 0 & 0 \\ 0 & -\frac{1}{2} & 0 \\ 0 & 0 & -\frac{1}{2} \end{pmatrix}$.

3.1.3 Distance between density matrices

After measuring the density matrices it would be good to have a quantitative measure for the difference between the measured and the theoretical expected state. In quantum information the L_1 norm and the fidelity are the two most widely used measure for distance of quantum states. All in all the fidelity is a more often used method to calculate the distance between two states. On the other hand the L_1 norm remains a norm on the space of the hermitian matrices with trace one, where the fidelity can only be used for density matrices. In the following section we will describe the properties of the L_1 norm as well as the fidelity. The discussion is following ideas from [32] and [33].

L_1 norm:

The L_1 norm between the states ρ^a and ρ^b is defined by

$$D(\rho^a, \rho^b) = \frac{1}{2} Tr\left(|\rho^a - \rho^b|\right) = \frac{1}{2} Tr\left(\sqrt{(\rho^a - \rho^b)^\dagger (\rho^a - \rho^b)}\right).$$

This definition fulfills all requirements for being a metric; it is positive definite $D(\rho^a, \rho^b) \geq 0$ with $D(\rho^a, \rho^b) = 0$ if and only if (iff) $\rho^a = \rho^b$, is symmetric $D(\rho^a, \rho^b) = D(\rho^b, \rho^a)$ and satisfies the triangle inequality $D(\rho^a, \rho^b) \leq D(\rho^a, \rho^c) + D(\rho^b, \rho^c)$. A proof for these three properties of the L_1 norm and therefore a proof that L_1 is a metric can be found in [32].

The definition of the L_1 norm is motivated by the classical L_1 norm of two probability distribution $\{p_x\}$ and $\{q_x\}$ given by $D_{\text{classical}}(p, q) = \frac{1}{2} Tr(\sum_x |p_x - q_x|)$. For the case where the matrices ρ^a and ρ^b commute the classical and quantum mechanical definition are identical. We can see this by diagonalizing the matrices simultaneously $\rho^{a,b} = U^\dagger D^{a,b} U$ and we end up with the relation $\frac{1}{2} Tr\left(|\rho^a - \rho^b|\right) = \frac{1}{2} Tr\left(\sqrt{U^\dagger (D^a - D^b)^\dagger (D^a - D^b) U}\right)$ $= \frac{1}{2} Tr\left(U^\dagger \sqrt{(D^a - D^b)^\dagger (D^a - D^b)} U\right) = \frac{1}{2} \sum_k |\lambda_k^a - \lambda_k^b|$.

In the case of one qubit we can use the Bloch picture and the L_1 norm becomes

$$D(\rho^a, \rho^b) = \frac{|(\vec{r}^a - \vec{r}^b)\vec{\sigma}|}{4} = \frac{|\vec{r}^a - \vec{r}^b|}{2},$$

since the eigenvalues of $\vec{r}$ are $\pm\vec{r}$. The norm is equal to half the Euclidean distance of two points on the Bloch sphere.

In addition the L_1 norm has the useful property of being a metric even if we expand the definition to all hermitian matrices with trace one. It is important to have a metric

which is valid for arbitrary hermitian matrices because the tomography process will yield matrices which do not have to fulfill the requirements of being positive definite.

Fidelity:

The fidelity is the most widely used measure for comparing different density matrices. The fidelity is defined as

$$F(\rho^a, \rho^b) = Tr\left(\sqrt{\sqrt{\rho^a}\rho^b\sqrt{\rho^a}}\right).$$

In fact the quantum mechanical fidelity becomes equal to the classical one for the case where ρ^a and ρ^b commute.

The fidelity is symmetric and has values between $0 \leq F(\rho^a, \rho^b) \leq 1$, with equal zero iff ρ^a and ρ^b are lying in orthogonal spaces and equal one iff $\rho^a = \rho^b$. The fidelity is almost a metric. The quantity $\arccos\left(F(\rho^a, \rho^b)\right)$ on the other hand fulfills all requirements for a metric. For one qubit the quantity $\arccos\left(F(\rho^a, \rho^b)\right)$ has the intuitive meaning of being an angle between the two Bloch vectors $\vec{r^a}$ and $\vec{r^b}$. And we can immediately see that there is a close relation between the fidelity and the L_1 norm, at least for two one qubit density matrices. For the case of a pure state the fidelity is given by

$$F(\rho, |\Psi\rangle\langle\Psi|) = Tr\left(\sqrt{\left(\Sigma_i \left\langle\tilde{\Psi}_i\right| \rho \left|\tilde{\Psi}_i\right\rangle \left|\tilde{\Psi}_i\right\rangle \left\langle\tilde{\Psi}_i\right|\right) |\Psi\rangle\langle\Psi|}\right) = \sqrt{\langle\Psi|\rho|\Psi\rangle}.$$

In this case the fidelity is the square root of the overlap of the pure state $|\Psi\rangle\langle\Psi|$ and an arbitrary state ρ.

However, if we take the fidelity of matrices, which are not density matrices, the fidelity can become negative or larger than one. This makes it unfavorable for matrices, which are calculated by using a linear tomography procedure. As we will see later the most likelihood procedure yields density matrices and the fidelity can be used as a measure of the difference of two states.

3.2 Experimental setup

We will now discuss the experimental setup which has been used to perform all one qubit measurements, which are presented in this thesis. The sample consists of two transmon qubits [9], which are capacitively coupled to a microwave resonator. The transmon qubits are localized on each end of the resonator. The magnetic flux, which tunes the qubits is generated by two different coils. One of the coil has a inner diameter of 4 mm and couples in good approximation to only one qubit, where the other coil has a diameter of 16 mm and couples to both qubits. Adjusting the current of both coils gives the possibility to tune the flux through the two qubits individually. The qubits have coupling rates of $g_A = 133$ MHz and $g_B = 134$ MHz, $E_A^j = 35.112$ GHz and $E_B^j = 37.632$ GHz, $E_A^c = 331.7$ MHz and $E_B^c = 232.54$ MHz. The microwave resonator has on both ends a one plus two finger capacitor. The circuit is made of niobium on a sapphire substrate. The bare resonator has it's fundamental mode at 6.441 GHz and has a quality factor of roughly $Q = 4000$.

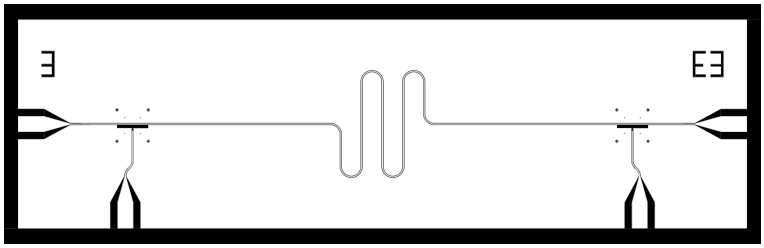

Figure 3.3: The picture shows the mask design, which was used to fabricated the resonator. The horizontal meandering line is the resonator, which is terminated on both ends by a one plus two finger contact. The signal is measured in transition. On each end of the resonator (middle of the 8 crosses) a transmon qubit is placed. Each transmos qubits is capacitively coupled to a separate charge gate line. These individual gate lines allow a individual manipulation of the qubits.

Operations on the qubits are done by using charge gate lines. A gate line is a wave guide, which is capacitively coupled to the reservoir of one of the qubits. The fact that the charge gate line is only coupled to one qubit gives the opportunity to manipulate the qubit individually. Each gate line is then connected to a microwave generator for driving the qubit. Between the generator and the gate line a mixer is implemented. The mixer modulates the amplitude and the phase of the microwave pulse.

It is important to make sure that no microwave field is exciting the qubit via the gate lines, if no drive pulse is applied. There are two possibilities to ensure that. The first is to turn off the microwave generator the second is to bring the mixer in the point where it fully blocks the drive field. Turning off the microwave generator sounds easier but it turns out that the mixer needs a continuous drive field to work properly. Therefore, we have to use the mixer to block the microwave field from exciting the qubit. However, the mixer is not linear and has an offset in I and Q. The problem of the mixers nonlinearity can be solved by calibrating the mixer as describes in the appendix 5.4. The offset can be removed by adding a constant voltage to the pulse sequences. However, to achieve a good on/off ratio the offset in I and Q has to be adjusted up to 100 μV. Unfortunately the used arbitrary waveform generator (AWG) has only a 1 mV voltage resolution. Therefore, additional voltage sources with smaller step size were connected in series with the AWG. To determine the offset the mixer's output has been measured by using a spectrum analyzer. The mixer's minimum can then be found by minimizing the output power as a function of the I/Q offset. However, if the spectrum analyzer is removed from the mixer a change in the potential at the mixer's output will occur and result in a shift of the offset. Therefore, the spectrum analyzer has been integrated into the setup as one can see in Fig. 3.4. For an input power of 14.5 dBm we can obtain a leakage of $P_{off} \leq -95$ dB. This is quite good especially if we compare it with the attenuation of $P_{I=300\text{ mV}} \leq -20$ dB which is at the usual operation point. This already shows that the mixer's on/off ratio ($\frac{P_{I=300\text{ mV}}}{P_{\text{off}}} \approx 75dB$) is good. To estimate the population of the excited level (for a closed mixer) we can use the simple formula

$$\frac{dP_e}{dt} = \Omega_{\text{leakage}} P_g - \Omega_{\text{leakage}} P_e - \frac{P_e}{T_1},$$

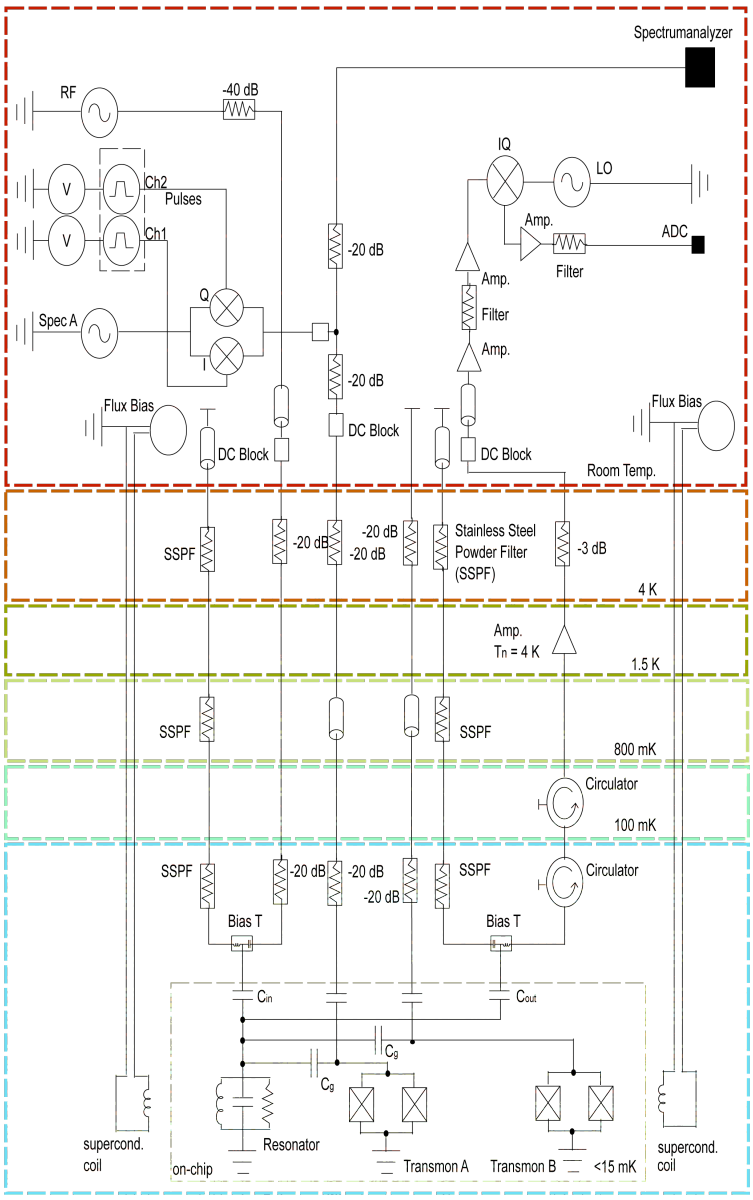

Figure 3.4: The graphic shows schematically the measurement and control circuitry. The signal generation for measurement and control pulses are pictured in the top left corner and the readout and calibration output are placed in the top right corner. The different temperature stages are indicated by color. The graphic shows all filters, attenuators and amplifiers. The two coils which have been used for individual detuning of the qubits are depicted on the side of the image.

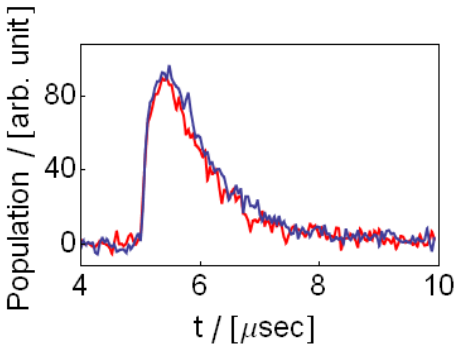

Figure 3.5: The graph shows the measured population of the excited state if a π pulse has been performed with backup pulse (blue) or continous driving of the mixer (red).

where P_e is the calculated population of the excited, P_g is the calculated population of the ground state, Ω_{leakage} is the Rabi frequency caused by the mixers leakage and T_1 is the qubit's decay rate. If we use the steady state condition $\frac{dP_e}{dt} = 0$, the normalization condition $P_g = 1 - P_e$ and if we assume that the Rabi frequency caused by the mixer's leakage is given by $\Omega_{\text{leakage}} = \Omega_{(I,Q)}\sqrt{\frac{P_{\text{leakage}}}{P_{(I,Q)}}}$, we can find a population of the excited state which is

$$P_e^{\text{leakage}} \leq 0.005.$$

To check if the population of the excited state is small we can measure the total phase shift of the response of a π pulse. The results for continuous measurement is plotted in Fig. 3.5. If the leaking of the mixer populates the excited state we will register a smaller phase shift after applying a π pulse. The ratio of the phase shifts for the operation pulse without backup pulse, which switch the microwave resonator on and off, and the operation with backup pulse is than given by

$$\frac{\phi_{\text{no backup}}}{\phi_{\text{backup}}} = 0.92 \pm 0.12.$$

This is in agreement with the calculated value. We can conclude it is possible to block the drive pulse by turning the mixer off without changing the power of the applied microwave.

3.3 Experimental approach

Here we explain how the measurements were performed. We will first show that dephasing processes can be neglected in good approximation for the performed experiments. Then we talk about the way the measurement pulses were applied and averaged. In the following we will explain how the measurement process was done. In addition we will explain how the calibration process for the tomography pulses was realized. And finally we will give an error estimate for systematic and statistical errors of the tomography. This section differs a lot from the experiment for two qubits, which will be discussed later.

Dephasing process

It would be convenient, if we could neglect all dephasing processes, which occur during the tomography process. Therefore, we analyze the influence of T_1 and T_2 on the tomography process. If we take interaction with the environment into account, the evolution of the qubit is not anymore described by the Von Neumann equation but by the master equation, which is a direct consequence of Markovian processes and the operator sum representation see appendix 5.5. The master equation is than given by

$$\frac{d\rho}{dt} = -\frac{i}{\hbar}\left[H,\rho\right] + \sum_{n\neq 0}\left(L_n\rho L_n^\dagger - \frac{1}{2}L_n^\dagger L_n\rho - \frac{1}{2}\rho L_n^\dagger L_n\right),$$

where the Markov approximation $M_n(t) = \sqrt{t}L_n$ has been used. This differential equation can easily be solved by changing into the Liouville space.

From measurements of T_1 and T_2, which were done independently, we know that qubit A has $T_1 \approx 380$ ns and $T_2 \approx 400$ ns and qubit B has $T_1 \approx 380$ ns and $T_2 =\approx 440$ ns. An upper limit for the error, which results from neglecting decoherence, can now been found by

$$\max_{|\vec{r}|=1}\left|\frac{\rho_{\text{Lindblad}} - \rho_{\text{v.Neumann}}}{\rho_{\text{v.Neumann}}}\right|.$$

For pulse length of $\tau = 20$ ns we can find an error that is 0.03, 0.029 respectively. This is of sufficient accuracy for our measurements.

Applied pulse sequences

The microwave pulses for controlling the qubit state are shaped by putting a continuous microwave field through a I/Q mixer, which modulates the amplitude and phase of the output field. The mixer does this modulation by applying a DC voltage to two different channels I/Q. For further detail see Section 3.2. The pulse sequences for the mixer I/Q port have been generated by using a arbitrary waveform generator (AWG) AWG5014 from Tektronix. The AWG has a 10 bit resolution for the amplitude of the output voltage and a 1 ns time resolution. The AWG loads the pattern files which determines the pulse sequences. The AWG then runs each pattern file once. After running all pattern files the AWG repeats the process several times and averages. One pattern file consists of a file for the I and one for the Q channel and a trigger file that turns on the microwave generator for the measurement if the measurement has been done pulsed. In addition there would be the possibility to implement an additional file that turns one the microwave generator which drives the qubit.

Measurement process

The measurement process was either done continuous, which means that the resonator has always been populated with photons (at the resonator frequency ω_{res}), or pulses, which means that the measurement photons are only in the resonator if we do a measurement. Continuous measurement has the enormous drawback that the measurement photons will

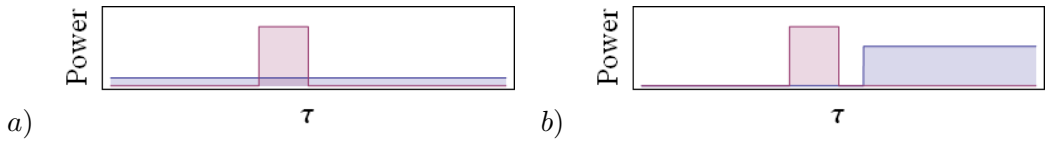

Figure 3.6: Schematic picture for the pulse sequences. The blue pulse is the measurement pulse and the red is the operation pulse. The left picture shows a continous measurement where the right one shows a pulsed measurement.

cause an AC Stark shift. This can be seen by writing the Jaynes Cummings Hamiltonian in the dispersive limit

$$H_{JC} \approx \hbar \left(\omega_r' + \chi\sigma_z\right)\left(a^\dagger a + \frac{1}{2}\right) + \hbar\frac{\omega_{01}}{2}\sigma_z$$

The AC Stark shift is represented by the term $\hbar\chi\sigma_z a^\dagger a$. Since the Hamiltonian depends on the photon number $a^\dagger a$ the eigenenergies will vary, if the photon number fluctuates. This fluctuations will cause a random phase shift which will yield decoherence [34]. Therefore, the photon number in the resonator and hence the measurement power has to be kept low. On the other hand the signal-to-noise ratio increases proportional to the measurement power and measurement time. This fact requires a large averaging if the measurement is performed at low power.

Even though that this is an enormous drawback for continuous measurement it has the clear advantage that we can observe the qubit before, while and right after applying the operation pulses. However, in most cases the operation pulses are much shorter than the cavity response and the resonator is only virtually populated by photons from the operation pulses. The two different pulse sequences for the cases of continuous measurement and pulsed measurement are shown in Fig. 3.6.

As discussed previously, the phase shift of the transmitted microwave is determined during the measurement process. Due to energy relaxation the phase signal will decay exponentially in time (on a scale of T_1).

On the other hand the expectation value for the population of the excited state $p_k = Tr\left(U_k^\dagger \left|1\right\rangle\left\langle 1\right| U_k\rho\right)$ is proportional to the measured phase $p_k \propto \phi(t=0)$ shift. This can easily be seen by the fact that the expectation value for the phase shift is given by

$$\phi_k = Tr\left(U_k^\dagger\phi_0 \left|1\right\rangle\left\langle 1\right| U_k\rho\right) = \phi_0 p_k,$$

where ϕ_0 is the phase shift for the transmon in the excited state $\phi_0 = \arctan\left(\frac{\omega_{meas}}{\omega_0+\chi}\right)$, χ is the effective dispersive phase shift, ω_{meas} is the measurement frequency and ω_0 is the resonator frequency.

It can be shown [29] that the optimal way to determine the quantity $p_k(t=0)$ is to calculate a weighted average over time. The optimal weighting factor $f(t) = p_{|1\rangle\langle 1|}\exp(-t/\lambda)$ is an exponential decay with decay rate equal to the qubit decay rate λ. The weighted average $\tilde{p}_k$ is given by

$$\tilde{p}_k = \frac{\sum_t f(t)p(t)}{\sum_t f^2(t)}.$$

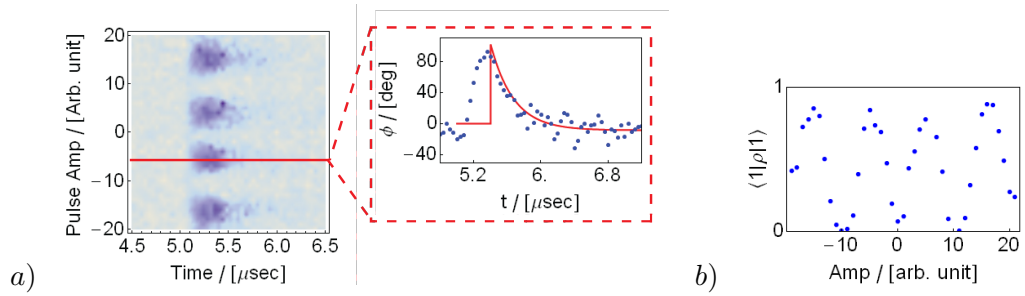

Figure 3.7: The graphic shows how the population of the exited is determined for different pulse sequence (here in a Rabi experiment). The left graphic shows the measured phase shift (blue coresponds to high phase shift) as a function of time after applying a pulse (x axis) and as a function of the pattern file number (y axis) here indicated by pulse amplitude. The middle picture shows the process for determining the initial population, which is calculated by building the scalar product of the experimental points (blue) and an exponential weighting factor (red) $\frac{\sum_t f(t)p(t)}{\sum_t f^2(t)}$. The last picture shows than the population of the excited state as a function of the pattern file number (here pulse amplitude).

A simple calculation shows that $\tilde{p}_k(0) = p_k(0)$.

$$\tilde{p}_k = \frac{\int_0^\infty p_k(t)f(t)}{\int_0^\infty f(t)^2} \overset{p_k(t)=p_k(0)\exp(-t/\tau)}{\longrightarrow} p_k(0).$$

This method gives us the opportunity to extract the population of the excited state after performing an operation on the qubit. This process is illustrated for the case of a Rabi process in Fig. 3.7.

Manual calibration of the tomography pulses

We would like to use tomography pulses which are close to id, $\left(\frac{\pi}{2}\right)_x$ and $\left(\frac{\pi}{2}\right)_y$. The easiest way to distinguish the amplitude for a $\left(\frac{\pi}{2}\right)$ pulse is by performing a Rabi oscillation. Since we are keeping the length of the tomography pulses constant we have to perform a Rabi experiment with varying pulse amplitude. The pulse amplitude, which yields a population of 50% of the excited state can be identified with the amplitude, which is required for a $\left(\frac{\pi}{2}\right)$ pulse (see Fig. 3.10). However, this determines only the quantity $\sqrt{\Omega_x^2 + \Omega_y^2}$ it does not state anything about the phase $\phi_i = \arg(\Omega_{x,i} + i\Omega_{y,i})$ of the tomography pulse. To ensure that the $\left(\frac{\pi}{2}\right)_x$ and $\left(\frac{\pi}{2}\right)_y$ pulses are close to be orthogonal we take the results from the mixer calibration, which is described in the appendix 5.4. The calibration data gives us the opportunity to determine a set of $(I, Q)_{1,2}$ values, which have the property of creating orthogonal pulses parametrized in the amplitude $|\Omega\tau|\,(\cos(\varphi), \sin(\varphi))$ and $|\Omega\tau|\,(-\sin(\varphi), \cos(\varphi))$, where the power has been parametrized be the quantity $|\Omega\tau|$. This procedure is pictured in Fig. 3.8.

Even though the tomography pulses have been calibrated we want to eliminate slight miss matches in the calibration. Therefore, we attach to the sequence file four additional pattern files which create $\left(\frac{\pi}{2}\right)_x$, $\left(\frac{\pi}{2}\right)_y$, $\left(\frac{\pi}{2}\right)_x \circ \left(\frac{\pi}{2}\right)_y$ and $\left(\frac{\pi}{2}\right)_y \circ \left(\frac{\pi}{2}\right)_x$ pulses. If now these four

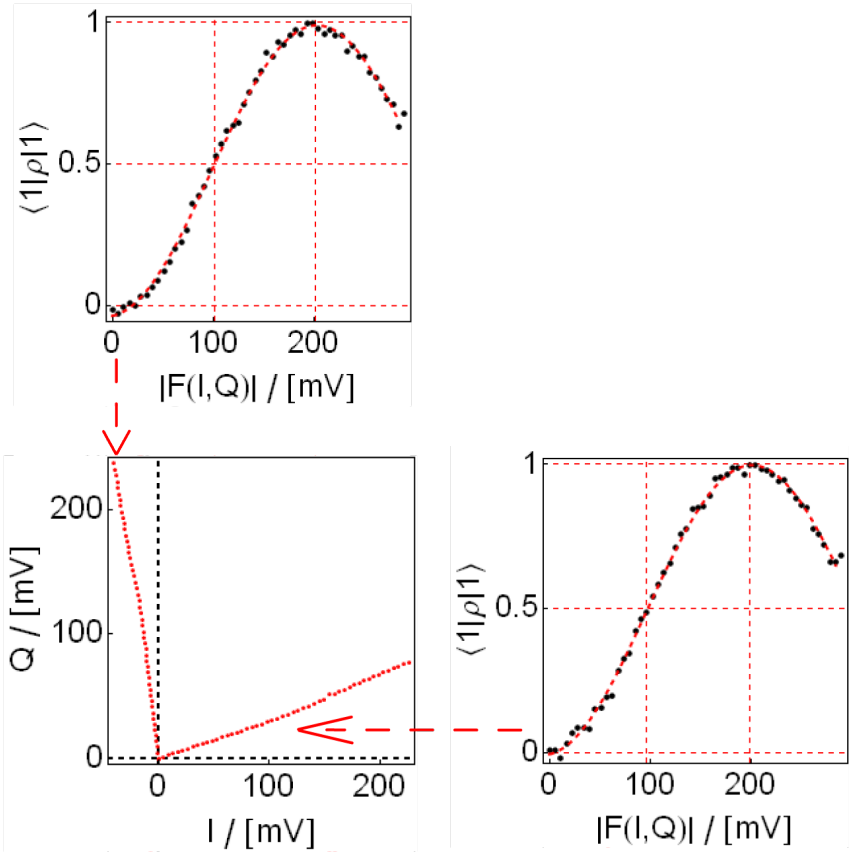

Figure 3.8: The graphics show the calibration procedure for finding $\left(\frac{\pi}{2}\right)$ and π pulses used for tomography. The plot in the lower left corner shows the voltage on the (I, Q) channel, which is required to create orthogonal microwave pulses with variable amplitude. The points were found by using a vector network analyzer. The population of the excited state for the two branches was measured as shown in the graphics to the right and to the top left side. The (I, Q) voltage for a tomography pulses is then determined by finding the (I, Q) values, which corresponds to a population of 0.5, 1 respectively (red dashed lines).

measurements have response 0.5 we can say with certainty that the tomography pulses have been calibrated in the right way. If not this measurement gives the opportunity to perform the auto calibration procedure, which is explained in the next Section 3.3.1.

3.3.1 Auto calibration for tomography pulses

The tomography procedure described above is a simple and elegant way to determine an arbitrary state. However, the approach discussed above requires that we know exactly what kind of operations U_k we have applied. What can be done if the operations U_k are unknown or have a systematic error? A method will now be introduced, which determines the tomography pulses in the same run as the tomography process is performed. For the further discussion we will call the process which determines the tomography pulses auto calibration.

The idea of the auto calibration is to include in the measurement run a pulse sequence, which determines the tomography pulses. The only requirement the pulses have to fulfill is the assumption that they yield a system of equations, which has kernel equal zero. Of course the accuracy can be increased if the tomography pulses have been chosen in a optimal way. A description on the best choice for tomography pulses can be found in [35]. As the discussion of the experiment shows it is especially easy to create an identity pulse. Therefore, we have to determine only two more pulses U_1 and U_2. If the system is not detuned the Hamiltonian for the two pulses have the form $H_k = \hbar\Omega'_{x,k}\sigma_x + \hbar\Omega'_{y,k}\sigma_y$, with $k = 1, 2$. Since a global phase is of no interest [1] the Hamiltonian can be written in the from $H_1 = \hbar\Omega_{x,1}\sigma_x$ and $H_2 = \hbar\Omega_{x,2}\sigma_x + \hbar\Omega_{y,2}\sigma_y$. The task is to determine the three amplitudes $\Omega_{x,1}$, $\Omega_{x,2}$ and $\Omega_{y,2}$. This requires three proper equations. If the initial state is chosen to be the ground state, the time evolution of the density matrix is given by $\rho(t) = \exp\left[-i\frac{H}{2\hbar}(t-t_0)\right]|0\rangle\langle 0|\exp\left[i\frac{H}{2\hbar}(t-t_0)\right]$. The required three equations can now to be obtained by measuring the pulse sequences U_1, U_2 and U_1U_2 as shown in Fig. 3.9. The resulting system of equations is than given by

$$p_1^{cal} = Tr\left(U_1^\dagger|1\rangle\langle 1|U_1|0\rangle\langle 0|\right)$$

$$p_2^{cal} = Tr\left(U_2^\dagger|1\rangle\langle 1|U_2|0\rangle\langle 0|\right)$$

$$p_3^{cal} = Tr\left(U_2^\dagger U_1^\dagger|1\rangle\langle 1|U_1U_2|0\rangle\langle 0|\right)$$

This system is nonlinear but can be solved numerically. For this purpose a function

$$S\left(\Omega_{x,1},\Omega_{x,2},\Omega_{y,2}\right) = \left(p_1 - Tr\left(U_1^\dagger|1\rangle\langle 1|U_1|0\rangle\langle 0|\right)\right)^2 +$$

$$+\left(p_2 - Tr\left(U_2^\dagger|1\rangle\langle 1|U_2|0\rangle\langle 0|\right)\right)^2 + \left(p_3 - Tr\left(U_2^\dagger U_1^\dagger|1\rangle\langle 1|U_1U_2|0\rangle\langle 0|\right)\right)^2$$

has been introduced. Since U_k are periodic functions in $\Omega_{x,1}$, $\Omega_{x,2}$ and $\Omega_{y,2}$ the additional constraint $|\Omega_{x,1}| < 2\pi$ and $\sqrt{\Omega_{x,2}^2 + \Omega_{y,2}} < 2\pi$ has to be satisfied. The function S in respect to the given constraints can be minimized by using the option FindMinimum, which is implemented in Mathematica6.0. The problem of finding local minima instead of global can be avoided by choosing the starting point randomly.

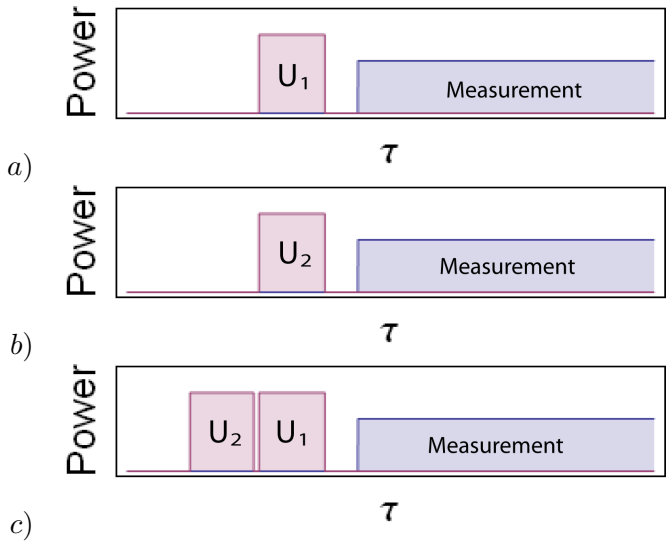

Figure 3.9: Systematic scheme of the calibration procedure. The purple line indicates the pluses U_1 and U_2. The two pulses U_1 and U_2 are different in phase (not indicated) and different in amplitude, but have the same length of 20 ns. The blue pulse indicates, when the RF field for the measurement is turned on and the cavity gets populated with photons for measurement.

Error estimation

We can basically make out two different sources for measurement error. The first possibility is that the $\left(\frac{\pi}{2}\right)$ and π pulses are not properly calibrated. The second source is statistical noise in the measurement process. Both of them will yield an error in the density matrix. We will first discuss the error coming from inaccuracy in the tomography pulse and in the next section we will talk about the influence of statistical noise.

Systematical error for tomography pulse:

Even though we found a way to correct errors in the tomography pulses it is more convenient to assume that the tomography pulses are perfect $\left(\frac{\pi}{2}\right)$ pulses. Therefore we will now discuss how close this the tomography pulses are to perfect $\left(\frac{\pi}{2}\right)$ pulses.

If we write the tomography pulses in the generalized way

$$U\left(\Omega_x, \Omega_y\right) = \exp\left(-i\frac{\Omega_x \tau \sigma_x + \Omega_y \tau \sigma_y}{2}\right),$$

it becomes clear that the error in the $\left(\frac{\pi}{2}\right)$ pulses comes from an error in $\Omega_i \tau$. The expectation value for the qubit in the excited state is then given by the A matrix

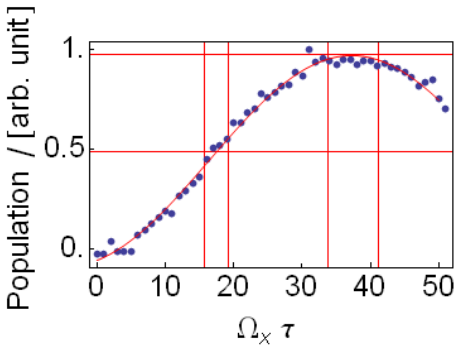

Figure 3.10: The picture shows the population of the excited state as a function of the pulse amplitude. This allows us to determine the power, which is required to create a $\frac{\pi}{2}$ and π pulse.

$$A = \begin{pmatrix} \frac{\Omega_{y,1} sin\tau\sqrt{\Omega_{x,1}^2+\Omega_{y,1}^2}}{\sqrt{\Omega_{x,1}^2+\Omega_{y,1}^2}} & \frac{-\Omega_{x,1}\sin\tau\sqrt{\Omega_{x,1}^2+\Omega_{y,1}^2}}{\sqrt{\Omega_{x,1}^2+\Omega_{y,1}^2}} & -\cos\tau\sqrt{\Omega_{x,1}^2+\Omega_{y,1}^2} \\ \frac{\Omega_{y,2}\sin\tau\sqrt{\Omega_{x,2}^2+\Omega_{y,2}^2}}{\sqrt{\Omega_{x,2}^2+\Omega_{y,2}^2}} & \frac{-\Omega_{x,2}\sin\tau\sqrt{\Omega_{x,2}^2+\Omega_{y,2}^2}}{\sqrt{\Omega_{x,2}^2+\Omega_{y,2}^2}} & -\cos\tau\sqrt{\Omega_{x,2}^2+\Omega_{y,2}^2} \\ \frac{\Omega_{y,3}\sin\tau\sqrt{\Omega_{x,3}^2+\Omega_{y,3}^2}}{\sqrt{\Omega_{x,3}^2+\Omega_{y,3}^2}} & \frac{-\Omega_{x,3}\sin\tau\sqrt{\Omega_{x,3}^2+\Omega_{y,3}^2}}{\sqrt{\Omega_{x,3}^2+\Omega_{y,3}^2}} & -\cos\tau\sqrt{\Omega_{x,3}^2+\Omega_{y,3}^2} \end{pmatrix}$$

The error can than be estimated by

$$\Delta r_k = \sum_{l=0}^{3} p_l \sqrt{\left(\frac{\partial (A_{k,l})^{-1}}{\partial \Omega_{x,l}}\right)^2 \Delta\Omega_{x,l}^2 + \left(\frac{\partial A_{k,l}}{\partial \Omega_{y,l}}\right)^2 \Delta\Omega_{y,l}^2}$$

Mathematica can calculate this strait forward calculations easily.

As shown in Fig. 3.10 the $\left(\frac{\pi}{2}\right)$ and π pulses are determined by performing a Rabi pulse. The accuracy for the $\left(\frac{\pi}{2}\right)$ and π pulses are about $\frac{\Delta\Omega_i\tau}{\Omega_i\tau} = 0.1$. This error in $\Omega_i\tau$ will then yield an inaccuracy in determining the Bloch vector $\frac{\Delta r_k}{r_k} \leq 0.05$.

Statistical error in tomography:

Since we are measuring only for a finite time interval the measured value for p_k has a certain statistical error. If we assume that the measurement is Gaussian distributed the standard deviation $stdw_k \propto \sqrt{n}$. In principle this gives the possibility to do an error estimation. The error in the Bloch vector is then given by $\Delta\vec{r} = A\vec{\sigma}$, with $\vec{\sigma} = (\sigma_x, \sigma_y, \sigma_z)$. For the measurement we can find for each measurement point a standard deviation of $\sigma \approx 3.3^o$. However, the population of the excited state is calculated by using a weighted average $\tilde{p}_k = \sum_t \frac{f(t)\phi(t)}{f^2(t)}$, where the weighting function is given by $f(t) = \exp(-t/\lambda)$. This yield a standard deviation for p_k of $p_k \approx 0.015$. Again this measurements were taken with approximately 1 photon in the resonator and 655350 times averaged. The error for the Bloch vector can be estimated as $\frac{\Delta r_{x,z}}{r_{x,z}} \approx 0.03$. Even though, that this error seems to

be of the same order as the systematical it is rather easy to reduce it by increasing the measurement time or even better by increasing the measurement power by performing pulsed measurements. The adventage of increasing the power is given by the fact that the statistical accuracy is proportional to the measurement photon numbers but only to the square root of the measurement time. However, if we would have done the measurement in pulsed mode the error would have been smaller by an order of magnitude.

3.4 Experimental results

In this section we will discuss the results of the experiments performed on one qubit. First we will talk about a two dimensional tomography procedure, which was applied on the four different states $|0\rangle$, $|1\rangle$, $|0\rangle + |1\rangle$ and $|0\rangle + i\,|1\rangle$. This has the motivation to show that the system responds in an expected way. Next we will do state tomography, using three pulses, on the same four states as above. For all the other experiments we will use three tomography pulses. After that we will go on with tomography of a Rabi and Ramsey experiment. This has the purpose to illustrate that the tomography procedure works. In the end we will also perform a process tomography on a Hadamard gate.

3.4.1 Two dimensional Plots

As we have seen for the one qubit case a full tomography can be performed by using the manipulation $H = \hbar\Omega_x\sigma_x + \hbar\Omega_y\sigma_y$. Therefore, it is important to verify that applying this operations will yield the predicted states. Since this Hamiltonian is just depending on Ω_x and Ω_y, which is given by the power and the phase of the drive pulse, it is enough to check the responses as a function of Ω_x and Ω_y. For this reason we measure the population of the excited state as a function of $\tau\Omega_x$ and $\tau\Omega_y$. As starting states we use $|0\rangle$, $|1\rangle$, $|0\rangle + |1\rangle$ and $|0\rangle + i\,|1\rangle$.

For this experiment a microwave generator with integrated I/Q mixer has been used. This microwave generator has the enormous advantage that the I/Q mixer can automatically be calibrated in phase and amplitude.

Results:

The measurement response for such a pulse sequence can be calculated by

$$p\left(\Omega_x, \Omega_y\right) = Tr\left(\exp\left[-i\frac{(\Omega_x\sigma_x + \Omega_y)\tau}{2}\right]\rho\exp\left[i\frac{(\Omega_x\sigma_x + \Omega_y)\tau}{2}\right]\frac{1-\sigma_z}{2}\right).$$

The formula given above yields for the starting value $|0\rangle$, $|1\rangle$, $|0\rangle + |1\rangle$ and $|0\rangle + i\,|1\rangle$ to the expectation values which are plotted in Fig. 3.11. The response for the qubit starting in the ground and excited state is rotation symmetric. It can be proven by a simple straight forward calculation that the expectation value $p = Tr\left(U^\dagger\frac{1-\sigma_z}{2}U\rho\right)$ is rotational symmetric if and only if the density matrix takes the values $\rho = (1 \pm \sigma_z)/2$.

If we assume that the preparation pulse has not been perfect we can obtain a response similar to the one given in Fig. 3.12. For the case that the qubit is driven at a detuned frequency $\Delta = \omega_{01} - \omega_{\text{drive}}$ the measured response will yield a response as give in Fig. 3.12.

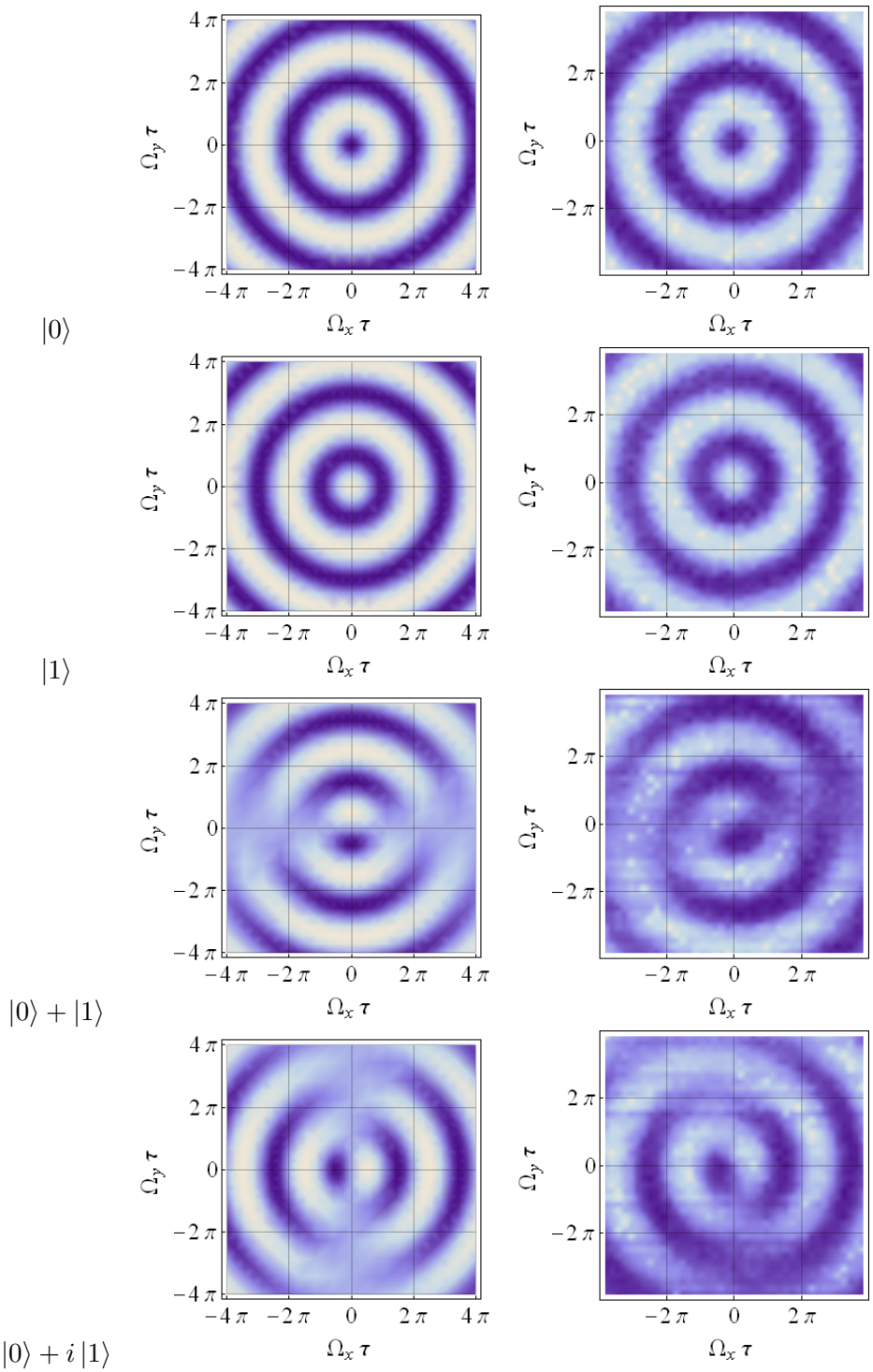

Figure 3.11: The graphics show the population of the excited state $\langle 1|\,\rho\,|1\rangle$ (blue population zero, white population one). The prepared states from top to bottom are $|0\rangle$, $|1\rangle$, $|0\rangle + |1\rangle$ and $|0\rangle + i\,|1\rangle$. The left hand side is a simulation and the right hand side is the measurement.

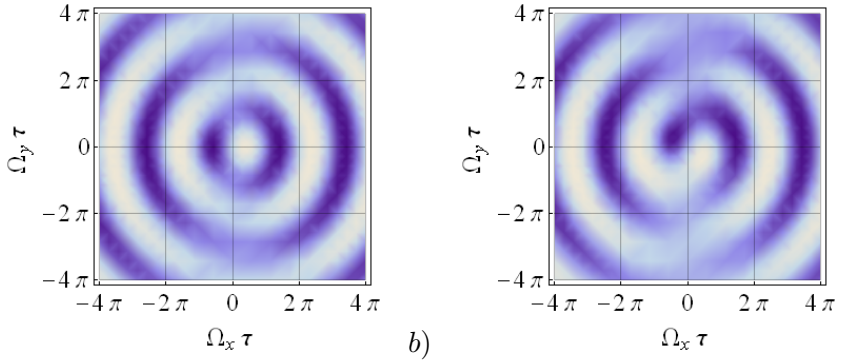

Figure 3.12: The plots show simulations for imperfect preparation and tomography pulses. The left plot shows tomography on a state with $a\,|0\rangle + b\,|1\rangle$ where $|a| < |b|$ and the right plot shows the response for detuned tomography pulses.

If we compare the simulation to the experiment it can be recognized that the drive frequency is slightly detuned form the qubit's transition frequency. However, this is not surprising since the measurement run took more than 7 hours.

Applied pulse sequences:

In the case of the microwave generator with integrated I/Q mixer, the mixer can be calibrated automatically and the output of the microwave generator will have amplitude $\propto \sqrt{I^2 + Q^2}$ and phase $= \arg(I + iQ)$. The I/Q channel of the integrated mixer can be controlled by an external source which is in our case a AWG generator. Since a measurement with all pattern files in one sequence file would consume to much memory of the acquisition card shorter sequences of pattern files have been loaded in a row.

For the experiment the measurement have been done with a continuous measurement field. The power of the RF generator has been set to a value equivalent to one photon in the resonator. The measurement have been averaged 655350 times. The transition frequency for the qubit has been at 5 GHz, which corresponds to $\omega_r - \omega_{01} = 1.5$ GHz. The pulse lemgth was chosen to to 20 ns.

3.4.2 State tomography

Even though that the two dimensional plots, which are described above, fully determine the initial density matrix, the measurement is not practical for application because it takes too long to record it. However, as shown in the theory Section 3.1.2, it is sufficient to apply three appropriate tomography pulses to reconstruct the qubit's initial state.

To keep the pulse calibration simple we have chosen the id, $\left(\frac{\pi}{2}\right)_x$ and $\left(\frac{\pi}{2}\right)_y$ tomography pulses, see Fig. 3.14.

Results:

Tomography was done on the four different states $|0\rangle$, $|1\rangle$, $|0\rangle + |1\rangle$ and $|0\rangle + i\,|1\rangle$. We assume perfect tomography pulse (the case of imperfect pulses will be discuss later). This assumption is justified by reconstructing the driving pulses from the measurement $p_1 = |U_1 \rho U_1^\dagger\,|1\rangle\,\langle 1|\,|$, $p_2 = |U_2 \rho U_2^\dagger\,|1\rangle\,\langle 1|\,|$ and $p_{1,2} = |U_2 U_1 \rho U_1^\dagger U_2^\dagger\,|1\rangle\,\langle 1|\,|$ which yield operations given by

$$U_1 = \begin{pmatrix} 0.73 & -0.69i \\ -0.69i & 0.73 \end{pmatrix} \text{ and } U_2 = \begin{pmatrix} 0.69 & -0.72 + 0.02i \\ 0.72 + 0.02i & 0.69 \end{pmatrix}.$$

$$U_1^{perfect} = \frac{1}{\sqrt{2}} \begin{pmatrix} 1 & -i \\ -i & 1 \end{pmatrix} \text{ and } U_2^{perfect} = \frac{1}{\sqrt{2}} \begin{pmatrix} 1 & -1 \\ 1 & 1 \end{pmatrix}.$$

This is very close to what would be expected from orthogonal $\left(\frac{\pi}{2}\right)$ pulses. Therefore we assume perfect $\left(\frac{\pi}{2}\right)$ pulses.

The density matrices can be reconstructed by using the property

$$\vec{r} = \frac{1}{2} \begin{pmatrix} \frac{1}{2} & 0 & 0 \\ 0 & -\frac{1}{2} & 0 \\ 0 & 0 & -\frac{1}{2} \end{pmatrix} \vec{p} - \frac{\vec{e}_1 + \vec{e}_2 + \vec{e}_3}{2}.$$

The density matrices for these experiments are plotted in Fig. 3.13.

Since the density matrices have been determined by solving the linear system of equations the found matrices are not positive definite and calculating the fidelity would be useless. However the L_1 norm between the theoretical and the measurement states can be calculated and are found to be

$$D\left(\frac{1+\sigma_z}{2}, \rho_{id}\right) = 0.03,$$

$$D\left(\frac{1+\sigma_x}{2}, \rho_{(\pi/2)_x}\right) = 0.13,$$

$$D\left(\frac{1+\sigma_y}{2}, \rho_{(\pi/2)_y}\right) = 0.05 \text{ and}$$

$$D\left(\frac{1-\sigma_z}{2}, \rho_{\pi_x}\right) = 0.09.$$

For this case the L_1 norm has the very intuitive meaning of being the Euclidean of the points in the Bloch picture. These L_1 norms are indicating the the states are quite close together.

In the example above we have calibrated the tomography pulses well. It is interesting to show that the tomography procedure also works with imperfectly calibrated tomography pulses. However in that case an auto calibration procedure is required. For that reason we performed another experiment, with less carefully calibrated tomography pulses. This can be useful if it is not possible to calibrate th pulses perfectly.

If the tomography pulses are not perfect $\left(\frac{\pi}{2}\right)$, we can take a systematic error of the tomography pulses into account, if we use the auto calibration procedure, which has been

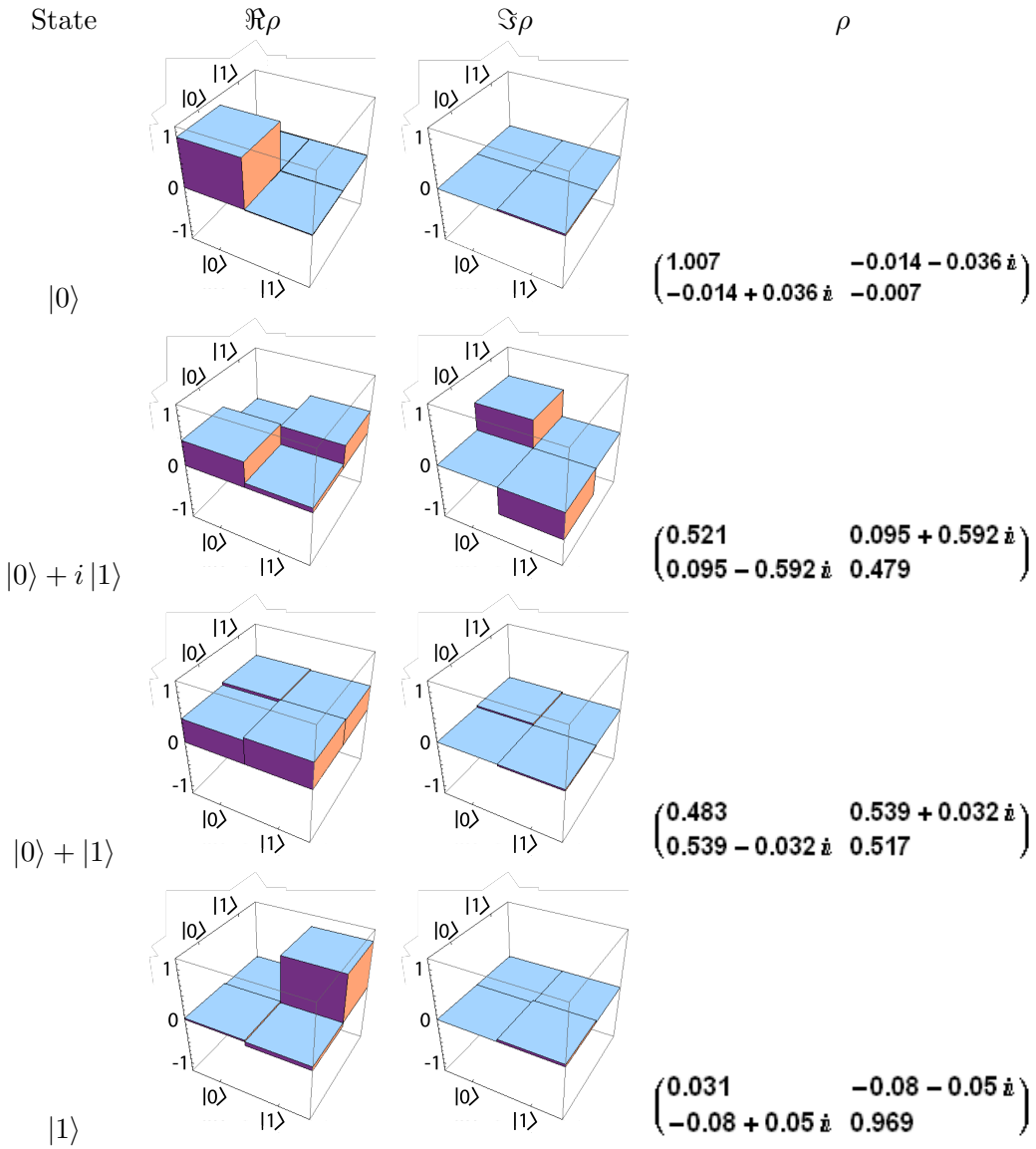

Figure 3.13: The plots show the real part (first row) and the imaginary part (second row) of the density matrices, which were found by tomography.

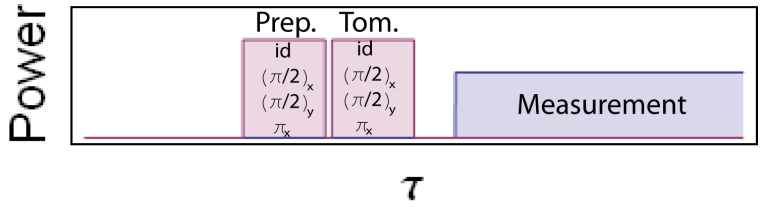

Figure 3.14: The picture shows the pulse sequence for the tomography process. The first purple pulse is for preparing the initial state ($|0\rangle$, $|1\rangle$, $|0\rangle + |1\rangle$ and $|0\rangle + i\,|1\rangle$). The second purple pulse for the tomography. The following pulse is for measuring (pulsed measurement). For the case of continuous measurement the photons populate the resonator all the time.

explained above. The density matrices for this states can then be reconstructed by using the previously derived formula

$$\vec{r} = \frac{1}{2}\begin{pmatrix} \frac{\Omega_{y,1}\sin\sqrt{\Omega_{x,1}^2+\Omega_{y,1}^2}}{\sqrt{\Omega_{x,1}^2+\Omega_{y,1}^2}} & \frac{-\Omega_{x,1}\sin\sqrt{\Omega_{x,1}^2+\Omega_{y,1}^2}}{\sqrt{\Omega_{x,1}^2+\Omega_{y,1}^2}} & -\cos\sqrt{\Omega_{x,1}^2+\Omega_{y,1}^2} \\ \frac{\Omega_{y,2}\sin\sqrt{\Omega_{x,2}^2+\Omega_{y,2}^2}}{\sqrt{\Omega_{x,2}^2+\Omega_{y,2}^2}} & \frac{-\Omega_{x,2}\sin\sqrt{\Omega_{x,2}^2+\Omega_{y,2}^2}}{\sqrt{\Omega_{x,2}^2+\Omega_{y,2}^2}} & -\cos\sqrt{\Omega_{x,2}^2+\Omega_{y,2}^2} \\ 0 & 0 & -1 \end{pmatrix}^{-1} \vec{p} - \frac{\vec{e}_1+\vec{e}_2+\vec{e}_3}{2}.$$

The results for this can be found in Fig. 3.15.

If we do an auto calibration procedure we can reconstruct the density matrices without loosing any accuracy. In addition we can compare the initial state with the measured state by calculating the L_1 norm. We find

$$D\left(\frac{1+\sigma_z}{2}, \rho_{id}\right) = 0.015,$$

$$D\left(\frac{1+\sigma_x}{2}, \rho_{(\pi/2)_x}\right) = 0.11,$$

$$D\left(\frac{1+\sigma_y}{2}, \rho_{(\pi/2)_y}\right) = 0.11 \text{ and}$$

$$D\left(\frac{1-\sigma_z}{2}, \rho_{\pi_x}\right) = 0.15.$$

This is of the same order as we found for well calibrated pulses. However it can be still important to apply a proper calibration, if we want to use $\left(\frac{\pi}{2}\right)$ for the experiment (e.g. in a Ramsey experiment or Hadamard gate).

In both experiments (with well calibrated and imperfect calibrated tomography pulses) I used for the state preparation the same pulses as for the tomography. To create a one qubit system the second qubit has been detuned to $\Phi = 0.5\Phi_0$ flux quantum. The other qubit, which was used for tomography, was kept at $\omega_{01} = 4.955$ GHz, which is equal to $\omega_r - \omega 01 = 1.5$ GHz. In the first example the measurement was done pulsed with 8 photons

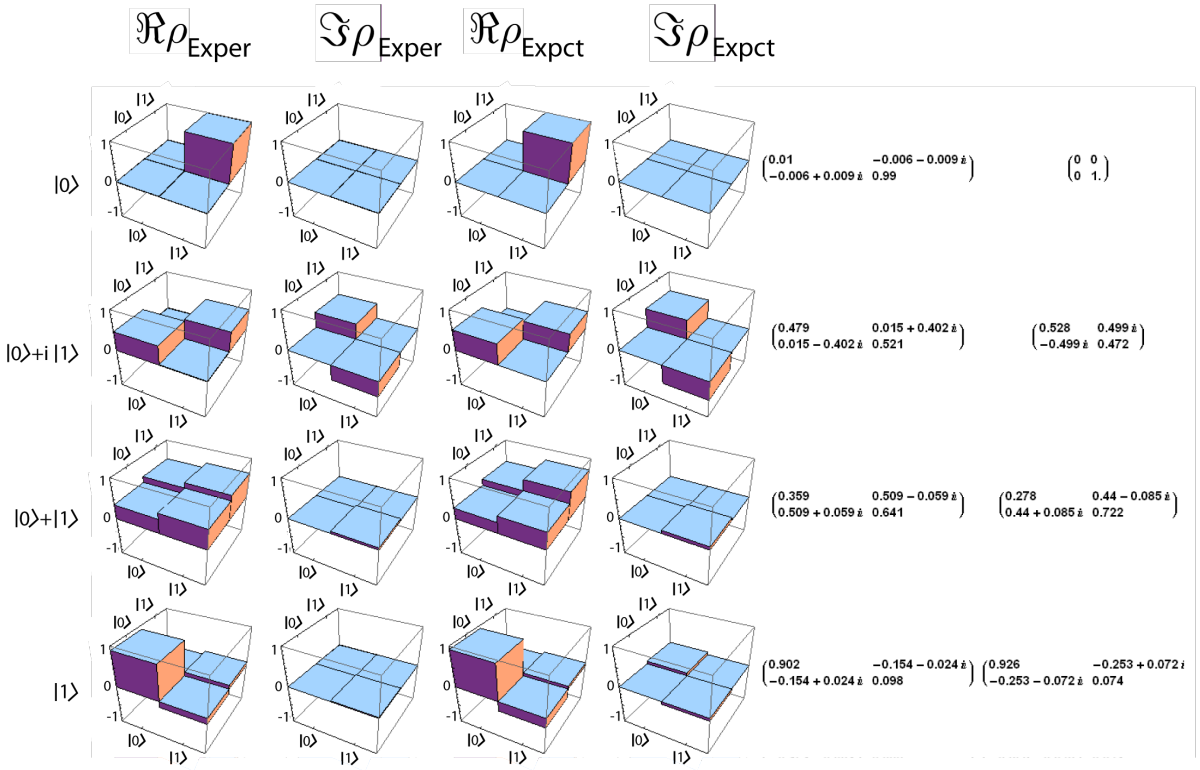

Figure 3.15: The first row shows the real part of the measured density matrices, the second row shows the imaginary part of the measured density matrices, the third row represents the real part of the density matrices expected from the auto calibration procedure, the fourth row pictures the imaginary part of the expected density matrices and the last two rows give the corresponding matrices.

in the resonator and 3 10^6 times averaged. In the second example the measurement was performed continuously, with one photon in the resonator and 6 10^5 times averaged.

Applied pulse sequence:

For the sequence file we need a part which can be used for the auto calibration and one for the tomography. The tomography process on the other hand consists of a preparation pulse and three tomography pulses. It can be seen that the sequence files consists of a fourth tomography pulse. However, this pulse has not been used for this analysis. For preparing the states id, $\left(\frac{\pi}{2}\right)_x$, $\left(\frac{\pi}{2}\right)_y$ and π we use pulses similar to the tomography pulses. A schematic picture of the pulse sequence is shown in Fig. 3.13.

3.4.3 State tomography of Rabi oscillations

Now we would like to apply tomography on a Rabi oscillation process. A Rabi rotation is one of the most simple process we can think of. As discussed above, the Hamiltonian for interaction is given by

$$H_{Rabi} = \frac{\hbar\Omega_x^{Rabi}}{2}\sigma_x + \frac{\hbar\Omega_y^{Rabi}}{2}\sigma_y,$$

where the detuning has been chosen to be zero and $\Omega_i = \frac{g}{\Delta}\epsilon_i(t)$ as previously. The time evolution of the density matrix starting from the ground state is then given by

$$\rho = \exp\left(-i\frac{H_{Rabi}}{\hbar}t\right)|0\rangle\langle 0|\exp\left(i\frac{H_{Rabi}}{\hbar}t\right)$$

$$\rho = \begin{pmatrix} \cos^2\left(\frac{1}{2}\sqrt{\Omega_x^2+\Omega_y^2}t\right) & \frac{(i\Omega_x+\Omega_y)\sin\left(\sqrt{\Omega_x^2+\Omega_y^2}t\right)}{2\sqrt{\Omega_x^2+\Omega_y^2}t} \\ \frac{(-i\Omega_x+\Omega_y)\sin\left(\sqrt{\Omega_x^2+\Omega_y^2}t\right)}{2\sqrt{\Omega_x^2+\Omega_y^2}t} & \sin^2\left(\frac{1}{2}\sqrt{\Omega_x^2+\Omega_y^2}t\right) \end{pmatrix},$$

where t indicates the pulse length and $\Omega = \sqrt{\Omega_x^2+\Omega_y^2}$ the pulse amplitude. It can easily be seen that this density matrix corresponds to a Bloch vector given by

$$\left(\frac{\Omega_y \sin\left(\sqrt{\Omega_x^2+\Omega_y^2}t\right)}{\sqrt{\Omega_x^2+\Omega_y^2}}, -\frac{\Omega_x \sin\left(\sqrt{\Omega_x^2+\Omega_y^2}t\right)}{\sqrt{\Omega_x^2+\Omega_y^2}}, \cos\left(\sqrt{\Omega_x^2+\Omega_y^2}t\right)\right)^T.$$

In the Bloch picture this is a rotation around the axis $(\Omega_x, \Omega_y, 0)^T$ with frequency $\omega_{Rabi} = \sqrt{\Omega_x^2+\Omega_y^2}$.

Results:

To measure this Rabi oscillation we can perform Rabi pulses of different length and reconstruct the state after the Rabi pulses by applying tomography. This yields the result given in Fig. 3.16. The measured Bloch vectors should lie on a circle. Indeed the

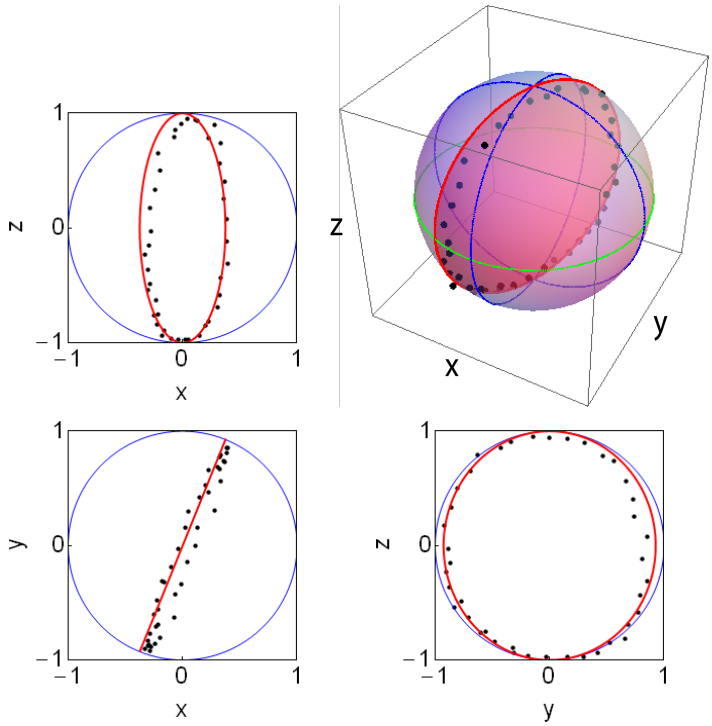

Figure 3.16: The plot illustrates a Rabi experiment. Each of the points corresponds to the qubit state after applying a pulse of different pulse length. The plot in the upper right corner shows the points on the Bloch sphere for Rabi oscillations. The two other plots indicate the projection on the xy-, xz- and yz- axis.

measurements are close to the predicted circle (red). One can see that the Rabi circle is neither lieing in the xz or yz plane. However, that is not an error in fact there is no reason why that should be the case, it just happens because the Rabi pulse have been chosen as $\arg(\Omega_x + i\Omega_y) = -21^o$. On the other hand we can see that the Rabi circle goes through the ground state as expected.

We can already see the Rabi experiment is close to the theoretical trajectory. However, it would be nice to check more carefully how well our Rabi experiment has been performed. Therefore we calculate the L_1 norm for each point in comparison to the theory. As we have seen the L_1 norm is defined by

$$D_{L1}(\rho_{\text{exper}}, \rho_{\text{theory}}) = \frac{1}{2} Tr\left(\left|\rho_{\text{exper}} - \rho_{\text{theory}}\right|\right)$$

Parameterizing the density matrix by the Bloch vector and using the normalization condition $Tr(\rho) = 1$ yields

$$D_{L1}(\rho, \delta) = \frac{|\vec{r}_{\rho\text{exper}} - \vec{r}_{\rho_{\text{theory}}}|}{2},$$

where $r_{\rho,i}$ is the i^{th} component of the Bloch vector for the density matrix ρ. This enables us to determine the error for performing and analyzing a Rabi pulse. If we assume that the Rabi pulse was created by a pulse with $Arg(\Omega_x + i\Omega_y) = -21^o$, we can calculate the L_1 norm $D_{L1}(\rho_{\text{theory}}, \rho_{\text{experiment}})$. This yields in average a norm of

$$D_{L1}(\rho_{\text{theory}}, \rho_{\text{experiment}}) = 0.08 \pm 0.04$$

which is comparable with the error estimated in the discussion on tomography of $\left(\frac{\pi}{2}\right)$ pulses.

Applied pulse sequences:

The data have been measured continuously, with a RF power equivalent to one photon in the resonator. The qubit's transition frequency was at $\omega_{01} = 4.9$ GHz a detuning of $\omega_r - \omega_{01} = 1.5$ GHz. In the measurement each pattern file has been averaged 655350 times. The sequence file consists of pattern files with different Rabi pulse length. For each Rabi pulse length three different tomography pulse have been used.

3.4.4 State tomography of Ramsey fringes

A more advanced example for time resolved experiments than the Rabi oscillations is a Ramsey fringe experiment. In a Ramsey experiment we want to prepare a equally superposition state and then accumulate phase by a σ_z rotation. For this an off resonant $\left(\frac{\pi}{2}\right)$ pulse brings the qubit from its ground state into a equally weighted superposition state. Since the operation pulse has been off resonant the term $\Delta = \left(\chi(a^\dagger a + \frac{1}{2}) + \frac{\omega_{01}}{2} - \frac{\omega_{\text{drive}}}{2}\right)\sigma_z$, in the rotating wave approximation, is not equal to zero. The Hamiltonian becomes

$$H = \frac{\hbar\Delta}{2}\sigma_z + \frac{\hbar\Omega_x}{2}\sigma_x + \frac{\hbar\Omega_y}{2}\sigma_y.$$

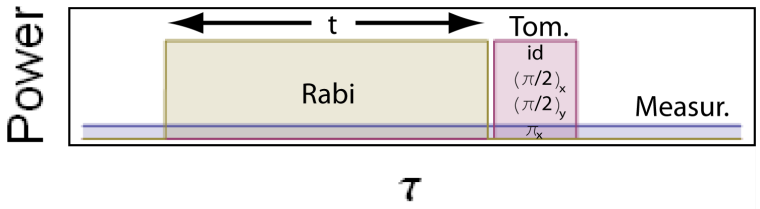

Figure 3.17: This graphic shows the pulse scheme for tomography on a Rabi oscillation. The purple pulse shows the tomography pulse, the brown pulse indicated the Rabi pulses (the rotation angle is regulated by adjusting the length of the Rabi pulse) and the blue indicates the measurement.

Therefore, a σ_z rotation will remain. If we now prepare such as superposed state and measure it with a delay, we will register a state that has been rotated by $t\Delta$, with t the time between the off resonant $\left(\frac{\pi}{2}\right)$ pulse and the measurement. Since the experiment has been performed on a long timescale we have to include decoherence T_1 and T_2. A common way to solve this problem can be done by introducing the Lindblad operator and using super operators, see Section 2.8. However, we will use here a different approach. Since we depict the system as Bloch vector we will use the phenomenological Bloch equations [36] to describe time evolution of the qubit. In the rotating frame the Bloch equation for a non driven qubit is then given by

$$\frac{dr_x}{dt} = -\frac{r_x}{T_2} + \Delta \cdot r_y$$

$$\frac{dr_y}{dt} = -\Delta \cdot r_x - \frac{r_y}{T_2}$$

$$\frac{dr_z}{dt} = \frac{1 - r_z}{T_1}.$$

In this case the last equation is already decoupled from the other two. It can immediately be seen that the Bloch vector performs a rotation around the z axis with a frequency equal to the detuning. The $-\frac{1}{T_2}$ term represents phase decoherence and causes a contraction of the r_x and r_y component. The time evolution of the r_z component is determined by relaxation of the qubit into the ground state and decays with a decoherence time T_1.

Results:

As mentioned above we can perform a Ramsey experiment by applying a $\left(\frac{\pi}{2}\right)$ pulse on the ground state and do a tomography after waiting a variable time. This yields the results given in Fig. 3.18. One can see the predicted rotation around the z axis as well as the effects coming from T_1 and T_2. To determine how accurate the Ramsey experiment in combination with the tomography fit to the experiment we can again determine the L_1 norm. For the case where we fitted $\Delta = 40$MHz, $T_1 = 800$ ns and $T_2 = 420$ ns the norm becomes $D_{L1}(\rho_{\text{theory}}, \rho_{\text{experiment}}) = 0.07 \pm 0.04$. This is again in good agreement with the error form the discussion above.

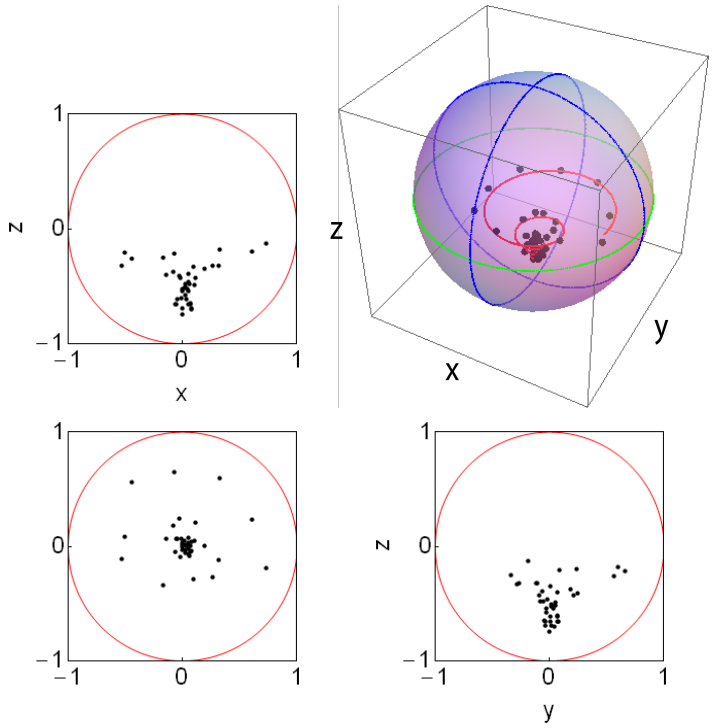

Figure 3.18: The graphic shows tomography on a Ramsey experiment. The right upper picture illustrates the points on the Bloch sphere for different time between the preparation $\left(\frac{\pi}{2}\right)$ and the tomography pulses. The other three plots show projection of the Bloch sphere on the xy-, xz- and yz- axis. One can see how the Bloch vector turns around the z axis and contracts due to T_2. In addition one can recognize energy relaxation corresponding to T_1.

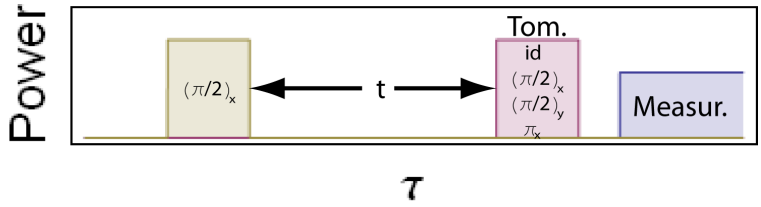

Figure 3.19: The schematic picture shows the pulse which were applied for a Ramsey experiment. The brown pulse is a off resonant $\left(\frac{\pi}{2}\right)$ pulse. The time t between the preparation pulse an the tomography is varied. The purple pulse indicates the tomography pulses.

It should be mentioned that for the initial $\left(\frac{\pi}{2}\right)$ pulse the drive frequency has to be detuned from the qubit frequency, because we want to obtain σ_z rotations. On the other hand the tomography pulses should be on resonance to prevent additional rotations while doing the tomography. However, the tomography pulses and the preparation pulse are created with the same microwave generator. Therefore we can only perform slow σ_z rotations. A possibility to apply a preparation pulse and tomography pulses at different frequency is by using two generators and bringing the signal together by a combiner.

Applied pulse sequences:

The measurement have been performed continuously with a power equivalent to one photon in the resonator. The data have than been averaged 600000 times. The sequence file consists of pattern files which have different time length between the preparation $\left(\frac{\pi}{2}\right)$ pulse and the tomography pulse. A schematic plot of the sequence file can be seen in Fig. 3.19.

3.4.5 Process tomography

Now that we are able to perform state tomography with good accuracy we can think of implementing process tomography.

Process tomography is a very useful tool, because it enables us to characterize operations performed on the qubit. This is of importance if we would like to characterize coherent operations, as for example in logical gates. Furthermore it gives us the opportunity to analyze incoherent operations like decoherence processes (T_1 and T_2) [6], which are important if we deal with open systems. Hence process tomography makes it possible to measure the Lindblad operators [6]. In addition a most likelihood procedure can be implemented [37].

The goal of process tomography is to determine an arbitrary linear function E, which maps a initial state of the qubit ρ^{in} on a final state $\rho^{out} = E(\rho_{in})$. The linear function E has to preserve hermiticity, trace and positivity, if we apply E on an arbitrary density matrix. This has to be satisfied since we are interested in a physical quantum map.

We know from theory (see appendix 5.5) that any quantum map (even those which describe interactions with the environment) can be written by the operator sum representation. With N^2 operators, where N is the systems dimension, we can write the map

by

$$E(\rho) = \sum_{n \leq N^2} M_n \rho M_n^\dagger,$$

where $\{M_n\}$ is a set of operators, which fulfill the completeness relation

$$1 = \sum_{n \leq N^2} M_n^\dagger M_n.$$

The task is now to determine the operators M_n.

On the other hand we are free in choosing the basis $\{M_n\}$. Therefore we can chose an arbitrary basis $\{M'_n\}$, with the transformation $M_n = \sum_{i \leq N^2} a_i M'_i$. The quantum map E becomes

$$E(\rho) = \sum_{m,n} M'_n \rho M'^\dagger_m \underbrace{a_n a^*_m}_{\chi_{m,n}}. \tag{3.1}$$

Since we have chosen the operators M'_n the only unknown quantity is $\chi_{n,m}$, which is a hermitian matrix. For the following we will call it the χ matrix.

We will determine χ in two steps. In step A we chose a set of density matrices $\{\rho_1, ..., \rho_{N^2}\}$, which parametrize any state ρ. This allows us to write the expression $M'_m \rho_j M'^\dagger_n$ by a linear combination of our set of density matrices $\{\rho_j\}_{j=1,...,N^2}$

$$M'_n \rho_j M'_m = \sum_{k \leq N^2} b^{n,m}_{j,k} \rho_k. \tag{3.2}$$

The coefficients $b^{n,m}_{j,k}$ can be determined by algorithm known from linear algebra.

In step B we prepare experimentally the states $\{\rho_j\}_{j=1,...,N^2}$ and apply the unknown process E, which yields to the new states $\{E(\rho 1), ..., E(\rho N^2)\}$. Using state tomography we can fully determine $E(\rho_j)$. Again we can express the mapping of $E(\rho_j)$ by a linear combination of density matrices $\{\rho_j\}_{j=1,...,N^2}$

$$E(\rho_j) = \sum_{k \leq N^2} c_{j,k} \rho_k. \tag{3.3}$$

By simple linear algebra we find the coefficients $c_{j,k}$.

Now we are almost done. Inserting the two relations Eq. 3.2 and Eq. 3.3 in Eq. 3.1 yields to

$$c_{j,k} = \sum_{n,m \leq N^2} b^{n,m}_{j,k} \chi_{n,m}.$$

This is a matrix equation and we can immediately obtain $\chi_{n,m}$. Even though that we have now quantified the quantum map E by

$$E(\rho) = \sum_{m,n} M'_n \rho M'^\dagger_m \chi_{m,n}$$

we have not yet found the desired operator sum representation. However this can easily be done. We apply a basis transformation U in such a way that U diagonalize χ and we

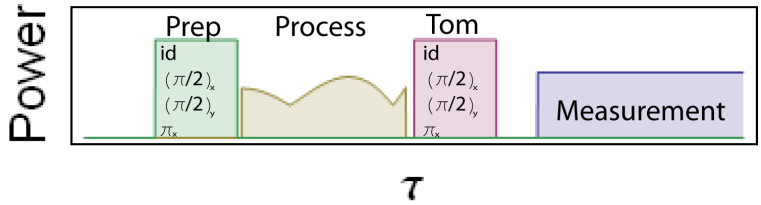

Figure 3.20: Schematic diagram of the pulse sequence, which is used for process tomography. The purple pulses indicate the tomography pulses, which consist here of id, $\left(\frac{\pi}{2}\right)_x$, $\left(\frac{\pi}{2}\right)_x$ and π pulses. However for the analysis just three of the pulses were used. The green pulse indicated the id, $\left(\frac{\pi}{2}\right)_x$, $\left(\frac{\pi}{2}\right)_x$ and π pulses, which were used for preparing the initial density matrices ρ^{in}. The process tomography uses all 16 combinations of these pulses. The process which has to be determined is pictured by a brown pulse. The readout is indicated by the blue pulse.

can find

$$E(\rho) = \sum_{x \leq N^2} \underbrace{\sum_{n \leq N^2} \left(\sqrt{D_{x,x}} U_{x,n} M'_n \right)}_{M_x} \rho \underbrace{\sum_{m \leq N^2} \left(\sqrt{D_{x,x}} U^*_{x,m} M^\dagger_m \right)}_{M_x^\dagger},$$

where D represents the diagonal matrix similar to χ. If the χ matrix is in the diagonal form, the diagonal elements tell us the weighting of each of the operators in the operator sum representation. If χ is not diagonal in the chosen basis, the off diagonal elements show the correlation between the different operators.

Since we experimentally implement process tomography on one qubit, we will now discuss the case for $N = 2$. A straight forward method to implement process tomography on one qubit systems can be found in [6]. We have used this method for the following experiments. In addition we will chose the pure states $(1 \pm \sigma_z)/2$, $(1+\sigma_x)/2$ and $(1+\sigma_y)/2$ since they are easy to be calibrated.

As an interesting example we can perform process tomography on a Hadamard gate. A Hadamard gate consists of a $\left(\frac{\pi}{2}\right)$ rotation around the y axis followed by a π rotation around x axis. This process can be described by the operator

$$H = \frac{1}{\sqrt{2}} \begin{pmatrix} 1 & 1 \\ 1 & -1 \end{pmatrix}.$$

The Hadamard gate maps the ground and exited state on the equally superposed states $(|0\rangle + |1\rangle)/\sqrt{2}$ and $(|0\rangle - |1\rangle)/\sqrt{2}$. This forms with the phase and CNOT gate a set of universal gates and is therefore used in many algorithms [32].

Results:

Similar to the description in the theory part the starting states for the process tomography have been chosen as $\frac{1 \pm \sigma_z}{2}$, $\frac{1+\sigma_x}{2}$, $\frac{1+\sigma_y}{2}$ respectively. For the tomography we used id, $\left(\frac{\pi}{2}\right)_x$ and $\left(\frac{\pi}{2}\right)_y$ pulses. The Hadamard gate has been realized by the pulse sequence $(\pi)_y \circ \left(\frac{\pi}{2}\right)_x$ shown in Fig. 3.21.

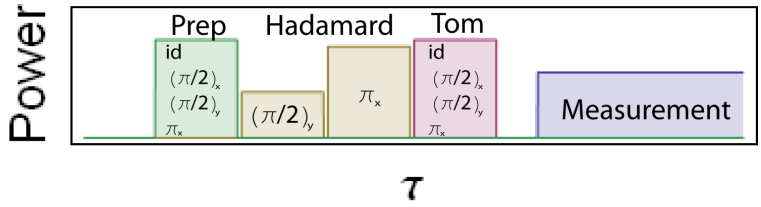

Figure 3.21: The scheme shows the pulse sequence which has been used for the process tomography of the Hadamard gate. The brown pulses are the implementation of the Hadamard gate. The first is a $\left(\frac{\pi}{2}\right)_y$ and the second is a π_y pulse. The Purple pulse is for the tomography and the green for preparation pulse for process tomography. The blue pulse indicates the measurement. Each of the pulses has a length of 20 ns.

For this implementation of a Hadamard gate we can measure for each input state the density matrices of the output state as shown in Fig. 3.22.

The process tomography, which we have implementation and is given in [6], uses the basis set of operators given by $\{1, \sigma_x, i\sigma_y, \sigma_z\}$. The task is now to determine the χ matrix in this basis. From the results shown in Fig. 3.22 we can determine the χ matrix (see Fig. 3.23) by

$$\chi\text{exper} = \begin{pmatrix} 0.02 & 0.02-0.05i & -0.01-0.03i & -0.01-0.15i \\ 0.02+0.05i & 0.43 & 0.01-0.03i & 0.42+0.03i \\ -0.01+0.03i & 0.01+0.03i & 0.06 & 0.02-0.02i \\ -0.01+0.15i & 0.42-0.03i & 0.02+0.02i & 0.49 \end{pmatrix} \text{ and}$$

$$\chi_{\text{theory}} = \begin{pmatrix} 0 & 0 & 0 & 0 \\ 0 & 0.5 & 0 & 0.5 \\ 0 & 0 & 0 & 0 \\ 0 & 0.5 & 0 & 0.5 \end{pmatrix}$$

One can see that the basis $\{1, \sigma_x, i\sigma_y, \sigma_z\}$ is not the canonical basis for the Hadamard gate. The physical basis can be obtained by diagonalising the χ matrix. For this we obtain the operators

$$M_0 = \begin{pmatrix} 0.71-0.15i & 0.61+0.03i \\ 0.66+0.05i & -0.68-0.15i \end{pmatrix}, M_1 = \begin{pmatrix} 0.02-0.11i & -0.27+0.22i \\ -0.07-0.17i & -0.23-0.11i \end{pmatrix},$$

$$M_2 = \begin{pmatrix} -0.18+0.15i & 0.07-0.12i \\ -0.04-0.06i & -0.18-0.1i \end{pmatrix}, M_3 = \begin{pmatrix} 0.09-0.08i & 0.04-0.08i \\ -0.19+0.05i & -0.02-0.08i \end{pmatrix}.$$

We can see that the operator M_0 is close to the operator of a Hadamard gate, which is supposed to be

$$H \approx \begin{pmatrix} 0.71 & 0.71 \\ 0.71 & -0.71 \end{pmatrix}.$$

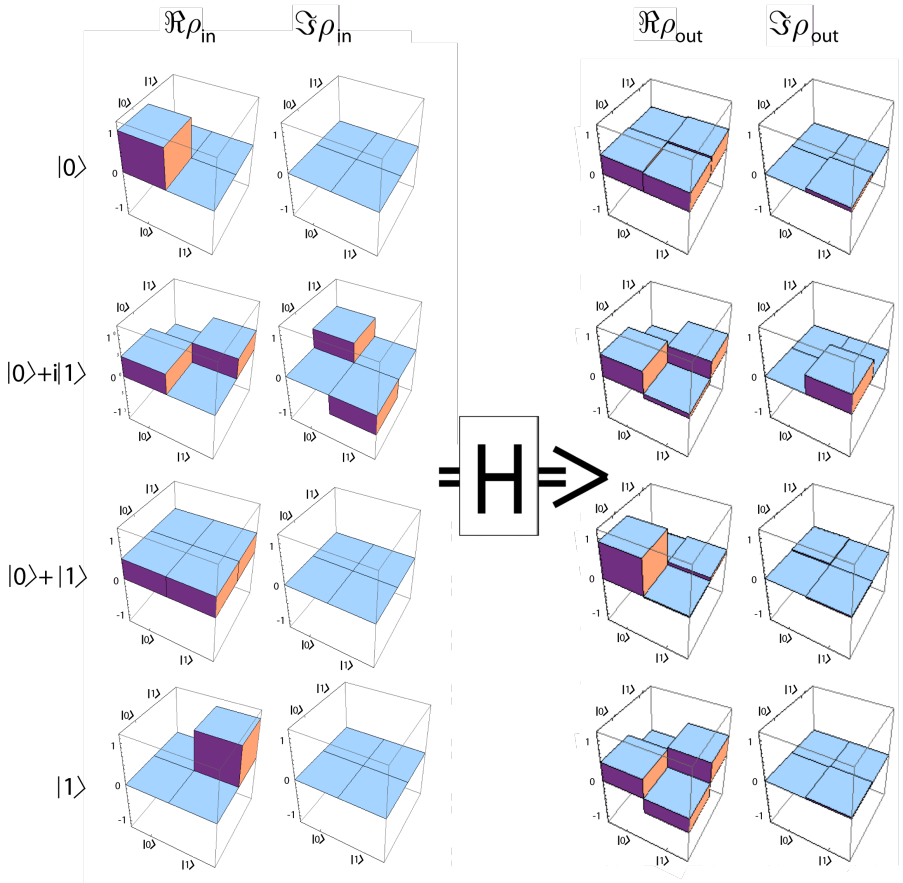

Figure 3.22: The picture shows experimental results of how four different input states transform under the Hadamard gate as implemented above.

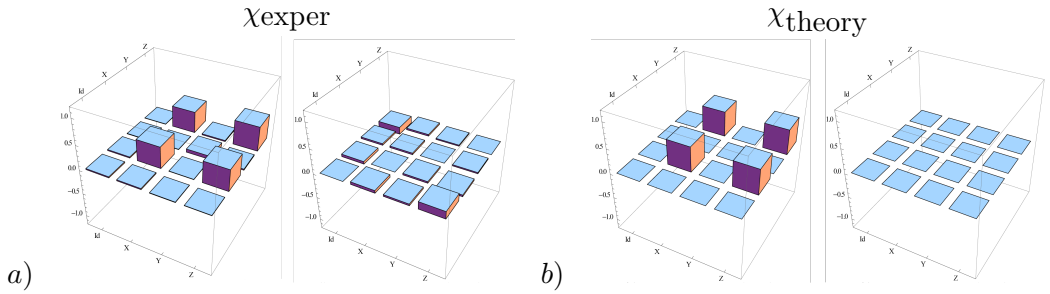

Figure 3.23: The matrices show the real and imaginary part of the χ matrix. The right plot shows the experimental obtained and the left plot shows the theoretical predicted matrix.

Applied pulse sequences:

The measurement has been done pulsed and with a power equivalent of approximately 8 photons in the resonator. For each pulse the length has been chosen to be 20 ns. For the experiment one of the qubit was kept at $\omega_{01} = 5$ GHz ($\omega_r - \omega 01 = 1.4$ GHz) transition frequency while the other was set at the point with $\Phi = 0.5$ flux quantum. The measurement was averaged 600.000 times. For state preparation and tomography id, $\left(\frac{\pi}{2}\right)_x$, $\left(\frac{\pi}{2}\right)_y$ and π_x pulses were used. As mentioned the Hadamard gate was implemented by $\left(\frac{\pi}{2}\right)_x$ and π_y pulses. All this pulses are from the same calibration procedure. Each of the pulses has a length of 20 ns which yields to a total length of 80 ns.

Chapter 4

Tomography of two qubit states

In this chapter we will talk about two qubit tomography. We will perform tomography on different product states. The experiments show nicely how we can map out the density matrix of a multi qubit system. Furthermore, two qubit tomography will be very important if we want to verify the creation of more complicated and entangled states, e.g. Bell states, or if we want to determine the fidelity of a CNOT gate. Moreover, we will implement a most likelihood method, which is a way to find a density matrix that is most likely to create the measured outcome.

4.1 Theory

In this section we explain theoretically how tomography on two qubits can be performed in Circuit QED systems. The first section gives a short introduction into the measurement process for two qubits. We will see this is more difficult than in the case of just one qubit. The second section deals with how the two qubit state can be reconstructed using state tomography. The last section is then introducing the most likelihood method.

4.1.1 Measurement operator

We will discuss the measurement operators, which are available in Circuit QED and how this affects the tomography process. As we will see the system provides us with just one measurement operator, which measure the transmitted microwave field of the resonator. This is interesting because all the other qubit system give the opportunity to readout each qubit individually. We can extract the phase and amplitude of the transmitted field. Since the phase and the amplitude contain the same information the phase was measured in all experiments. Nevertheless it could be desirable to combine the phase and amplitude measurement to improve the readout fidelity. Therefore we will just focus on the phase measurement operator.

Measuring the phase is described by the measurement operator given by

$$M = \Sigma_{i,j\in\{0,1\}} \phi_{ij} \left|ij\right\rangle \left\langle ji\right| ,$$

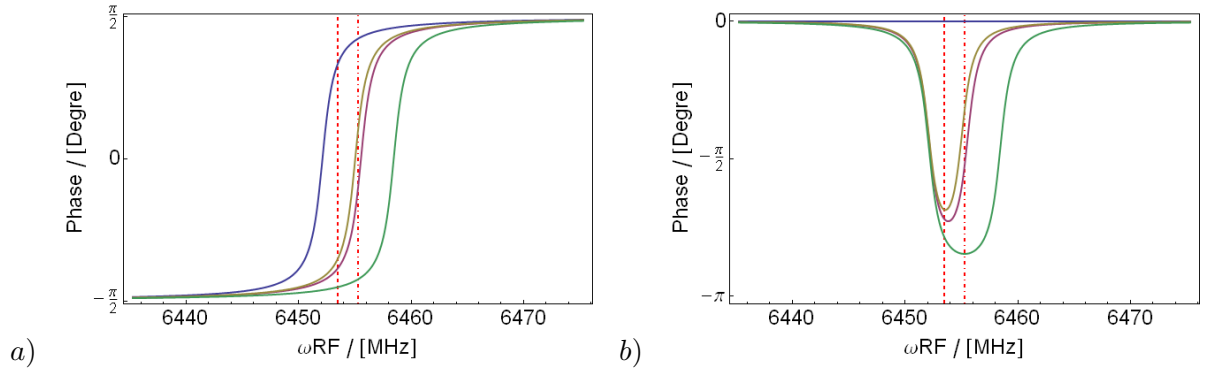

a) *b)*

Figure 4.1: The left plot shows the phase shift of a transmitted microwave as a function of the frequency for our two qubit sample. Since the two qubits have different χ they will have a different Lamb shift and the resonance at a different point. The blue curve shows the response for the $|00\rangle$, the brown for the $|01\rangle$, the purple for the $|10\rangle$ and the green for the $|11\rangle$ state. The right plot shows the phase shift normalized to the ground state. The red dashed line shows a good measurement point, all three states ($|01\rangle$,$|10\rangle$,$|11\rangle$) have large signal. The red pointed-dashed line on the other hand shows the frequency where no measurement should be performed since the A matrix becomes singular (see Section 4.1.2).

where $\langle ij| \hat{=} |ji\rangle^{\dagger}$. The phase shifts $\phi_{i,j}$ for the state $|ij\rangle\langle ji|$ is given by

$$\phi_{i,j} = \arctan\left(\frac{\nu_{\text{meas}}}{\nu_0 + (-1)^{1+i}\chi_A + (-1)^{1+j}\chi_B}\right),$$

with $i, j \in \{0, 1\}$ for the ground and excited state and $\chi_{A,B}$ the dispersive shift for qubit A and qubit B, as shown in Fig. 4.1. If the second excited level is taken into account, which has to be done because of the small anharmonicity [9], $\chi_{A,B}$ can be calculated by

$$\chi_A = \chi_{A,01} - \frac{\chi_{A,12}}{2},$$

where $\chi_{A,mn}$ stands for the dispersive shift from the m^{th} and n^{th} level. The dispersive shift $\chi_{A,mn}$ can be computed by using perturbation theory and gives

$$\chi_{mn} = \frac{g_{mn}^2}{\omega_{mn} - \omega_r},$$

where ω_{mn} is the transition frequency for the n^{th} and m^{th} energy level. However, it turns out that g_{mn} depends strongly on the magnetic flux Φ trough the qubit loop. Therefore, g_{mn} has to be computed individually for each detuning [38].

The measurement at the time t gives the expectation value

$$\phi(t) = Tr\left(M\rho(t)\right),$$

which represents the phase shift of the transmitted microwave at t. In the case of one qubit the measured phase shift is proportional to the population of the excited state p, because $\tilde{\phi} = Tr\left(\phi\,|1\rangle\langle 1|\,\rho\right) = \phi p$. However, this is no longer true for two qubits. It can

easily be seen that different population of the excited state for qubit A and B can yield the same phase shift.

We have just one measurement operator M, which measures the phase shift of the cavity. In all the other physical realization of quantum computing the qubits can be readout individually: in NMR different qubits have different frequencies, in ion traps different ions have different spatial positions, in quantum dots different quantum dots couple to different quantum point contacts and in superconducting flux qubits the readout is realized in a variety of ways for single qubit readout. To our knowledge there is no other system where the qubits are not read out individually.

In principle we could also introduce additional measurement operators and extract the state for different qubits. A possibility would be to measure at different measurement frequencies. Different measurement frequencies would change the phase shift $\phi_{i,j}$ and hence yield a different measurement operator M. However, we will see in the next section that one measurement operator does not pose any constraints for doing state tomography.

4.1.2 Quantum state tomography using 16 pulses

As mentioned above, all other qubit systems are using single qubit readout. In contrast we have to implement a technique which can determine the qubit state by using just one measurement operator. Such a method can be found in [5].

For a 2 qubit system the density matrix is a 4x4 hermitian, positive definite matrix with trace one. Hence, a system of equations has to be found which yields a unique solution for all the 16 entries of the density matrix. A simple way to realize this is to apply a set of 16 different tomography pulses, which yield a system of equations with kernel zero.

In the experiment both qubits are addressed independently over the gate lines. Therefore, the Hamiltonian, which describes the two qubit system, in the rotating wave approximation, can be written in the form [1]

$$
\begin{aligned}
H_{\text{rot}} = \hbar \left(\chi(a^\dagger a + \frac{1}{2}) + \frac{\omega_{01}^A}{2} - \frac{\omega_{\text{drive}}^A}{2} \right) \sigma_z \otimes id + \\
+\hbar \left(\chi(a^\dagger a + \frac{1}{2}) + \frac{\omega_{01}^B}{2} - \frac{\omega_{\text{drive}}^B}{2} \right) id \otimes \sigma_z + \\
+\hbar \frac{g_{01}^A}{\Delta^A} \left(\epsilon_x^A(t)\sigma_x + \epsilon_y^A(t)\sigma_y \right) \otimes id + \\
+\hbar \frac{g_{01}^B}{\Delta^B} id \otimes \left(\epsilon_x^B(t)\sigma_x + \epsilon_y^B(t)\sigma_y \right) + \\
+\hbar J \left(\sigma_+ \otimes \sigma_- + \sigma_- \otimes \sigma_+ \right) + \\
+\hbar \left(\epsilon_x^A(t) + \epsilon_y^A(t) + \epsilon_x^B(t) + \epsilon_y^B(t) \right) (a^\dagger + a).
\end{aligned}
$$

For simplicity we have again used the effective dispersive shift $\chi = \chi_{01} - \chi_{12}/2$, $\omega_r' = \omega_r - \chi_{12}/2$ and $\omega_{01} = \omega_{01} + \chi_{01}$. In addition we have used the raising and lowering operators $\sigma_\pm$. In the Hamiltonian the first two lines represent σ_z rotations due to off resonant driving of the two qubits, the next two terms represent individual single qubit

operations over the gate lines, the following term describes coupling between the two qubits and the last term is skipped. For simplicity we rewrite the Hamiltonian as

$$H_{\text{rot}} = \hbar \Big(\tilde{\Delta}^A \sigma_z \otimes id + \tilde{\Delta}^B id \otimes \sigma_z + (\Omega_{x,1}\sigma_x + \Omega_{y,1}\sigma_y) \otimes id +$$

$$+ id \otimes (\Omega_{x,2}\sigma_x + \Omega_{y,2}\sigma_y) + J\left(\sigma_+ \otimes \sigma_- + \sigma_- \otimes \sigma_+\right)\Big).$$

With the detuning frequency $\tilde{\Delta}^i = \chi(a^\dagger a + \frac{1}{2}) + \frac{\omega_{01}^i}{2} - \frac{\omega^i_{\text{drive}}}{2}$ with $i = A, B$, the Rabi frequency $\Omega_{k,i} = \frac{2g_{01}^i}{\Delta^i}\sqrt{\epsilon_x^i(t) + \epsilon_y^i(t)}$ with $k = x, y$ and $i = 1, 2$ and the coupling constant $J = g^A g^B (1/\tilde{\Delta}^A + 1/\tilde{\Delta}^B)/2$ [3]. In addition resonant driving of the qubits and sufficient detuning between the qubits Fig. 4.3 yield further simplifications of the Hamiltonian for the tomography pulses

$$H_{\text{rot}} = \frac{\hbar}{2}\left((\Omega_{x,1}\sigma_x + \Omega_{y,1}\sigma_y) \otimes id + id \otimes (\Omega_{x,2}\sigma_x + \Omega_{y,2}\sigma_y)\right).$$

Again the tomography pulses have been assumed to be much shorter in time than the decoherence time.

We will now show that a full two qubit tomography can be done, if we perform on both qubits all 16 combinations of the id, $\left(\frac{\pi}{2}\right)_x$, $\left(\frac{\pi}{2}\right)_y$ and $(\pi)_x$ pulses. These pulses will also be the tomography pulses, which we use for tomography in the experiment.

The time evolution of the density matrix can be written as

$$\rho(0) = \exp\left[-i\frac{H_{i,j}}{\hbar}\tau\right]\rho(-\tau)\exp\left[i\frac{H_{i,j}}{\hbar}\tau\right],$$

where $\rho(0)$ is the density matrix immediately after the tomography pulse and $\rho(-\tau)$ the density matrix right before applying the pulses. The indices i, j in the Hamiltonian $H_{i,j}$ indicates what kind of pulses $\left(i, j = \left\{id, \left(\frac{\pi}{2}\right)_x, \left(\frac{\pi}{2}\right)_y, (\pi)_x\right\}\right)$ have been applied on qubit A, qubit B respectively. In calculations the matrix exponential has been computed by Mathematica6.0 which uses Jordan form. The matrix representation of the operators $U_{i,j} = \exp\left[-iH_{i,j}/(2\hbar)\tau\right]$ are given in the appendix 5.2.

The measured response for all 16 operators give the system of equations

$$\left| p_k = \text{Tr}\left(\exp[-i\frac{H_{i,j}}{\hbar}\tau]M\exp[i\frac{H_{i,j}}{\hbar}\tau]\rho\right)\right|_{i,j=\left\{id,\left(\frac{\pi}{2}\right)_x,\left(\frac{\pi}{2}\right)_y,(\pi)_x\right\}}$$

For id, $\left(\frac{\pi}{2}\right)_x$, $\left(\frac{\pi}{2}\right)_y$ and $(\pi)_x$ pulses we can write down the system of equations. For this we first parametrize the density matrix by

$$\rho = \frac{1}{4}\sum_{i,j=0,x,y,z} r_{i,j}\sigma_i \otimes \sigma_j.$$

This is a parameterization for an arbitrary hermitian matrix. It is emphasized that the matrix does not satisfy the condition $Tr(\rho) = 1$ nor is the matrix positive definite. However, the normalization condition can easily be satisfied by $\tilde{\rho} = \rho/Tr(\rho)$.

If we use the isomorphism $r_k \mapsto r_k \vec{e}_k$, we can write the system of equations by

$$\sum_{i=0}^{16} a_{i,j} r_i = p_j.$$

The matrix $A = (a_{i,j})$ is given in the appendix 5.2.

We can now analyze which conditions the measurement operator M has to fulfill to ensure that the system of linear equations has a unique solution. The condition for linear independency is than given by $\det(a_{i,j}) \neq 0$. This yields the condition $M_3 \neq M_1 + M_2$, $M_3 \neq -(M_1 + M_2)$ and $M_3 \neq \pm(M_1 - M_2)$. However, the conditions $M_3 \neq -(M_1 + M_2)$ and $M_3 \neq \pm(M_1 - M_2)$ are not physical, this can easily be seen from the chapter on measurement operator 4.1.1. The quantity $M_3 = M_1 + M_2$ on the other hand can occur. Therefore, we are restricted to perform our measurements not at that frequency where $M_3 = M_1 + M_2$.

4.1.3 Most likelihood method

As mentioned above, if the density matrix is determined by solving the system of linear equations, the resulting matrix will not necessarily be positive definite. This is caused by a statistical noise in the measurement response p_k. However, the most likelihood method gives us the possibility to find a matrix which fulfills all requirement to be a density matrix. The method computes a positive definite hermitian matrix with $Tr(\rho) = 1$, which is most likely to produce the response measured in the experiment. The following discussion has been written according to [5].

The most likelihood method uses a matrix $\widetilde{\rho}(t_1, t_2, ..., t_{16})$, which has been parametrized in such a way that it describes only positive definite hermitian matrices with $Tr(\widetilde{\rho}) = 1$. Furthermore a likelihood function $\Theta(t_1, t_2, ..., t_{16}, p_1, p_2, ..., p_{16})$ has to be introduced, which is a measure for the probability that a density matrix $\widetilde{\rho}(t_1, t_2, ..., t_{16})$ will give the response $\{p_1, p_2, ..., p_{16}\}$. Finally the function Θ has to be maximized.

Since a hermitian matrix $\widetilde{\rho}$ is positive definite if and only if it can be written in the form $\widetilde{\rho} = T^\dagger T$ we only have to parametrize T. This can easily be seen by

$$0 \overset{?}{<} \langle\varphi|\widetilde{\rho}|\varphi\rangle = \left\langle \varphi | T^\dagger T | \varphi \right\rangle = \langle\varphi'|\varphi'\rangle > 0 \text{ for } |\varphi\rangle \neq 0$$

The matrix $\widetilde{\rho} = T^\dagger T$ is also hermitian because $\widetilde{\rho}^\dagger = (T^\dagger T)^\dagger = T^\dagger T = \widetilde{\rho}$. To minimize computation for inverting the matrix T, we parametrize T as a triangle matrix

$$T = \begin{pmatrix} t_1 & 0 & 0 & 0 \\ t_5 + it_6 & t_2 & 0 & 0 \\ t_{11} + it_{12} & t_7 + it_8 & t_3 & 0 \\ t_{15} + it_{16} & t_{13} + it_{14} & t_9 + it_{10} & t_4 \end{pmatrix}$$

Trace one is simply ensured by $\widetilde{\rho} = T^\dagger T / \mathrm{Tr}(T^\dagger T)$.

In a simple model it is assumed that the noise on the response $\{p_1, p_2, ..., p_{16}\}$ is Gaussian distributed. Due to the central limit theorem the assumption is true for almost all physical cases. However, in our system the phase is measured. Since the phase is a periodical function it will not be normal distributed. Nevertheless, if the amplitude is larger

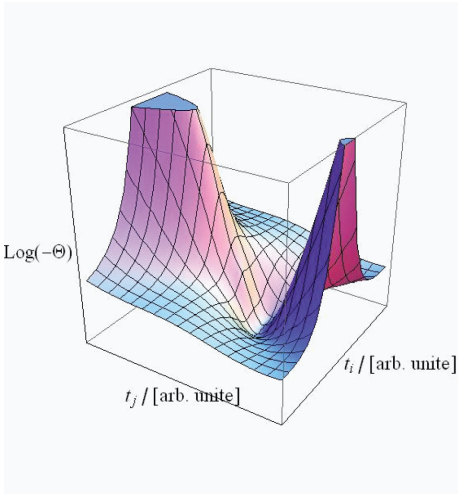

Figure 4.2: The picture shows schematically the likelihood function, which is parametrized in t_i. Of course a two qubit system requires an optimization in $t_1, t_2, ..., t_{16}$. This can easily be done numerically.

then the standard deviation, we can assume a Gaussian distribution. The probability to obtain the response $\{p_1, p_2, ..., p_{16}\}$ for uncorrelated p_i, which is the case, is determined by

$$\Theta(t_1, t_2, ..., t_{16}) = \prod_{k=1}^{16} \exp\left[-\frac{(p_k - \widetilde{p_k})^2}{2\sigma_k^2}\right],$$

where $\widetilde{p_k}$ is the expectation value given by $\widetilde{p_k} = Tr\left(U_k M U_k^\dagger \widetilde{\rho}\right)$ and σ_k is the standard deviation given by $\sigma_k = \sqrt{\widetilde{p_k}}$. The likelihood function becomes

$$\Theta(t_1, t_2, ..., t_{16}) = \exp\left[-\sum_{k=1}^{16} \frac{\left(p_k - \mathrm{Tr}\left(U_k M U_k (T^\dagger T/\mathrm{Tr}(T^\dagger T))\right)\right)^2}{2\mathrm{Tr}\left(U_k M U_k (T^\dagger T/\mathrm{Tr}(T^\dagger T))\right)}\right].$$

The task is now to maximize the likelihood function. Since the logarithms is a one to one mapping maximizing Θ is equivalent to minimizing $\theta = -\log[\Theta]$. The minimization has to be done numerically. A routine is implemented in Mathematica6.0 under the command FindMinimum. The function FindMinimum requires a starting value for the algorithm. As starting value the density matrix ρ_{start} found from solving the system of equations above is used. The starting values for $\{t_1, t_2, ..., t_{16}\}$ are then given by

$$T = \begin{pmatrix} \sqrt{\frac{\det(\rho_{start})}{\det(\rho_{start}^{11})}} & 0 & 0 & 0 \\ \frac{\det(\rho_{start}^{12})}{\sqrt{\det(\rho_{start}^{11})\det(\rho_{start}^{11,22})}} & \sqrt{\frac{\det(\rho_{start}^{11})}{\det(\rho_{start}^{11,22})}} & 0 & 0 \\ \frac{\det(\rho_{start}^{12,23})}{\sqrt{\rho_{start,44}\det(\rho_{start}^{11,22})}} & \frac{\det(\rho_{start}^{11,23})}{\sqrt{\rho_{start,44}\det(\rho_{start}^{11,22})}} & \sqrt{\frac{\det(\rho_{start}^{11,22})}{\rho_{start,44})}} & 0 \\ \frac{\rho_{start,41}}{\sqrt{\rho_{start,44}}} & \frac{\rho_{start,42}}{\sqrt{\rho_{start,44}}} & \frac{\rho_{start,43}}{\sqrt{\rho_{start,44}}} & \sqrt{\rho_{start,44}} \end{pmatrix}.$$

In the above formula the expression ρ_{start}^{ij} stands for the matrix ρ_{start} where the i^{th} row and the j^{th} column has been deleted. Similar $\rho_{start}^{ij,kl}$ stands for the matrix where the i^{th} and the k^{th} row, the j^{th} and the l^{th} column has been deleted.

Since the density matrix has only real numbers on the diagonal the real part of the diagonal elements is taken instead.

4.2 Experimental setup

The experimental setup differs only in one major point from the setup described in the previous chapter. The big difference is that we have to add one more channel to control the second qubit. Since we want to manipulate both qubits individually ($\sigma_i \otimes id$ and $id \otimes \sigma_j$) we drive them over two different charge gate lines. Measurements done in our lab confirm that the gate lines address the qubits locally. In addition the qubits are detuned from each other which also prevents a coupling between the gate line to the opposite qubit. This justifies the assumption that the two qubits can be addressed individually. In Section 4.3 we will show that the two qubits are essentially uncoupled from each other, at least for the used detuning.

The drive for the second qubit is created with an additional microwave generator. Again the amplitude and phase of the second drive are set by a I/Q mixer. The mixer's I and Q channel are controlled by dc voltage pulses which comes from an AWG. Similar to the one qubit experiment the mixer is driven continuously, which requires a high on/off ratio (see Section 3.2). This is achieved by adjusting the mixer's offset. The output is measured by the same spectrum analyzer as the output for the first mixer (see Section 3.2) but at a different frequency, see Fig. 4.3.

4.3 Experimental approach

Here we will talk about the difference between two qubit tomography and one qubit tomography. First we will justify the assumption that qubit-qubit interaction can be neglected on the time scale on which the experiments were performed. Then we will explain how the pulse sequence for the I/Q mixer was arranged. Next we will talk about the way how a phase shift is extracted from the measurement data. Last the calibration procedure for the $\left(\frac{\pi}{2}\right)$ and π pulses will be discussed.

Qubit-qubit interaction

As mentioned in the theory Section 4.1.2, it is important that the two qubits do not interact with each other. Otherwise the

$$\hbar J(\sigma_+ \otimes \sigma_- + \sigma_- \otimes \sigma_+)$$

term in the Hamiltonian would cause a $\sqrt{i\text{SWAP}}$ interaction corresponding to the σ_x term. This coupling can be suppressed by a strong detuning between the two qubits.

In general the qubit-qubit interaction is suppressed if the condition $J << |\omega_{01}^A - \omega_{01}^B|$ is satisfied [3]. The coupling constant has been determined by Martin Goeppl by measuring

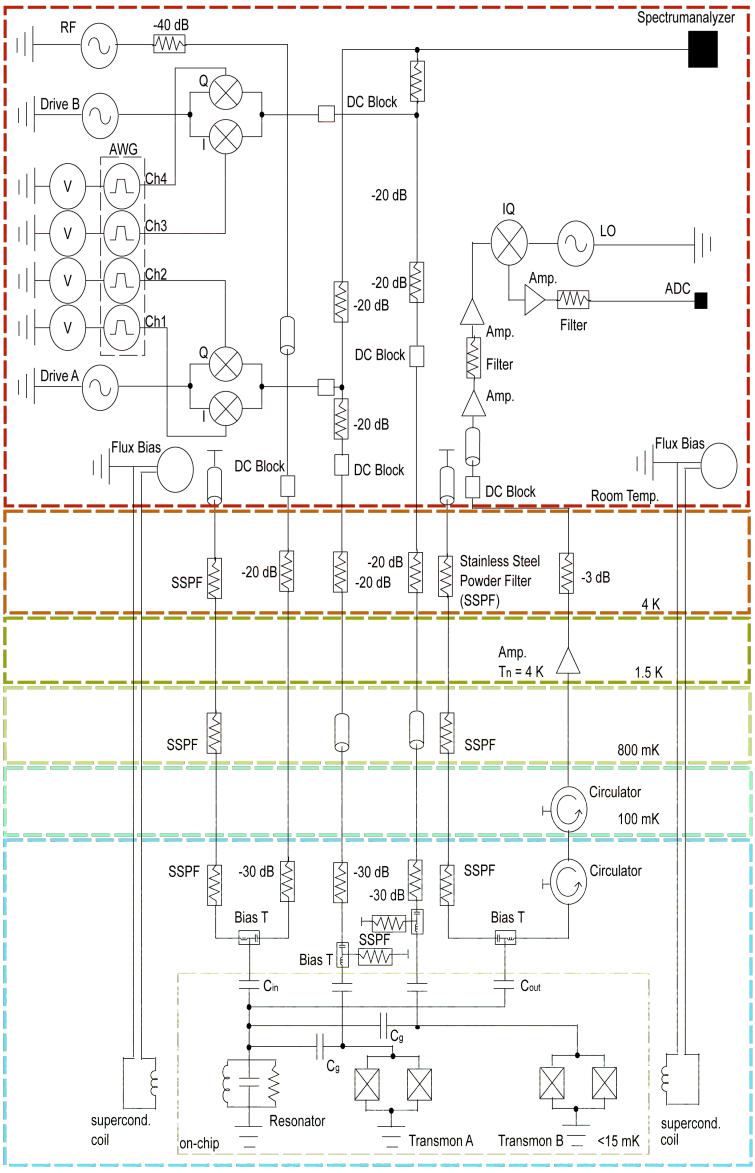

Figure 4.3: The picture shows schematically the experimental setup used for the two qubit experiments. The only difference to the setup for one qubit experiments is that the second gate line is used as well. This means an additional microwave generator connected to a I/Q mixer has been added to the system. The mixer is controlled by dc pulses coming form an AWG. Similar to the one qubit experiment a splitter is placed after the mixer which brings one part of the microwave to the qubit while the other part goes to the spectrum analyzer. In addition the attenuation inside the fridge has been changed, since it had been determined that thermal photons were in the resonator.

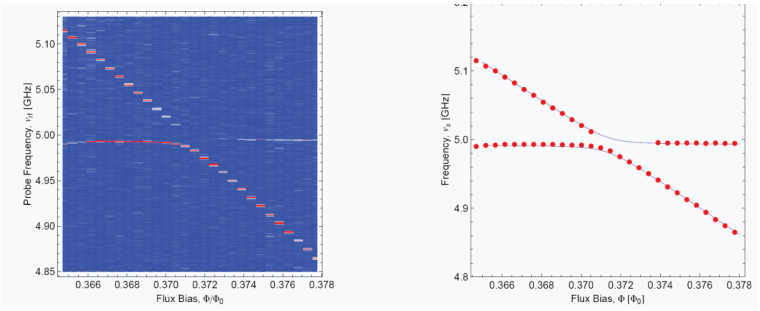

Figure 4.4: The left hand side shows spectroscopy for the two qubits as a function of the magnetic flux Φ, which detunes the two qubits. The right hand side shows the extracted transition frequencies. For the measurements one qubit has been kept at a constant detuning of 5 GHz while the other one has been frequency. One can clearly see a dark state $|01\rangle + |10\rangle$, which yields from a symmetrical arrangement of the qubits in the cavity [3]. This measurement and the analysis have been done by Martin Goeppl.

the splitting of the two qubits in resonance. For 5 GHz and 4.85 GHz qubits transition frequencies a coupling constant of $J = 14$ MHz can be observed, see Fig. 4.4. In our experiment the qubits were detuned by $|\omega_{01}^A - \omega_{01}^B| = 150$ MHz. This detuning and J causes fluctuations in the qubit-qubit population which are less then 1%.

Applied pulse sequence

The difference to the one qubit experiment is that we have now a second microwave generator with a second I/Q mixer. Since we want to control the two mixers independently we need two additional pattern files, for the I/Q channel of the second mixer. The used AWG has four outputs, which create dc voltage pulses with a 1 ns time and a 10 bit amplitude resolution. These pulses can be used to control both mixers.

Measurement process

In the measurement process we determine the phase shift of the transmitted microwave field as a function of time. For one qubit it can be shown [29] that an accurate and convenient way to determine the populations is not to compare the cavity's phase shift ϕ but the weighted average with the theoretical response (see Section 3.3). For two qubits we can use a similar procedure.

For each set of measurements $p(t)$ we calculate the weighted average

$$\tilde{p}_k = \frac{\sum_t f(t)p(t)}{\sum_t f^2(t)}. \tag{4.1}$$

The weighting function $f(t)$ is chosen by $f(t) = \exp[-t/\lambda]$, the damping factor λ is kept for the analysis at a fix value and on the order of $\min\{T_1\}$, see Fig. 4.5. It is important to notice that the weighted average is not equal the population of any of the excited states. It is even not possible to extract the population of the excited states of the two qubits just from this data. Additional measurements would be required to determine the population.

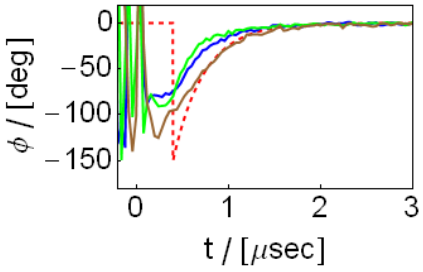

Figure 4.5: The plot shows the phase shift for three different measurements. Here green is π pulse on qubit A, blue π pulse on qubit B and brown π pulse on both of them. The red line indicated the weighting function $f(t)$. This measurements allow us to calculate the measurement operator M. Analogous measurement give the response $p_k = \mathrm{Tr}\left(U_k M U_k^\dagger \rho\right)$.

The new measurement operator on the other hand can be written by

$$\tilde{M} = \Sigma_{i,j\in\{0,1\}} \tilde{p}_{|ij\rangle\langle ji|} \left|ij\right\rangle \left\langle ji\right|,$$

where $\tilde{p}_{|ij\rangle\langle ji|}$ is the weighted average defined in Eq. 4.1 for a state starting in $|ij\rangle\langle ji|$. This measurement operator can either be derived theoretically by using cavity Bloch equations [39] for two none interacting qubits or by measuring the response after applying a π pulse on qubit A or on qubit B or on both of them simultaneously. Both methods allow to determine the measurement operator M. For the experiment we have chosen to determine M by applying π pulses. The main reason for this is because we do not have the cavity Bloch equations for two qubits available.

The system of equations becomes then

$$\tilde{p}_k = \mathrm{Tr}\left(U_k \tilde{M} U_k^\dagger \rho\right).$$

Since the quantities $\tilde{p}$ and $\tilde{M}$ are in close relation with p_k and M we will not distinguish any more between them. From the context it should be clear which quantities we are referring to.

Relative phase between different gate lines

In the two qubit tomography we are driving both qubits over different gate lines. However this raises the question whether this has an influence on the result of the tomography process or not. We will now show that this constant phase shift affects the reconstruction of the density matrix. Similar problems are known form tomography on ions [40].

We can assume the two pulses have a phase difference φ. If we create now a tomography pulse U_k and send it through the gate lines, the microwave will pick up an additional phase φ, which yields a new tomography pulse

$$\tilde{U}_k = S U_k S^\dagger,$$

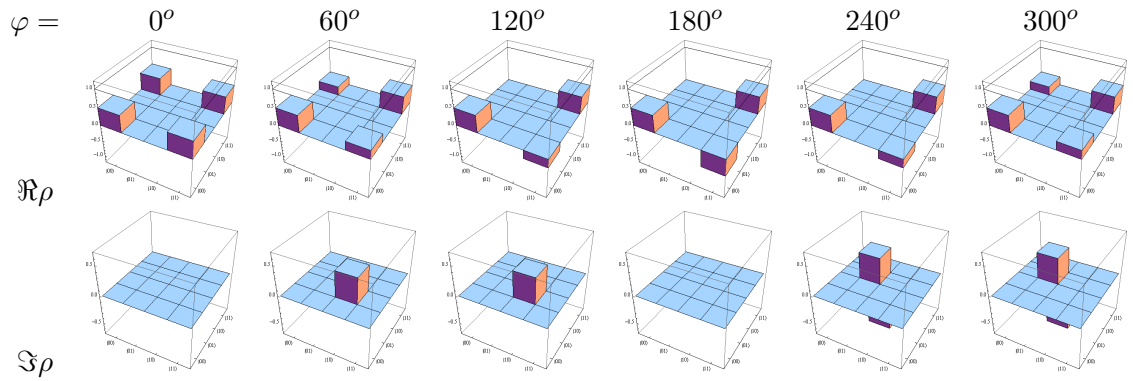

Figure 4.6: The plot shows simulations for reconstructed density matrices for a Bell state $|00\rangle\langle 00| + |11\rangle\langle 11|$ and an relative phase shift of $\varphi = 0^o$, 60^o, 120^o, 180^o, 240^o and 300^o.

where the transformation is given by $S = \exp[-i\varphi\sigma_z \otimes id]$. This yield us the system of equations

$$\left| p_k = \mathrm{Tr}\left(SU_k S^\dagger M S U_k^\dagger S^\dagger \rho\right)\right|_{k=1,\ldots,16} \text{, instead of } \left| p_k = \mathrm{Tr}\left(U_k M U_k^\dagger \rho\right)\right|_{k=1,\ldots,16}.$$

However, if we do not know anything about the phase shift φ, we will use the wrong operators U_k and hence reconstruct a state which is out of phase. We can easily see how this affects the result of the tomography process.

$$p_k = \mathrm{Tr}\left(SU_k S^\dagger M S U_k^\dagger S^\dagger \rho\right)$$

$$p_k = \mathrm{Tr}\left(U_k M U_k^\dagger S^\dagger \rho S\right),$$

where we have used $[S, M] = 0$. This phase shift S makes us believe that we are measuring the density matrix $S^\dagger \rho S$ instead of ρ, see Fig. 4.6. An possibility to determine this relative phase difference would be to prepare a known product state over the resonator and read it out by tomography.

Manual calibration of the tomography pulses

Similar to the one qubit tomography the $\left(\frac{\pi}{2}\right)$ and π pulses for the tomography have to be calibrated. However, this time we need to calibrate $\left(\frac{\pi}{2}\right)_x$, $\left(\frac{\pi}{2}\right)_y$ and π pulses for the first and $\left(\frac{\pi}{2}\right)_x$, $\left(\frac{\pi}{2}\right)_y$ and π pulses for the second qubit. The amplitude has been calibrated by measuring the population of the excited state as a function of the pulse amplitude (see previous chapter Fig. 3.3 and 3.3.1). The phase between $\left(\frac{\pi}{2}\right)_x$ and $\left(\frac{\pi}{2}\right)_y$ has been adjusted according to the calibration done by a vector network analyzer (see appendix). However, this calibration does not give any hint on the relative phase difference between the two different drive. A different way to calibrate the phase has to be applied. However we will see that for our experiment this additional phase shift does not matter as we will see in Section 4.4.

4.4 Experiment

To show the tomography procedure we will discuss the results of a two qubit state tomography. In the experiment we have performed tomography on 16 different product states. The product states have been prepared by performing on each qubit either no pulse, a $\left(\frac{\pi}{2}\right)_x$, $\left(\frac{\pi}{2}\right)_y$ or π pulse. First we reconstruct the density matrices by solving the system of linear equations. For these states we calculate the L_1 norm. Furthermore, we apply a most likelihood procedure to find physical density matrices. This enables us to determine the fidelity compared to perfect pulses.

For the tomography we use all possible combinations of id, $\left(\frac{\pi}{2}\right)_x$, $\left(\frac{\pi}{2}\right)_y$ or π pulses applied on each of the qubit. We can reconstruct the tomography pulses in the same way as we reconstructed the tomography pulses for the case of one qubit (see Section 3.4.3) and we find

$$U_1^A = \begin{pmatrix} 0.74 \pm 0.02 & -0.67i \pm 0.02i \\ -0.67i \pm 0.02i & 0.74 \pm 0.02 \end{pmatrix} \text{ and}$$

$$U_2^A = \begin{pmatrix} 0.70 \pm 0.03 & (-0.71 + 0.05i) \pm (0.02 + 0.04i) \\ (0.71 + 0.05i) \pm (0.02 + 0.04i) & 0.70 \pm 0.03 \end{pmatrix},$$

$$U_1^B = \begin{pmatrix} 0.76 \pm 0.03 & -0.64i \pm 0.04i \\ -0.64i \pm 0.04i & 0.76 \pm 0.03 \end{pmatrix} \text{ and}$$

$$U_2^B = \begin{pmatrix} 0.76 \pm 0.02 & (-0.64 + 0.13i) \pm (0.03 + 0.04i) \\ (0.64 + 0.13i) \pm (0.03 + 0.04i) & 0.76 \pm 0.02 \end{pmatrix},$$

where we have used the fact that the two qubits are not coupled (Section 4.3). Applying the useful formula $\exp(-i\vec{\sigma}\cdot\vec{n}\alpha/2) = \cos(\alpha/2)\,\mathrm{id} - i\vec{\sigma}\cdot\vec{n}\sin(\alpha/2)$ we can calculate the orientation and rotation angle for the tomography pulses represented as operations in $SO(3)$. For the pulses determined above we find

	U_1^A	U_2^A	U_1^B	U_2^B
rotation angle :	85^o	91^o	81^o	81^o
$\angle(U_1, U_2)$:		86^o		100^o

.

This justifies the assumption of perfect tomography pulses. For simplicity we assume perfect tomography pulses. We can find for the equation $\sum_{i=1}^{16} a_{i,j} r_i = p_j$ the parameters $a_{i,j}$ as given in the appendix 5.2. The matrix $(a_{i,j})_{i,j=\{1,2,3,4\}}$ can be inverted, since the measurement operator M fulfills the requirements $|M_{3,3}| \neq |M_{1,1} \pm M_{2,2}|$.

We obtain the density matrices shown in Fig. 4.8. To check the deviation from the theoretical value we can calculate the $L_1 = \frac{1}{2}\mathrm{Tr}\left|\rho_{\mathrm{theory}} - \rho_{\mathrm{experiment}}\right|$ norm. We find in Fig. 4.8 that the reconstructed states are in good agreement with the theoretical expected density matrices.

Furthermore we can apply the most likelihood procedure as described in the theory section. This has the advantage to obtain matrices, which are positive definite and describe therefore physical solutions. These results are shown in Fig. 4.10. From this solution we can now calculate the fidelity $F = \mathrm{Tr}\left(\sqrt{\sqrt{\rho_{\mathrm{theory}}}\rho_{\mathrm{experiment}}\sqrt{\rho_{\mathrm{theory}}}}\right)$.

In the previous section we have found that a phase shift $S = \exp(-i\varphi\sigma_z \otimes id)$ can cause problems to reconstruct the qubits state. However, we do not see such an effect in the presented results. The reason for that is because we use the same gate lines to prepare the state ρ as we use for the tomography pulse and hence the rotation S cancels out. We prove that by

$$p_k = \mathrm{Tr}\left((SU_kS^\dagger)^\dagger M(SU_kS^\dagger)\rho\right)$$

$$p_k = \mathrm{Tr}\left((SU_kS^\dagger)^\dagger M(SU_kS^\dagger)(SRS^\dagger)\left|00\right\rangle\left\langle 00\right|(SRS^\dagger)^\dagger\right)$$

$$p_k = \mathrm{Tr}\left(SU_k^\dagger S^\dagger MSU_kRS^\dagger\left|00\right\rangle\left\langle 00\right|SR^\dagger S^\dagger\right),$$

where we have written the state preparation by $\rho = (SRS^\dagger)\left|00\right\rangle\left\langle 00\right|(SRS^\dagger)^\dagger$. If we use the commutation relation $S\left|ij\right\rangle\left\langle ji\right| = \left|ij\right\rangle\left\langle ji\right|S$ and the commutation relation for the trace, the expectation value becomes

$$p_k = \mathrm{Tr}\left(U_k^\dagger MU_kR\left|00\right\rangle\left\langle 00\right|R^\dagger\right) = \mathrm{Tr}\left(U_k^\dagger MU_k\rho_{\mathrm{theory}}\right).$$

However, it is emphasized that this is only true if we use the same gate lines for the tomography as for the state preparation.

Applied pulse sequence:

To produce the desired product state we first apply on each of the qubits either no pulse or a $\left(\frac{\pi}{2}\right)$ pulse or a π pulse. After that we perform the tomography by using the 16 different $U_{i,j}$ operations, with $(i,j) = \left\{id, \left(\frac{\pi}{2}\right)_x, \left(\frac{\pi}{2}\right)_y, \pi\right\}$. This is schematically shown in Fig. 4.7. To ensure a proper calibration we have also added a calibration pulse sequence. The calibration sequence works analogously to the auto calibration sequence for one qubit. Since we have two qubits we perform calibration pulses on each of the qubits individually. The measurement has been performed pulsed with approximately 8 photons in the resonator. The two qubits were at transition frequencies of $\omega_{01}^A = 5$ GHz and $\omega_{01}^B = 4.85$ GHz ($\omega_r - \omega_{01}^A = 5$ GHz/$\omega_r - \omega_{01}^B = 1.65$ GHz detuned from the resonator) as discussed in Section 4.3. All the measurements have been averaged 600.000 times.

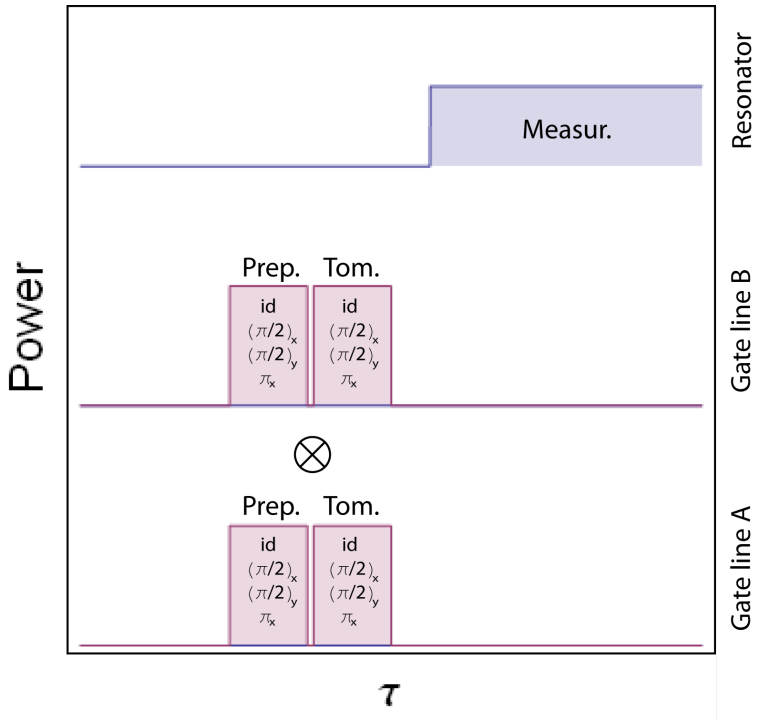

Figure 4.7: The figure shows a systematical picture of the pulse sequence for the tomography process. The lower two pulse sequence show the microwave pulse which are applied on the gate lines. These pulses are used for the state preparation and the tomography. The uppermost graphic shows the measurement pulse which is applied on the resonator. Each of the tomography and preparation pulse had a pulse length of 20 ns.

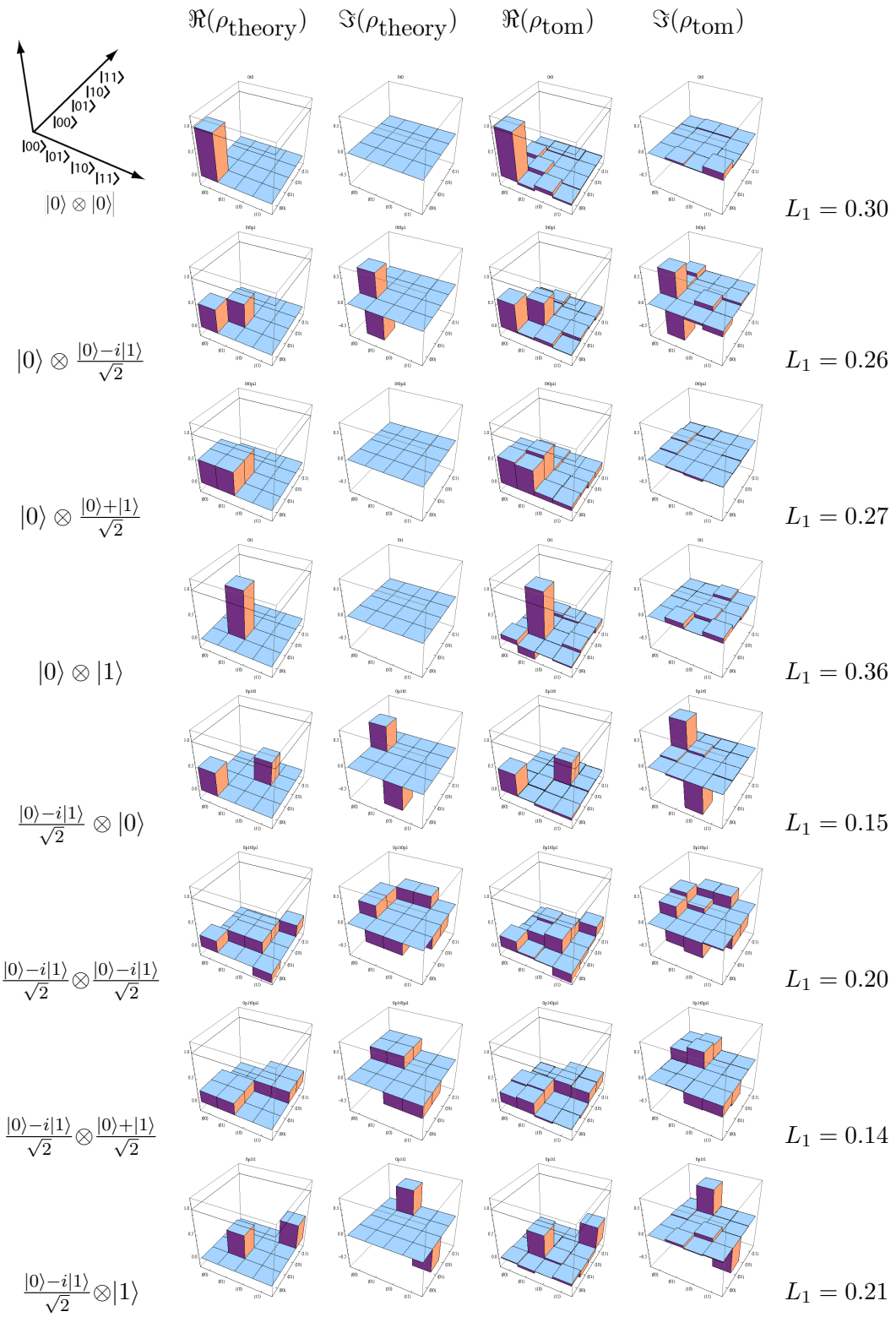

Figure 4.8: The graphic shows eight different product states for two qubits. The most left column names the wave function which we intend to map the second and third one show the real and imaginary part of theoretical density matrix for the corresponding state. The next two columns give real and imaginary part for the measured density matrices using tomography. The number shows the $L_1(\rho_{\text{theory}}, \rho_{\text{experiment}})$ norm for the theory and experiment.

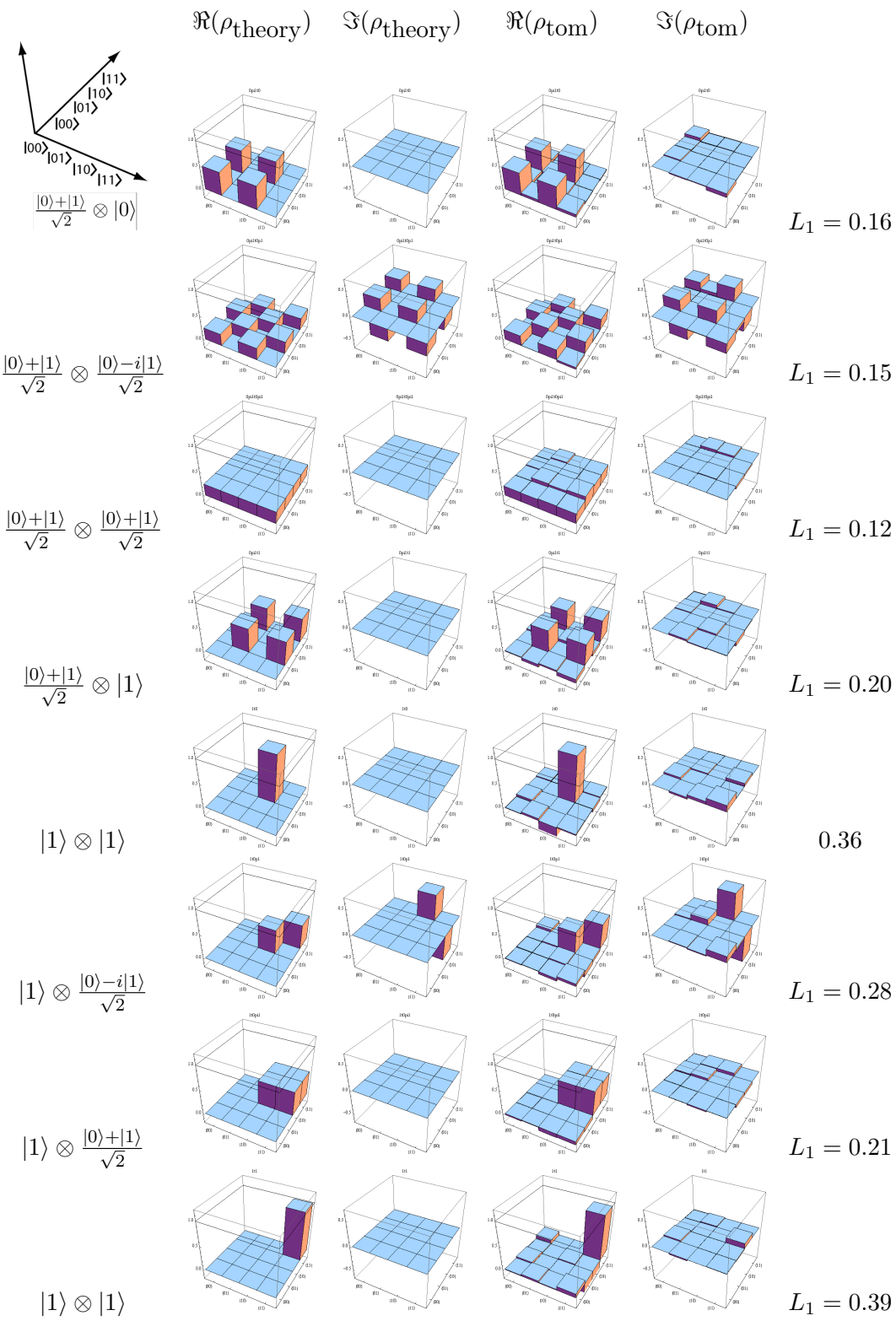

Figure 4.9: Continue from Fig. 4.8.

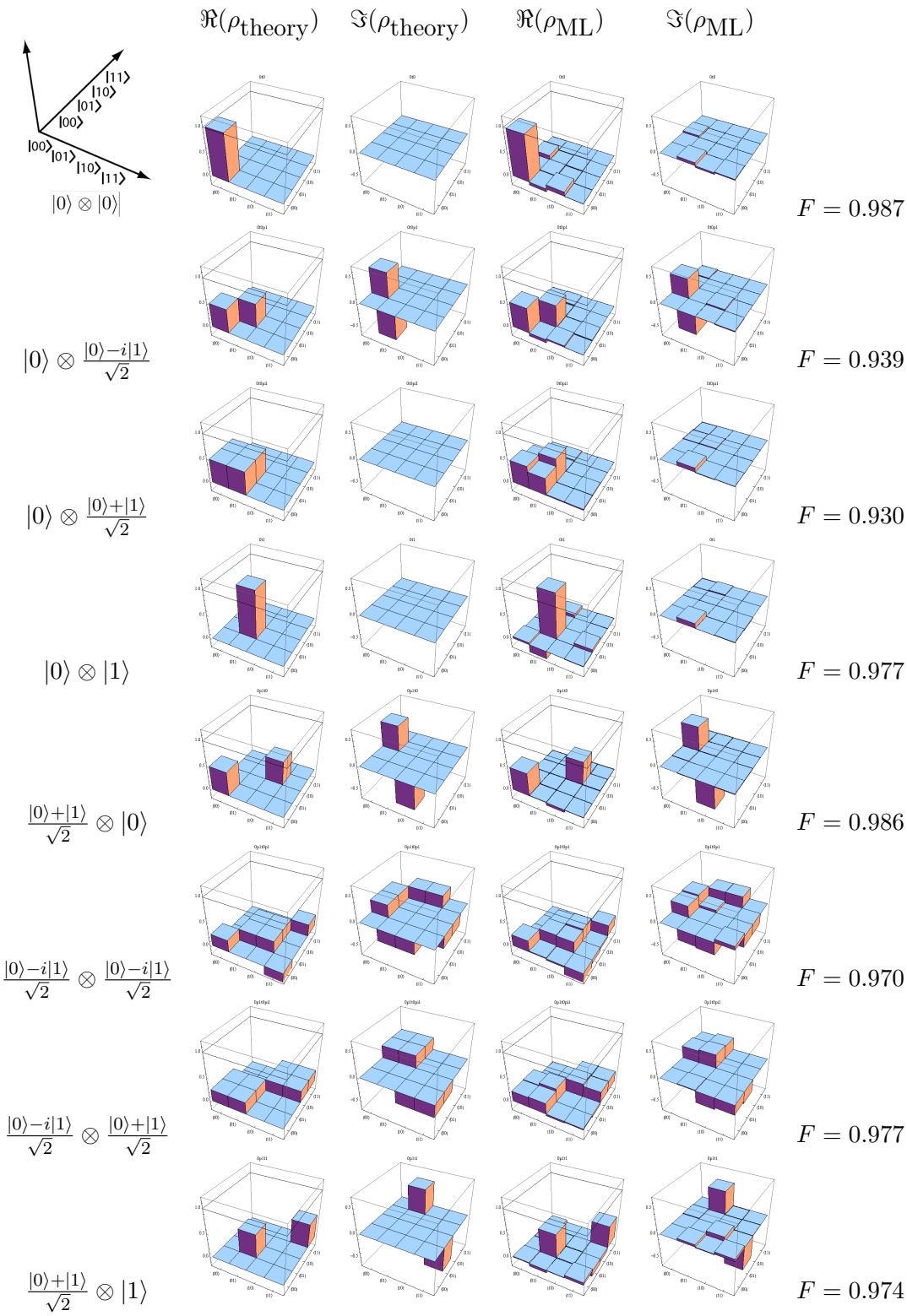

Figure 4.10: The plots show eight different product states for two qubits. The most left column labels the wave function, which we intend to map the second and third one show the real and imaginary part of theoretical density matrix for the corresponding state. The following two columns represent the real and imaginary part for the density matrices which can be observed if we use a most likelihood procedure. The number to the left gives the fidelity $F(\rho_{\text{theory}}, \rho_{mostlikelihood})$ for the theory and matrix found by the most likelihood procedure.

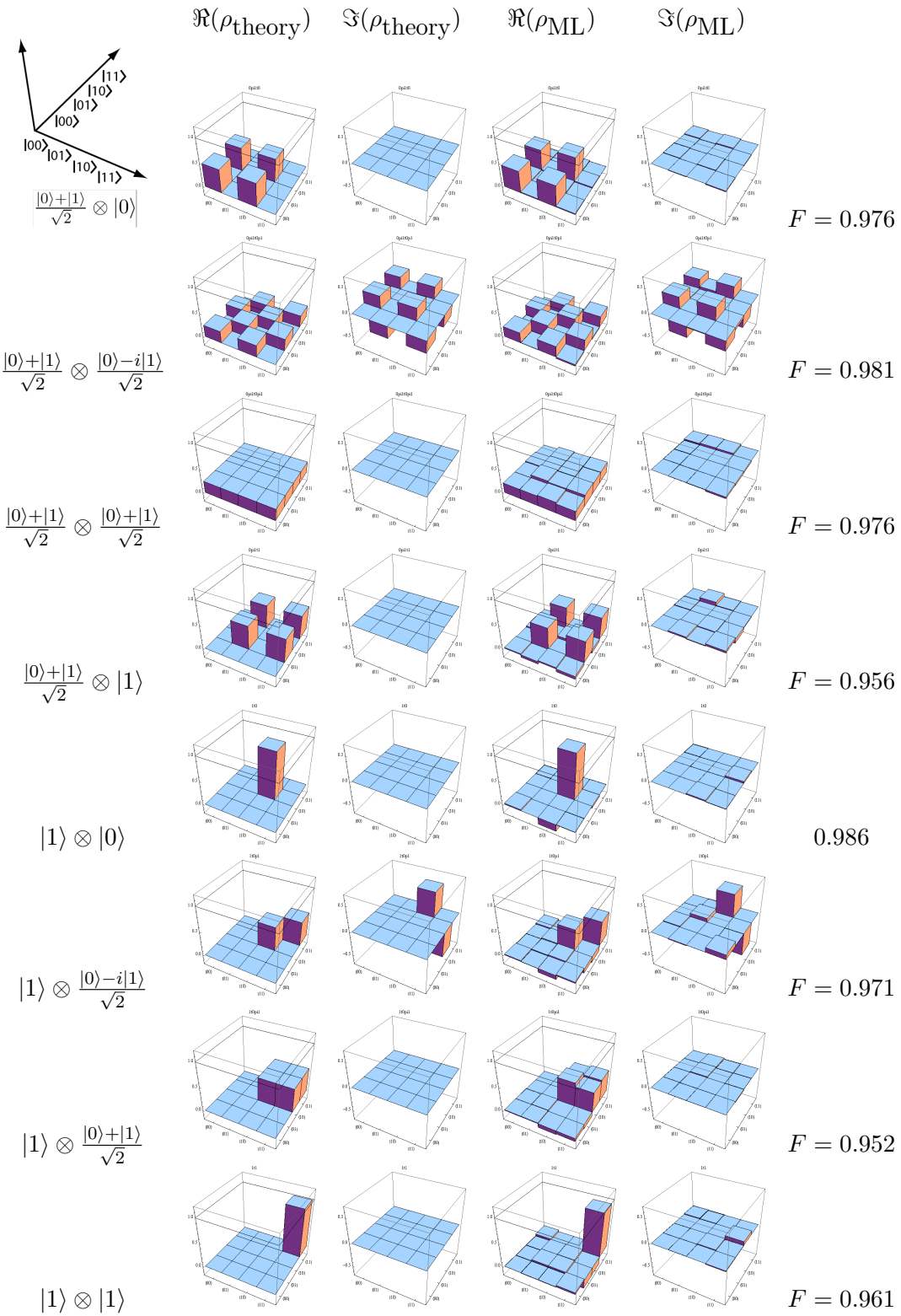

Figure 4.11: Continue from Fig. 4.10.

Conclusion

In this Diplomarbeit we have realized a tomography procedure for one and two qubits. The tomography on one qubit has been applied on different superposition states as discussed in Section 3.4.2. The tomography was performed with well calibrated pulses as well as with an auto calibration method, which allows to compensate imperfect tomography pulses. Further more, we performed tomography on Rabi (Section 3.4.3) and Ransey (Section 3.4.4) experiments. These experiments agree with the theoretical expected states as we have confirmed by extracting the L_1 norm, which has been found for the two processes to be of the order of 0.08 and 0.07. Moreover we have realized a Hadamard gate in Section 3.4.5 and applied process tomography on it. The result confirms the theoretical expected operation. We have written analysis files in Mathematica6.0 which can be used for further experiments.

In addition we have realized a two qubit tomography procedure. Since Circuit QED provides us with only one measurement operator it is impossible to readout the qubits individually. This is a different to all the other systems like ions, NMR and quantum dots where each qubits can be readout individually. Therefore we have realized a tomography method to characterize the system by using just one measurement operator. We performed this two qubit tomography on different product states as shown in (Section 4.4). With this we have been able to reconstruct states which are close to the theoretical expected density matrices. In addition to find physical density matrices (i.e. positive definite) we employed a most likelihood procedure. The fidelity between the found density matrices and the theoretical expected matrices are high and between 0.93 to 0.99. Very careful calibration of the tomography pulses and their frequency can probably yield to an even higher fidelity. The analysis file and pattern writing file for the two qubit tomography can easily be applied for tomography on systems with more then two qubits.

We have seen that one and two qubit tomography works well. However it would be good to adapt the method for the demand of further experiments. For example if we realize a two qubit state by pulses, which are not created in the same way as the tomography pulse (see 4.3), we will have to face the problem of a relative phase shift. Probably it will be possible to adjust the phase by sweeping one of the microwave generators.

In a next step the automation of the tomography process would be desirable. However, this would requires some major changes on the measurement software. Furthermore it would be good to implement the cavity Bloch equations [39] into the two qubit tomography. This would give us the opportunity to derive the measurement operator from theory rather then from an experiment (see Section 4.3). Nevertheless we have not yet analised the cavity

Bloch equations for a two qubit system. Moreover there has been ongoing effort to realize a two qubit Bell state. Two qubit tomography enables us to verify whether we have achieved to create an entangled state or not.

Chapter 5

Appendix

5.1 Topological set of tomography pulses for two qubit

If we apply id, $\left(\frac{\pi}{2}\right)_x$, $\left(\frac{\pi}{2}\right)_y$ and π pulses on each of the qubit individually, we can find the following 16 unitary operations. These operations are a complete set of tomography pulses $U_{\Omega_i,\Omega_j} = \exp\left[-i\frac{\Omega_i\sigma_i\otimes id+\Omega_j id\otimes\sigma_j}{2}\right]$ to reconstruct an arbitrary state.

$$U_{id,id} = \begin{pmatrix} i & 0 & 0 & 0 \\ 0 & i & 0 & 0 \\ 0 & 0 & i & 0 \\ 0 & 0 & 0 & i \end{pmatrix}, U_{id,\left(\frac{\pi}{2}\right)_x} = \begin{pmatrix} \frac{1}{2}+\frac{i}{2} & -\frac{1}{2}+\frac{i}{2} & 0 & 0 \\ -\frac{1}{2}+\frac{i}{2} & \frac{1}{2}+\frac{i}{2} & 0 & 0 \\ 0 & 0 & \frac{1}{2}+\frac{i}{2} & -\frac{1}{2}+\frac{i}{2} \\ 0 & 0 & -\frac{1}{2}+\frac{i}{2} & \frac{1}{2}+\frac{i}{2} \end{pmatrix},$$

$$U_{id,\left(\frac{\pi}{2}\right)_y} = \begin{pmatrix} \frac{1}{2}+\frac{i}{2} & \frac{1}{2}+\frac{i}{2} & 0 & 0 \\ -\frac{1}{2}-\frac{i}{2} & \frac{1}{2}+\frac{i}{2} & 0 & 0 \\ 0 & 0 & \frac{1}{2}+\frac{i}{2} & \frac{1}{2}+\frac{i}{2} \\ 0 & 0 & -\frac{1}{2}-\frac{i}{2} & \frac{1}{2}+\frac{i}{2} \end{pmatrix}, U_{id,\pi_x} = \begin{pmatrix} 0 & \frac{1+i}{\sqrt{2}} & 0 & 0 \\ -\frac{1+i}{\sqrt{2}} & 0 & 0 & 0 \\ 0 & 0 & 0 & \frac{1+i}{\sqrt{2}} \\ 0 & 0 & -\frac{1+i}{\sqrt{2}} & 0 \end{pmatrix},$$

$$U_{\left(\frac{\pi}{2}\right)_x,id} = \begin{pmatrix} \frac{1}{2}+\frac{i}{2} & 0 & -\frac{1}{2}+\frac{i}{2} & 0 \\ 0 & \frac{1}{2}+\frac{i}{2} & 0 & -\frac{1}{2}+\frac{i}{2} \\ -\frac{1}{2}+\frac{i}{2} & 0 & \frac{1}{2}+\frac{i}{2} & 0 \\ 0 & -\frac{1}{2}+\frac{i}{2} & 0 & \frac{1}{2}+\frac{i}{2} \end{pmatrix}, U_{\left(\frac{\pi}{2}\right)_x,\left(\frac{\pi}{2}\right)_x} = \begin{pmatrix} \frac{1}{2} & \frac{i}{2} & \frac{i}{2} & -\frac{1}{2} \\ \frac{i}{2} & \frac{1}{2} & -\frac{1}{2} & \frac{i}{2} \\ \frac{i}{2} & -\frac{1}{2} & \frac{1}{2} & \frac{i}{2} \\ -\frac{1}{2} & \frac{i}{2} & \frac{i}{2} & \frac{1}{2} \end{pmatrix},$$

$$U_{\left(\frac{\pi}{2}\right)_x,\left(\frac{\pi}{2}\right)_y} = \begin{pmatrix} \frac{1}{2} & \frac{1}{2} & \frac{i}{2} & \frac{i}{2} \\ -\frac{1}{2} & \frac{1}{2} & -\frac{i}{2} & \frac{i}{2} \\ \frac{i}{2} & \frac{i}{2} & \frac{1}{2} & \frac{1}{2} \\ -\frac{i}{2} & \frac{i}{2} & -\frac{1}{2} & \frac{1}{2} \end{pmatrix}, U_{\left(\frac{\pi}{2}\right)_x,\pi_x} = \begin{pmatrix} 0 & \frac{1}{\sqrt{2}} & 0 & \frac{i}{\sqrt{2}} \\ -\frac{1}{\sqrt{2}} & 0 & -\frac{i}{\sqrt{2}} & 0 \\ 0 & \frac{i}{\sqrt{2}} & 0 & \frac{1}{\sqrt{2}} \\ -\frac{i}{\sqrt{2}} & 0 & -\frac{1}{\sqrt{2}} & 0 \end{pmatrix},$$

$$U_{\left(\frac{\pi}{2}\right)_y,id} = \begin{pmatrix} \frac{1}{2}+\frac{i}{2} & 0 & \frac{1}{2}+\frac{i}{2} & 0 \\ 0 & \frac{1}{2}+\frac{i}{2} & 0 & \frac{1}{2}+\frac{i}{2} \\ -\frac{1}{2}-\frac{i}{2} & 0 & \frac{1}{2}+\frac{i}{2} & 0 \\ 0 & -\frac{1}{2}-\frac{i}{2} & 0 & \frac{1}{2}+\frac{i}{2} \end{pmatrix}, U_{\left(\frac{\pi}{2}\right)_y,\left(\frac{\pi}{2}\right)_x} = \begin{pmatrix} \frac{1}{2} & \frac{i}{2} & \frac{1}{2} & \frac{i}{2} \\ \frac{i}{2} & \frac{1}{2} & \frac{i}{2} & \frac{1}{2} \\ -\frac{1}{2} & -\frac{i}{2} & \frac{1}{2} & \frac{i}{2} \\ -\frac{i}{2} & -\frac{1}{2} & \frac{i}{2} & \frac{1}{2} \end{pmatrix},$$

$$U_{\left(\frac{\pi}{2}\right)_y,\left(\frac{\pi}{2}\right)_y} = \begin{pmatrix} \frac{1}{2} & \frac{1}{2} & \frac{1}{2} & \frac{1}{2} \\ -\frac{1}{2} & \frac{1}{2} & -\frac{1}{2} & \frac{1}{2} \\ -\frac{1}{2} & -\frac{1}{2} & \frac{1}{2} & \frac{1}{2} \\ \frac{1}{2} & -\frac{1}{2} & -\frac{1}{2} & \frac{1}{2} \end{pmatrix}, U_{\left(\frac{\pi}{2}\right)_y,\pi_x} = \begin{pmatrix} 0 & \frac{1}{\sqrt{2}} & 0 & \frac{1}{\sqrt{2}} \\ -\frac{1}{\sqrt{2}} & 0 & -\frac{1}{\sqrt{2}} & 0 \\ 0 & -\frac{1}{\sqrt{2}} & 0 & \frac{1}{\sqrt{2}} \\ \frac{1}{\sqrt{2}} & 0 & -\frac{1}{\sqrt{2}} & 0 \end{pmatrix},$$

$$U_{\pi_x,id} = \begin{pmatrix} 0 & 0 & \frac{1+i}{\sqrt{2}} & 0 \\ 0 & 0 & 0 & \frac{1+i}{\sqrt{2}} \\ -\frac{1+i}{\sqrt{2}} & 0 & 0 & 0 \\ 0 & -\frac{1+i}{\sqrt{2}} & 0 & 0 \end{pmatrix}, U_{\pi_x,\left(\frac{\pi}{2}\right)_x} = \begin{pmatrix} 0 & 0 & \frac{1}{\sqrt{2}} & \frac{i}{\sqrt{2}} \\ 0 & 0 & \frac{i}{\sqrt{2}} & \frac{1}{\sqrt{2}} \\ -\frac{1}{\sqrt{2}} & -\frac{i}{\sqrt{2}} & 0 & 0 \\ -\frac{i}{\sqrt{2}} & -\frac{1}{\sqrt{2}} & 0 & 0 \end{pmatrix},$$

$$U_{\pi_x,\left(\frac{\pi}{2}\right)_y} = \begin{pmatrix} 0 & 0 & \frac{1}{\sqrt{2}} & \frac{1}{\sqrt{2}} \\ 0 & 0 & -\frac{1}{\sqrt{2}} & \frac{1}{\sqrt{2}} \\ -\frac{1}{\sqrt{2}} & -\frac{1}{\sqrt{2}} & 0 & 0 \\ \frac{1}{\sqrt{2}} & -\frac{1}{\sqrt{2}} & 0 & 0 \end{pmatrix}, U_{\pi_x,\pi_x} = \begin{pmatrix} 0 & 0 & 0 & 1 \\ 0 & 0 & -1 & 0 \\ 0 & -1 & 0 & 0 \\ 1 & 0 & 0 & 0 \end{pmatrix}.$$

5.2 System of equations for two qubit tomography

Here we give the exact form of the system of equations, which results form the 16 tomography pulses described in the appendix 5.1. For simplicity we parametrize the density matrix by

$$\rho = \frac{1}{4} \sum_{i,j=0,x,y,z} r_{i,j} \sigma_i \otimes \sigma_j.$$

Using the isomorphism $p_k \mapsto p_k \vec{e}_k$ and $r_k \mapsto r_k \vec{e}_k$ we can obtain the formula

$$r = \left(\frac{p_{|01\rangle\langle 10|}\Lambda_1 + p_{|10\rangle\langle 01|}\Lambda_2 + p_{|11\rangle\langle 11|}\Lambda_3}{4} \right)^{-1} p,$$

with $p_{|ij\rangle\langle ji|}$ the weighted averaged phase shift for the state $|01\rangle\langle 10|$ (see Section 4.3) the matrices Λ_i defined as

$\overline{M}_1 =$

```
(100 -10  0  00  000  0  1  0  0 -1)
(10-10  0  0  00  000  0  1  0 -10 )
(110  0  0  0  00  000  0  1  1  0  0)
(100  1  0  0  00  000  0  1  0  0  1)
(100 -10  0  00  100 -10  0  0  0 )
(10-10  0  0  00  10-10  0  0  0  0)
(110  0  0  0  00  110  0  0  0  0  0)
(100  1  0  0  00  100  1  0  0  0  0)
(100 -1-10  01  000  0  0  0  0  0)
(10-10 -10  10  000  0  0  0  0  0)
(110  0 -1-100  000  0  0  0  0  0)
(100  1 -10  0-1000  0  0  0  0  0)
(100 -10  0  00  000  0 -10  0  1)
(10-10  0  0  00  000  0 -10  1  0)
(110  0  0  0  00  000  0 -1-10  0)
(100  1  0  0  00  000  0 -10  0 -1)
```

$\overline{M}_2 =$

```
(10  01  00  00  0  00  0 -10  0 -1)
(10  10  00  00  0  00  0 -10 -10 )
(1-100  00  00  0  00  0 -11  0  0)
(10  0-100  00  0  00  0 -10  0  1)
(10  01  00  00 -100 -10  0  0  0)
(10  10  00  00 -10-10  0  0  0  0)
(1-100  00  00 -110  0  0  0  0  0)
(10  0-100  00 -100  1  0  0  0  0)
(10  01  10  01  0  00  0  0  0  0)
(10  10  10  10  0  00  0  0  0  0)
(1-100  1-100  0  00  0  0  0  0  0)
(10  0-110  0-10  00  0  0  0  0  0)
(10  01  00  00  0  00  0  1  0  0  1)
(10  10  00  00  0  00  0  1  0  1  0)
(1-100  00  00  0  00  0  1  -10  0 )
(10  0-100  00  0  00  0  1  0  0 -1)
```

$\overline{M}_3 =$

```
(100 -1000  0  0  0  00 -10  0  1 )
(10-10  000  0  0  0  00 -10  1  0 )
(110  0  000  0  0  0  00 -1-10  0 )
(100  1  000  0  0  0  00 -10  0 -1)
(100 -1000  0 -10  01  0  0  0  0 )
(10-10  000  0 -10  10  0  0  0  0 )
(110  0  000  0 -1-100  0  0  0  0 )
(100  1  000  0 -10  0-10  0  0  0 )
(100 -1100 -10  0  00  0  0  0  0 )
(10-10  10-10  0  0  00  0  0  0  0 )
(110  0  110  0  0  0  00  0  0  0  0 )
(100  1  100  1  0  0  00  0  0  0  0 )
(100 -1000  0  0  0  00  1  0  0 -1)
(10-10  000  0  0  0  00  1  0 -10 )
(110  0  000  0  0  0  00  1  1  0  0 )
(100  1  000  0  0  0  00  1  0  0  1 )
```

The condition for inverting the matrix $A = \left(\frac{M_1\Lambda_1 + M_2\Lambda_2 + M_3\Lambda_3}{4}\right)$ is given in the theory chapter Section 4.1.2 and can easily be proven by calculating $\det(A) \neq 0$.

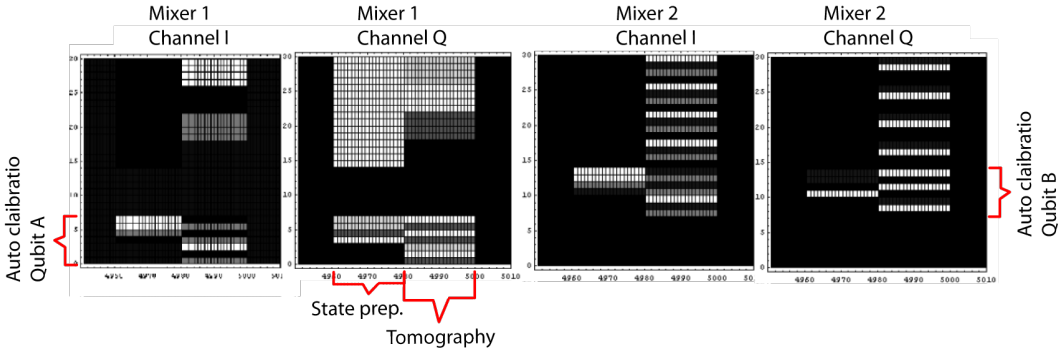

Figure 5.1: The picture shows a characteristic pattern file. The four plots show the pulse sequence for the I and Q channel of mixer 1 and for the I and Q channel of mixer 2.

5.3 Sequence file

The pulse sequences for the measurement are defined by pattern files. A pattern file consists of a pulse sequence which controlls the voltage applied on the channel for the two I/Q mixers, a trigger for the acquisition card and a trigger for the measurement microwave generator generator, which is used for pulsed measurements. The time resolution for the drive pulses are 1 ns and the amplitude has a 10 bit resolution. The pattern files are run by an arbitrary waveform generator (AWG). For a measurement run several pattern files combined in one sequence file are load into the AWG simultaneously. The experiment is organized in the following way: each of the pattern files is run sequential once, after running each of the pattern files once the procedure is repeated several times and averaged.

In all the experiments the sequence file consists of an auto calibration part and a part which contains the experiment. A schematic plot of a patter file is given in Fig. 5.1

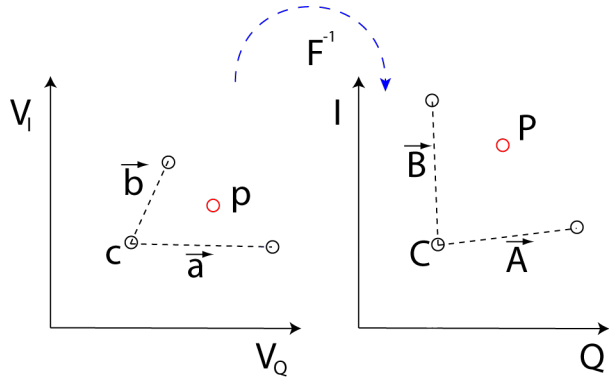

Figure 5.2: The picture shows schematically how we calculate the voltage (P_1, P_2) which we have to apply on the I/Q mixer to create the a microwave at the output with amplitudes (p_1, p_2). The points a, b, c and A, B, C comes from measurements with a VNA. The points a, b, c are the three closest point to the desired point p.

5.4 Mixer calibration

The I/Q mixer which we used for controlling the amplitude and the phase of the microwave pulses is not ideal. Even though that we have seen it is possible to calibrate the tomography pulse without calibrating the mixer it would be nice if the used I/Q mixer is calibrated.

To calibrate the I/Q mixer we measured with a Vector Network Analyzer (VNA) the amplitude and the phase of the out coming microwave field (V_I, V_Q) as a function of the applied (I, Q) voltage as shown in Fig. 5.4. This gives us the discrete function F which maps (I, Q) on (V_I, V_Q). The task is now to determine the voltage $\vec{P} = (P_1, P_2)$, which we have to apply in the I/Q channel, so that we obtain on the mixer's output the desired microwave field $\vec{p} = (p_1, p_2)$. For this we find the three points $\vec{a}, \vec{b}, \vec{c} \in (V_I, V_Q)$ which are closest to the point (P_1, P_2), this allows us to determine the parameter (α, β) so that the condition $\alpha(\vec{a} - \vec{c}) + \beta(\vec{b} - \vec{c}) + \vec{c} = \vec{p}$ is fulfilled.

$$\begin{pmatrix} \alpha \\ \beta \end{pmatrix} = \begin{pmatrix} a_1 - c_1 & b_1 - c_1 \\ a_2 - c_2 & b_2 - c_2 \end{pmatrix}^{-1} (\vec{p} - \vec{c}) \,.$$

On the other hand we can write for the input voltage $\alpha'(\vec{A} - \vec{C}) + \beta'(\vec{B} - \vec{C}) + \vec{C} = \vec{P}$, where we have used from the calibration measurement $\vec{A} = F^{-1}(\vec{a}), \ldots$. In first order we can assume $\alpha = \alpha'$ and $\beta = \beta'$ and we find for the Voltage on the I/Q channel

$$\vec{P} = \begin{pmatrix} A_1 - C_1 & B_1 - C_1 \\ A_2 - C_2 & B_2 - C_2 \end{pmatrix} \begin{pmatrix} a_1 - c_1 & b_1 - c_1 \\ a_2 - c_2 & b_2 - c_2 \end{pmatrix}^{-1} (\vec{p} - \vec{c}) + \vec{C}.$$

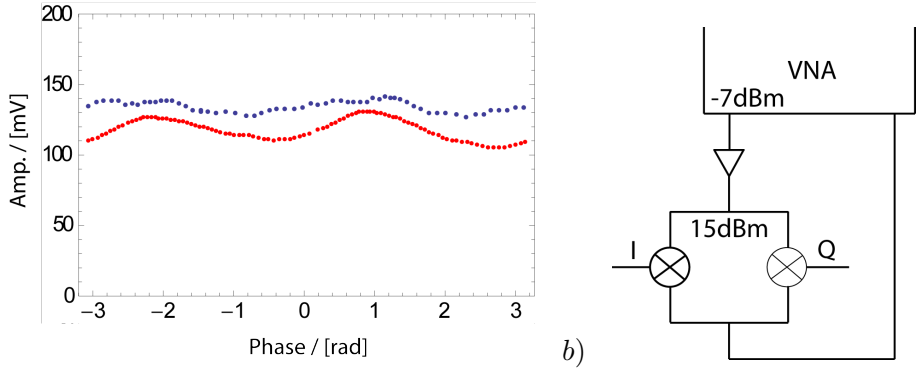

a) *b)*

Figure 5.3: The right plot shows the amplitude of the output microwave filed for different phases for the calibrated data (blue) and the uncalibrated data (red). The left picture shows the measurement setup which was uses for the calibration. Since the Vector Network Analyzer (VNA) can only create an output power of −7dBm but we are interested at a power of 15dBm we have to use an amplifier.

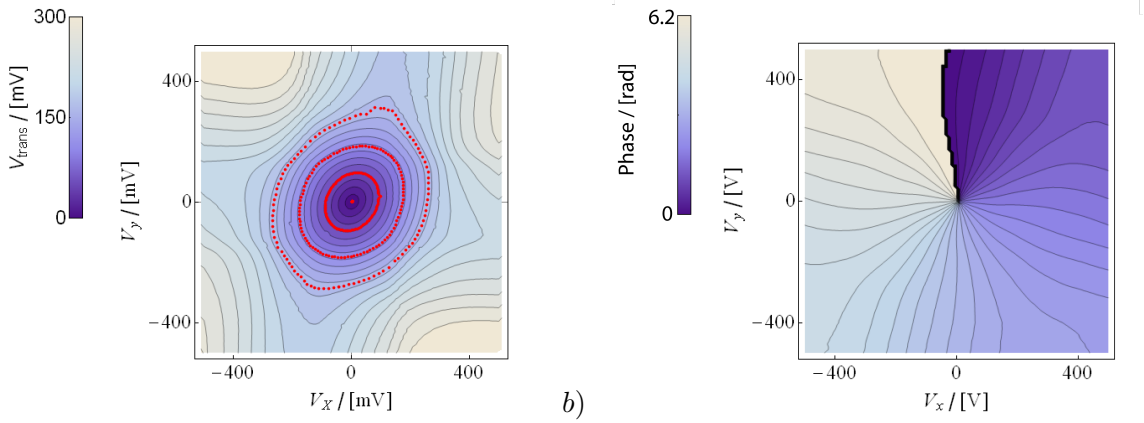

a) *b)*

Figure 5.4: The Plot shows for the measurement form the Vector Network Analyzer the amplitude (left) as a function of (I, Q) and the phase (right) as a function of (I, Q) of the output microwave. The input field is at a power of 15 dBm.

5.5 Operator sum representation

The time evolution is given by the map L, which is linear and conserves the property of the density matrix (positive hermiticity and trace one). If we assume that the initial qubit state is not entangled with the environment, we can write the starting state by $|\psi\rangle = N \sum_j \left|\varphi_j^{qubit}\right\rangle \otimes \left|\varphi_j^E\right\rangle$, where the last $N_E - N_{qubit}$ states build a basis orthogonal on H_{qubit}. Applying the operator L on this state yields

$$L \otimes 1_E \left(|\psi\rangle \langle\psi|\right) = \sum_i q_i \left|\Phi_i\right\rangle \left\langle\Phi_i\right|.$$

If we measure the environment Tr_E, we will obtain

$$\left\langle\varphi_j^E\right| L \otimes 1_E \left(|\psi\rangle \langle\psi|\right) \left|\varphi_j^E\right\rangle = \sum_i q_i \left\langle\varphi_j^E\right| \left|\Phi_i\right\rangle \left\langle\Phi_i\right| \left|\varphi_j^E\right\rangle.$$

The element $\left\langle\varphi_j^E\right| |\Phi_i\rangle$ is in H_{qubit}, since $|\Phi_i\rangle \in H_{qubit} \otimes H_E$ and $|\psi_i\rangle \in H_E$. Therefore we can do a basis transformation and find

$$L\left(\left|\varphi^{qubit}\right\rangle \left\langle\varphi^{qubit}\right|\right) = \sum_{j \leq N_{qubit}^2} M_j \left|\varphi^{qubit}\right\rangle \left\langle\varphi^{qubit}\right| M_j^\dagger,$$

or for an arbitrary density matrix

$$L = \sum_{j \leq N_{qubit}^2} M_j \rho M_j^\dagger.$$

It is remarkable that any process, which describes interaction between the qubit and the environment, can be written by using not more then N_{qubit}^2 operators regardless of the dimension of the environment (provided that $\dim H_E > \dim H_{qubit}$).

If we take interaction with the environment into account, the evolution of the qubit is not anymore described by the Von Neumann equation but by the master equation, which is a direct consequence of Markovian processes [41] and the operator sum representation. The master equation is then given by

$$\frac{d\rho}{dt} = -\frac{i}{\hbar}[H, \rho] + \sum_{n \neq 0} \left(L_n \rho L_n^\dagger - \frac{1}{2} L_n^\dagger L_n \rho - \frac{1}{2} \rho L_n^\dagger L_n \right),$$

where the Markov approximation $M_n(t) = \sqrt{t} L_n$ has been used.

5.6 Data sheet for two qubit sample

The used two qubit sample has the following specifications for qubit A:

g	133 MHz
E_J	35.11 GHz
E_C	231.7 GHz

Qubit B has the specificatio:

g	134 MHz
E_J	37.63 GHz
E_C	231.5 GHz

The resonator has the bare resonance frequency at $\nu_0 = 6.40845$ GHz and a quality factor $Q = 4092.39$ and $\kappa = 1.56595$ MHz.

Bibliography

[1] A. Blais, R. S. Huang, A. Wallraff, S. M. Girvin, and R. J. Schoelkopf. Cavity quantum electrodynamics for superconducting electrical circuits: An architecture for quantum computation. *Physical Review A*, 69(6):062320, June 2004.

[2] L. Frunzio, A. Wallraff, D. Schuster, J. Majer, and R. Schoelkopf. Fabrication and characterization of superconducting circuit QED devices for quantum computation. *IEEE Transactions On Applied Superconductivity*, 15(2):860–863, June 2005.

[3] J. Majer, J. M. Chow, J. M. Gambetta, Jens Koch, B. R. Johnson, J. A. Schreier, L. Frunzio, D. I. Schuster, A. A. Houck, A. Wallraff, A. Blais, M. H. Devoret, S. M. Girvin, and R. J. Schoelkopf. Coupling superconducting qubits via a cavity bus. *Nature*, 449(7161):443–447, September 2007.

[4] J. H. Plantenberg, P. C. de Groot, C. J. P. M. Harmans, and J. E. Mooij. Demonstration of controlled-not quantum gates on a pair of superconducting quantum bits. *Nature*, 447(7146):836–839, June 2007.

[5] Munro White James, Kwiat. Measurement of qubits. *Physical Review A*, 64:052312, 2001.

[6] I. L. Chuang and M. A. Nielsen. Prescription for experimental determination of the dynamics for quantum black box. *Journal of modern optics*, 44:2455–2467, 1996.

[7] G.L. Long, H.Y. Yan, and Yang Sun. Analysis of density matrix reconstruction in nmr quantum computing. *Journal of optics B*, pages 376–381, 2001.

[8] Lancaster GPT Roos, CF and, M Riebe, H Haffner, W Hansel, S Gulde, C Becher, J Eschner, F Schmidt-Kaler, and R Blatt. Bell states of atoms with ultralong lifetimes and their tomographic state analysis. *PHYSICAL REVIEW LETTERS*, 92, 2004.

[9] Jens Koch, Terri M. Yu, Jay Gambetta, A. A. Houck, D. I. Schuster, J. Majer, Alexandre Blais, M. H. Devoret, S. M. Girvin, and R. J. Schoelkopf. Charge-insensitive qubit design derived from the Cooper pair box. *Physical Review A*, 76(4):042319, 2007.

[10] Richard Feynman. Simulating physics with computers. *International Journal of Theoretical Physics*, 21(6):467–488, June 1982.

[11] David Deutsch and Richard Jozsa. Rapid solution of problems by quantum computation. *Proceedings: Mathematical and Physical Sciences*, 439(1907):553–558, December 1992.

[12] Peter W. Shor. Polynomial-time algorithms for prime factorization and discrete logarithms on a quantum computer. *SIAM Journal on Scientific and Statistical Computing*, 26:1484, 1997.

[13] Lov K. Grover. A fast quantum mechanical algorithm for database search. In *Proceedings of the twenty-eighth annual ACM symposium on Theory of computing*, pages 212–219, Philadelphia, Pennsylvania, United States, 1996. ACM.

[14] D. P. DiVincenzo. The physical implementation of quantum computation. *arxiv*, page 3, 2000.

[15] RJ Hughes. Quantum computing with trapped ions. *METHODS FOR ULTRASENSITIVE DETECTION*, 3270:120–130, 1998.

[16] Taylor JM Laird EA Yacoby A Lukin MD Marcus CM Hanson MP Gossard AC Petta JR, Johnson AC. Coherent manipulation of coupled electron spins in semiconductor quantum dots. *Science*, 309:2180–2184, 2005.

[17] Wilhelm FK Clarke J. Superconducting quantum bits. *Nature*, 453:1031–1042, 2008.

[18] M. K. Lieven, Vandersypen, M. Steffen, M. G. Breyta, C. S. Yannoni, Sherwood M. H., and Chuang I. L. Experimental realization of shor's quantum factoring algorithm using nuclear magnetic resonance. *Nature*, 414:883–887, 2001.

[19] H.; Riebe M.; Gulde S.; Lancaster C.P.T.; Deuschle T.; Becher C.; Roos C.; Eschner J.; Blatt R. SchmidtKaler, F.; Haffner. Realisation of the cirac-zoller controlled-not quantum gate. *European Quantum Electronics Conference*, page 384, 2003.

[20] A. Wallraff, D. Schuster, L. Frunzio, and R. Schoelkopf. A measurement setup for circuit quantum electrodynamics. *Applied Physics Letters*, ?:?, 2004. (we should write this one).

[21] Y. Nakamura, Y. A. Pashkin, and J. S. Tsai. Coherent control of macroscopic quantum states in a single-cooper-pair box. *Nature*, 398(6730):786–788, April 1999.

[22] V. Bouchiat, D. Vion, P. Joyez, D. Esteve, and M. H. Devoret. Quantum coherence with a single Cooper pair. *Physica Scripta*, T76:165–170, 1998.

[23] B. D. Josephson. Possible new effects in superconductive tunnelling. *Physics Letters*, 1(7):251–253, July 1962.

[24] D. I. Schuster. *Circuit Quantum Electrodynamics*. PhD thesis, Yale University, 2007.

[25] A. Shnirman, G. Schön, and Z. Hermon. Quantum manipulations of small josephson junctions. *Physical Review Letters*, 79(12):2371–2374, September 1997.

[26] D. Vion, A. Aassime, A. Cottet, P. Joyez, H. Pothier, C. Urbina, D. Esteve, and M. H. Devoret. Manipulating the quantum state of an electrical circuit. *Science*, 296(5569):886–889, May 2002.

[27] A. Wallraff, D. I. Schuster, A. Blais, L. Frunzio, R.-S Huang, J. Majer, S. Kumar, S. M. Girvin, and R. J. Schoelkopf. Circuit quantum electrodynamics: Coherent coupling of a single photon to a Cooper pair box. *Nature*, 431:162, 2004.

[28] A. Blais, J. Gambetta, A. Wallraff, D. I. Schuster, S. M. Girvin, M. H. Devoret, and R. J. Schoelkopf. Quantum-information processing with circuit quantum electrodynamics. *Physical Review A*, 75(3):032329, March 2007.

[29] Jay Gambetta, Alexandre Blais, M. Boissonneault, A. A. Houck, D. I. Schuster, and S. M. Girvin. Quantum trajectory approach to circuit qed: Quantum jumps and the zeno effect, 2007.

[30] Johnson Chow Koch Gambetta Schuster Frunzio Devoret Girvin Schoelkopf Houck, Schreier. Controlling the spontaneous emission of a superconducting transmon qubit. *arXiv*, 2008.

[31] P. J. Leek, J. M. Fink, A. Blais, R. Bianchetti, M. Göppl, J. M. Gambetta, D. I. Schuster, L. Frunzio, R. J. Schoelkopf, and A. Wallraff. Observation of Berry's Phase in a Solid-State Qubit. *Science*, 318(5858):1889–1892, 2007.

[32] Chuang Nielsen. *Quantum Computation and Quantum Information.* Cambridge Univertity Press, 2000.

[33] Nielson Gilchrist, Lamgford. Distance measures to real and ideal quantum processes. *Physical review A*, 71:062310, 2005.

[34] J. Gambetta, A. Blais, D. I. Schuster, A. Wallraff, L. Frunzio, J. Majer, M. H. Devoret, S. M. Girvin, and R. J. Schoelkopf. Qubit-photon interactions in a cavity: Measurement-induced dephasing and number splitting. *Physical Review A*, 74(4):042318, October 2006.

[35] Jaroslav Rehacek, Englert Berthold-Georg, and Kaszlikowski Dagomir. Minimal qubit tomography. *Phys. Rev. Lett. A*, 70:052321, 2004.

[36] A. Abragam. *Principles of Nuclear Magnetism.* Oxford University Press, 1961.

[37] Fiurasek and Hradil. Maximum likelihood estimation of quantum processes. *Physical review A*, 63, 2001.

[38] Boissonneault, Gambetta, and Blais. Nonlinear dispersive regime of cavity qed: The dressed dephasing model. *Physical review A*, 77, 2008.

[39] Boissonneault. *Effets non-lineaires et qualite de la mesure en electrodynamique quantique en circuit.* PhD thesis, Universite de Sherbrooke, 2007.

[40] Riebe. *Preparation of Entangled States and Quantum Teleportation with Atomic Qubits.* PhD thesis, Leopold Franzens Universitaet Innsbruck, 2005.

[41] Haroche and Raimond. *Exploring the quantum; Atoms, cavities, and photons.* Oxford Graduate Texts, 2006.